الجمهورية الجزائرية الديمقراطية الشعبية
PEOPLE'S DEMOCRATIC REPUBLIC OF ALGERIA
وزارة التعليم العالي والبحث العلمي
Ministry Of Higher Education and Scientific Research
جامعة الإخوة منتوري قسنطينة 1
Frères Mentouri University-Constantine 1
كلية علوم التكنولوجيا
Sciences of Technology Faculty
قسم الإلكترونيك
Electronic department

Order N°: 112 /D3C / 2022
Series: 12/Elec / 2021

PhD Dissertation

Presented to obtain the diploma

Doctorate 3rd Cycle LMD

Option: Electronics

Speciality: Micro-Nano electronics and photonics

By

BOUGHEDDA Abderrezak

THEME

Silicon radiation detectors in 3D technology at high speed and low energy consumption

22 December 2021

Committee members:

Chairman :	**S. SAHLI**	**Prof.**	**University of Constantine 1**
Advisor :	**M.LAKHDARA**	**Prof.**	**University of Constantine 1**
Co-Advisor:	**GF. DALLA BETTA**	**Prof.**	**University of Trento, Italy**
Examiners :	**A. TELIA**	**Prof.**	**University of Constantine 1**
	R. MAHAMDI	**Prof.**	**University of Batna 2**
	A.MERZOUGUI	**M.C.A.**	**University of Oum El Bouaghi**
Invited :	**S. LATRECHE**	**Prof.**	**University of Constantine 1**

Acknowledgments

First of all, I am grateful to my supervisor Professor ***Maya LAKHDARA****, whose knowledge and guidance enabled me to develop an understanding of the subject. Your informative remarks encouraged me to improve my thoughts and raise the quality of my work.*

I would like also to express my thankfulness to Professor ***Saida LATRECHE****, who provided help, guidance and support, an exemplary person of ethics and responsibility. And also every member of the Laboratory of Hyperfrequencies and Semiconductors (LHS).*

My special thanks go to my co-supervisor Professor ***Gian-Franco Dalla Betta*** *for facilitating such a positive learning environment at the University of Trento and the fruitful discussions that helped me increasing my knowledge on my topics, this work could not have been completed without his guidance.*

. *I would take advantage of the opportunity to thank Professor* ***Salah SAHLI*** *for being kind enough to judge our work and honor us by being the president of the Ph.D. Commission and for the whole commission, Professor* **Azzedine TELIA,** *professor.* **Ramdane MAHAMDI and Doctor *Amina* MERZOUGUI.**

My acknowledgements would not be complete without thanking ***my friend and my colleagues*** *for the support they gave me during these years of hard work.*

Finally, I welcome this opportunity to thank ***my parents****,* ***brother and sister*** *. Thank you* ***father*** *and* ***mother!*** *I do not know how to express my love for you. I am just speechless by remembering your contribution to my life. May Allah grant my father the highest rank in Jannah and protect my mother. This thesis is dedicated to my family.*

Table of contents

Table of Figures

List of Tables

General introduction

General introduction

A detector, in the broadest sense, is a device, module, machine, or subsystem that detects events or changes in its surroundings and transmits the data to other electronics, most commonly a computer processor. They are always used in conjunction with other electronics.

Nuclear detectors are special kind of instruments that can detect nuclear particles α particle, β particle or gamma radiation.They can also determine their energy momentum, direction and many other parameters. There are several different kinds of detectors, from which a special class of nuclear detectors is distinguished. This class is known as semiconductors detectors. These devices are used in a various research centers worldwide such as XFEL and the European Nuclear Research Center (CERN) with its ATLAS, CMS detectors, etc.

The first generation of X-ray free electron lasers (FEL) has been proven to be very successful as means to investigate the microscopic structure of both organic and inorganic materials that are used in different fields (i.e. Biology, chemistry, material science, atomic and molecular sciences). Those applications require the development of new X ray imaging edgeless planar detectors to satisfy very challenging requirements, such as space and amplitude resolution, input dynamic range, frame rate and frame storage capability. Silicon strip and silicon drift detectors were the first to become available, followed by silicon pixel detectors a few years later.

Several research groups have been working on improving these planar detectors by reducing their size and maximize the breakdown voltage, calling the 3D technology, among which we can cite the PixFEL project [1]. These detectors are built on hybrid multilayer tiles made of active-edge high resistivity pixel sensors bump-bonded to two-tiered 65-nm CMOS front-end ICs. These planar detectors are not preferred at high fluences such in the case of innermost layer of LHC (the Large Hadron Collider). Recently there has been extensive research on 3D radiation sensors due to the very small distance between the vertical electrodes. This plays a crucial role in lowering the power dissipation and enhancing the radiation hardness. All these features make them a tempting choice for the innermost layers of high luminosity tracking detectors LHC (HL-LHC), where it is expected to scale up to 200 events /bunch crossing owing to the high luminosity (5×10^{34} cm^{-2} s^{-1}).

The CERN RD53 Collaboration has been working on the construction of a new read-out chip in 65 nm CMOS technology, whereas several R&D projects have been initiated, aimed at developing various sensor technologies. The FBK INFN Italy collaboration (the National **Institute of Nuclear Physics** and **the Research Institute Fondazione Bruno**

Kessler of Trento) is one of the three designing groups working in tandem in order to develop the appropriate design. A new generation of pixel sensors has been developed for the Phase 2 Upgrades at the High Luminosity LHC (HL LHC). They are produced using a single sided Technology on Si-Si Direct Wafer Bonded "substrates" ,featuring pixel sizes of 50×50 μm^2 with 1 readout column, and 25×100 μm^2 with 1 or 2 readout columns (1E and 2E) . Owing to the small inter electrode distance, ranging from ~28 µm to ~51 µm in the considered layouts; these devices are extremely radiation hard. They were carried out with encouraging electrical characteristics results both before and after irradiation. Beam test results so far have been very promising efficiency values: ~ 99 % and ~97 % before and after irradiation up to fluence of 1 x 10^{16} n_{eq} cm^{-2} [2]. Because 3D fabrication process is more complex and expensive in comparison to the planar one, it is now understood that numerical device simulation has an important role and becomes crucial to design and verify the device operation before fabrication.

The overall aims of this thesis is to reduce the dead area and increase the breakdown voltage for an existing PixFEL planar sensor include a 3D trench implementation using TCAD simulations by Synopsys Sentaurus. The same software will be used also in order to compare the accuracy of different bulk damage models in predicting the leakage current and charge collection efficiency (CCE) of small-pitch 3D sensors irradiated at large fluences up to the maximum value foreseen at the innermost pixel layers at HL-LHC (2×10^{16} n_{eq} cm^{-2}). Results based on two bulk damage models will be analyzed, in comparison with experimental data from 3D diodes measured with a position resolved laser system in order to predict high signal efficiency and charge multiplication effects at high voltage, investigating the different distribution of the electric field and in particular to presence/intensity of the double peak effect.

The overall structure of the study takes the form of four chapters with a general introduction and conclusion.

The first chapter gives a general state of the art on the topic of radiation detector, starting from a simple PN junction, moving to the main principle of photons/ charged particles detection, emphasizing at damages caused by them and finally highlighting the evolution of three-dimensional integration in ICs and its different approaches and its importance in detector technology.

The second chapter begins with a brief description of the European X-ray free electron laser-XFEL. We will then present the study as well as the detector design carried out within the framework of the European PixFEL project. Finally, a new compact border termination for active-edge planar radiation detectors will be presented. A summary of the main conclusions, regarding the performance obtained, in comparison with the existing PixFEL detector, will close this chapter.

The third chapter is composed of two complementary parts. The first one deals with high physics at the LHC, the second one will be devoted to 3D radiation detectors. More precisely the Small-pitch 3D pixel sensors, which are the best candidates for the innermost tracking layers of the major detector upgrades at the High Luminosity LHC (HL-LHC). Some experimental results obtained from our FBK group will be also summarized. This chapter calls for the need of a deep investigation of these results using TCAD simulation in order to explain the evolution of the signal efficiency with voltage at different position within the 3D cell. These results allow bringing also remarkable contribution in the optimization and the design of these devices.

The fourth chapter will investigate in details the different experimental obtained quantities, using two of the most accurate radiation bulk damage models, which predict leakage currents, signal efficiency values and charge multiplication effects at high voltage compatible with the experimental observations.

- ***References:***

[1] G. Rizzo, et al., The PixeFEL project : development of advanced X-ray pixel detectors for application at future FEL facilities, J. of Instrumentation. vol. 10, C02024, 2015.

[2] H. Oide et al., INFN-FBK developments of 3D sensors for High-Luminosity LHC, Nucl. Instrum. Meth. A in press (2018).

Chapter 01

I.1. Introduction

Semiconductor detectors have been attracting considerable interest for spectroscopy applications since 1960. In contrast to ionization chambers which need at least 20 eV, these instruments play a vital role in lowering the required energy to produce electron-hole (3.6 eV) pairs, thereby leading to a much better energy resolution.

In the early 1980s, a significant advance in Si detector technology was attributed to J.Kemmer, who was the pioneer in using the planar fabrication process, which is originating from microelectronics [1]. The two benefits of this technic are in exploitation the passivation properties of Silicon dioxide, which have allowed the thermal budget to be kept to a minimum and enabling electrode fine pitch segmentation, thus a very small leakage currents inside the implanted detectors. Few years later, more sophisticated and accurate detectors such as strip and Silicon drift detectors could be obtained using the same approach, with excellent features in terms of energy, resolution, and stability and radiation tolerance. All these features make these devices very appealing choice for the XFEL applications and the central region of ATLAS experiment (75 % of the area basis) where fewer radiation damage was expected. However, the previously mentioned instrumentations suffer from the serious limitation at high fluencies like in the case of the ATLAS Inner Tracker (ITk) and CMS Silicon Tracker particle detectors.

In the mid-1990s, Sherwood Parker and collaborators shine new light at the proposed 3D radiation detectors through the introduction of the bulk micromachining in combination with microelectronics' very-large-scale integration (VLSI) in the processing. The 3D structure, present 3D array of vertical columnar electrodes arranged in adjacent cells etched perpendicularly to the wafer surface and penetrating through the entire substrate [2]. This architecture offers certainly some advantages with respect to the planar one, making 3D detectors ideal candidates for important applications such as the ones in high energy physics (HEP) at the LHC which will be upgraded to the high luminosity LHC by 2024 (HL-LHC) [3]. These experiments are expected to scale up five to ten times the nominal current luminosity and an integrated luminosity up to 3000 fb^{-1}[4]. The major drawback associated with this enhanced luminosity is the increased radiation damage in particle detectors; this requires the development of new low pitch pixel sensors with very dense pixel granularity features to cope the high particle densities giving also an improved position resolution [5].

The purpose of this chapter is to review the literature up on radiation sensors covering relevant aspects of device physics and simulation, fabrication technologies and design issue, Three-dimensional integration in the ICs, latest experimental results and application fields for both planar and 3D sensors.

I.2. Silicon as radiation detectors

Semiconductor detectors have been attracting considerable interest in particle physics since 1970s. Compared to other materials, semiconductors have special properties making them ideal for such applications, especially Silicon that is the most studied, cheap and abundant on earth. Furthermore, it became the most commonly used material for electronic amplifying components (transistors), and the full microelectronics circuits. Thus, the detector production could be inspired from the existing process technology in microelectronics.

During the last decade, more complex 3D structures have been obtained using this charmed material because of the maturity of processing technology. This offers the production of the extreme radiation hard detectors. What follows is a brief overview of semiconductor physics, it is recommended to review [6], [7], [8] for further understanding.

I.2.1. Basic concepts on semiconductor detectors

I.2.1.1. Semiconductor and Dopants

Understanding almost any type of semiconductor device requires diving in some basic materials properties of semi-conductors and replying some of the knowledge of chemistry or/and physics. Thus, showing how those concepts are extended and applied to real semi-conducting materials.

Semiconductors have a band gap small enough that we can break a few of their bonds, and at reasonable temperatures, it is possible to create some empty states in the valence band and create some electrons in the conduction band. The bandgap of Silicon is 1.12 eV. A semiconductor is called intrinsic when the number of electrons and holes is equal to the intrinsic concentration n_i=n=p, it is given by a simple and it simply gives the probability that a state at a particular energy with respect to the Fermi energy is occupied.

$$\boldsymbol{F(E) = \frac{1}{1+e^{\frac{(E-EF)}{KT}}} \cong e^{-\frac{(E-EF)}{KT}}.} \qquad \textit{I-1}$$

Where E_F, the Fermi energy is the energy at which the probability of a state being occupied is one half. T is the absolute temperature in Kelvin and K is the Boltzmann constant.

In an n-type semiconductor, the Fermi level would be closer enough to the conduction band such that there is a small probability that those states nearer to the conduction band would be occupied. For the p-type semiconductor there is a small probability that the states nearest to the top of the valence band are not occupied, this will give an empty state or a hole that is free to move around and act like a positive charge carrier. The density of free electrons per cubic centimeter in the conduction band related to the Fermi level and the densities of states together. It can be obtained by integrating from the bottom of the conduction band the carrier concentration given by the product of the density of states N(E) in that energy range multiplied by the probability that the state is occupied Fn(E).

$$\boldsymbol{n = \int_{E_C}^{+\infty} N(E)F(E)dE.} \qquad \textbf{\textit{I-2}}$$

By calculating this integral, the density of free electron will be given as;

$$\boldsymbol{n = 2\left(\frac{2\pi m_n kT}{h^2}\right)^{\frac{3}{2}} e^{-\frac{E_C\ -\ E_F}{kT}} = N_c e^{-\frac{E_C\ -\ E_F}{kT}}.} \qquad \textbf{\textit{I-3}}$$

Where m_n is the effective mass of the electron and h is Plank's constant
In the same way, the free holes will be obtained as following:

$$\boldsymbol{p = 2\left(\frac{2\pi m_p kT}{h^2}\right)^{\frac{3}{2}} e^{-\frac{E_F\ -\ E_V}{kT}} = N_v e^{-\frac{E_F\ -\ E_V}{kT}}.} \qquad \textbf{\textit{I-4}}$$

m_p is the effective mass of the electron

Where N_C and N_V are the effective density of states in the conduction and valence band respectively, they depend on the effective mass of electrons and holes. So, the multiplication of electron and hole density at thermal equilibrium gives this simple expression:

$$\boldsymbol{np = {n_i}^2 = N_c N_v e^{-\frac{E_g}{kT}}.} \qquad \textbf{\textit{I-5}}$$

Eg is the gap .

It turns out then that the Fermi energies drop out making the result independent of it. It just depends on the difference between the conduction band and the valence band.

It is possible to make semiconductor devices because of doping, and that is what make semiconductors so useful. The possibility of changing the number of electrons in the conduction band or the number of holes in the valence band by controlling the location of the Fermi energy when adding small fractions of specific impurities (doping). Therefore the extrinsic semiconductors can be n-type with an excess of electrons in the conduction band or p-type with additional holes in the valence band.

The substitution using another atom of a proper lattice atom is followed by the formation of localized energy levels in the bandgap. Furthermore, these energy levels could be whether a donor (E_D) close to conduction band leading to a high concentration of free electrons in the semiconductor or acceptor (E_A) close to valence band, thus, holes treated as a positive charge will be created in the valence band. At room temperature, most of those dopants in Silicon are ionized whether they are donors as Phosphor, Arsenic or acceptor as Boron of group III of the periodic table since the required energy is approximately 0.03 eV.

The charge carriers have a random displacement inside a semiconductor. It is possible to give the charge carriers a direction and producing a flux by applying an external electric field 'E', thus generating a drift current. There is another contribution of current so-called diffusion, it is due to the high probability that carriers cross from the side with highest concentration to the lower one. Consequently, combining the two effects of drift and diffusion, the current densities are expressed as the following:

$$j_n = qn\mu_n E - qD_n \frac{\partial n}{\partial x} \qquad \textit{I-6}$$

$$j_p = qn\mu_p E + qD_p \frac{\partial p}{\partial x} \qquad \textit{I-7}$$

Where q is the elementary charge electron, μ_n is the electron mobility, D_n the diffusion coefficient. The corresponding symbols for holes are μ_p, D_p.
Einstein equation associates the Mobility and diffusion by the following expression:

$$D_{n,p} = \frac{kT}{q}\ \mu_{n,p}. \qquad \text{I-8}$$

I.2.2. P-N diodes and relevant concepts for Silicon detectors:

The reverse-biased p-n junction is in reality the building block of every Silicon sensor; it typically consists of Silicon n-type (cathode) and p-type (anode) regions doped with donor atoms and acceptor ones respectively. Electrons move naturally from the n-side of high concentration to the p-side of low concentration leaving a positive charge. This phenomena so-called diffusion, in the same vein, the holes diffuse across the junction to the n-side leaving a negative charge. A region free of mobile charges is created near the junction, it is called space charge region (SCR). An electric field is created within the SCR.

The electric field and electrostatic potential distributions around the PN-junction can be obtained from the following Poisson's equation:

$$\frac{\partial^2 \varphi}{\partial x^2} = -\frac{dE}{dx} = -\frac{\rho(x)}{\varepsilon_s}. \qquad \text{I-9}$$

Where φ and **E** describe the electrostatic potential and electric field respectively, ρ is the charge density and εs is the dielectric constant of Silicon.

Figure I.1 displays the energy band diagram after combining the p-type and n-type materials.

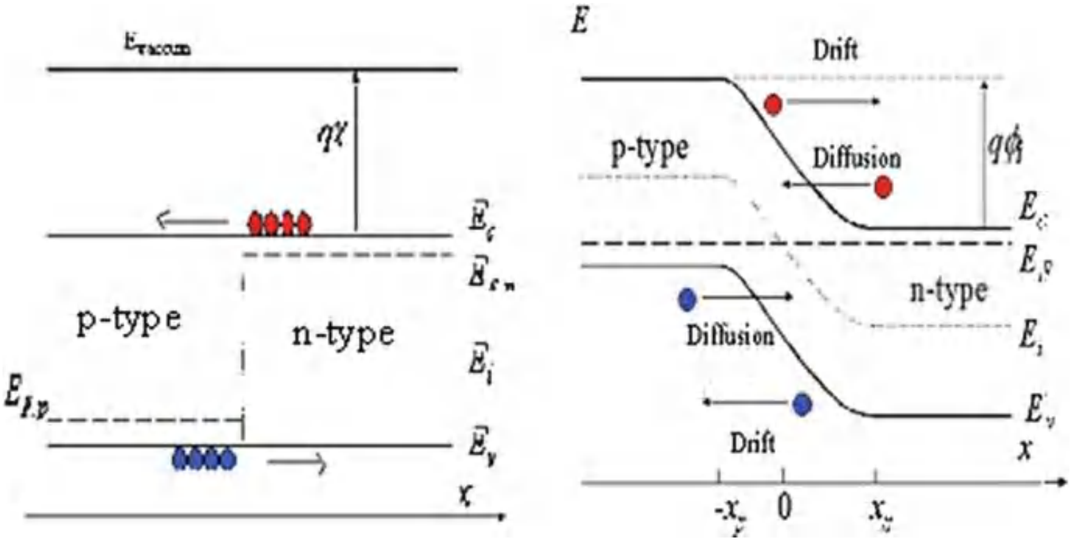

Figure I.1: A schematic of the energy band diagram after combining the p-type and n-type materials.

The following equation for built-in potential can be derived if all donors and acceptors are ionized:

$$\varphi_0 = \frac{kT}{q} ln\left(\frac{N_A N_D}{n_i{}^2}\right). \qquad \text{I-10}$$

Applying an external electric field is required in order to detect the radiation-induced charges. **Figure I.2** shows the effect of biasing a p-n junction on the generated current.

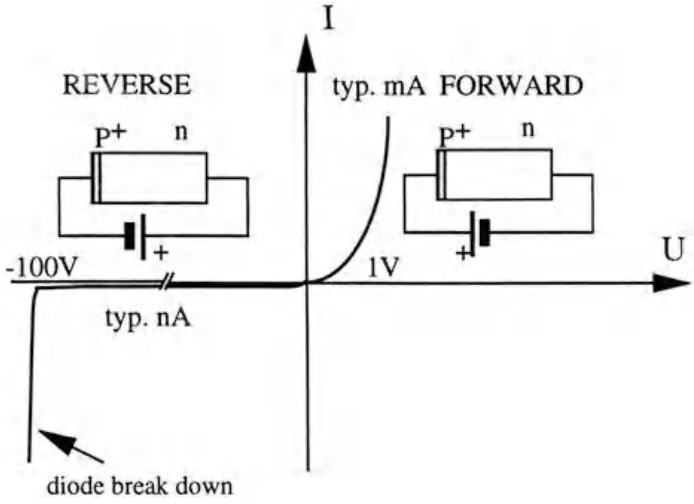

Figure I.2: Current-voltage characteristics of a diode under forward and reverse biasing.

V$_{\mathbf{bias}}$ and $\boldsymbol{\varphi_0}$ must be in the same direction. Thus, the depletion region width will be described as the following:

$$w = \sqrt{\frac{2\varepsilon_s}{q}\left(\frac{1}{N_A}+\frac{1}{ND}\right)(V_{bias}+\varphi_0)}. \qquad \text{I-11}$$

N_A and N_D are the concentrations of acceptors and donors respectively.

Since the bulk of Silicon detector is typically low-doped (10^{12} cm$^{-3)}$, whereas implants acting as electrodes are generally highly doped (10^{18} cm^{-3}), the depletion region will extend more to the bulk where the concentration is much lower. For an n-type bulk material, the width of the depletion layer can be simplified as the following:

$$w_{depl} \cong x_n = \sqrt{\frac{2\varepsilon_0\varepsilon_{si}}{qN_D}V_{bias}} \qquad (N_A \gg N_D). \qquad \text{I-12}$$

Inside a typical p-n junction, the maximum value of electric field can be estimated as:

$$E_{max} = \frac{2V_{bias}}{w} \cong \sqrt{\frac{2qN_D}{\varepsilon_s}V_{bias}}. \qquad \text{I-13}$$

The charge distribution, electric field and electrostatic potential plot of a one-sided abrupt P+N junction are depicted in **Figure I.3**

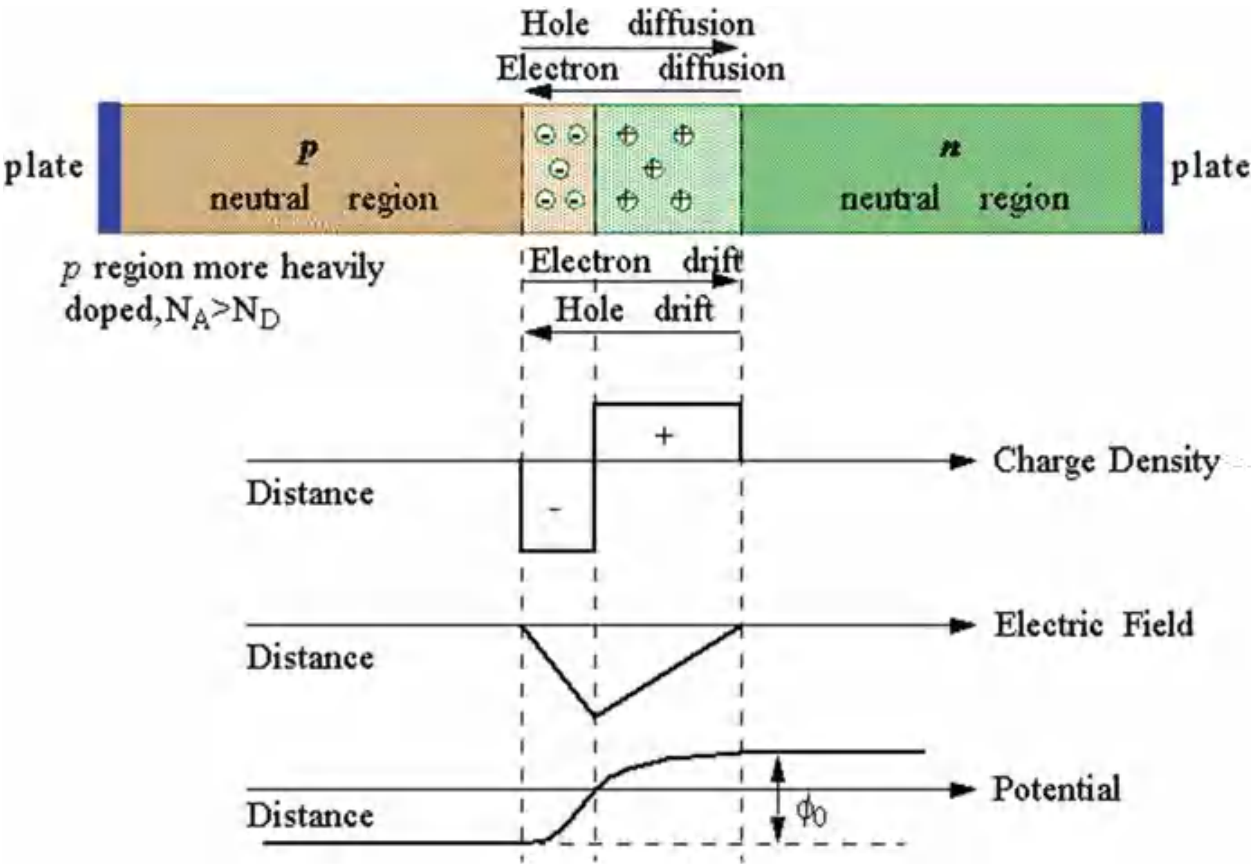

Figure I.3: Forming of the space charge region without any external field: In the picture from top to bottom, a simple charge configuration, the charge density, the electric field, the electric potential

The full depletion voltage (V_{fd}) of a detector with thickness (d) is formulated under the same simplifying assumptions as:

$$V_{fd} \cong \frac{qN_D d^2}{2\varepsilon_0\varepsilon_{si}}. \qquad \textbf{I-14}$$

This value is required to extend the (SCR) to the entire sensor thickness. The device is so – called over-depleted only if the applied voltage exceeds the full depletion voltage.

Within the device, the dark current has several components: (i) free carriers from non-depleted region into the SCR (ii) the thermal contribution at generation-recombination centers at either the surface and in the depleted bulk of the device.

The leakeage current density approximation of a reverse biased P-N junction can be given as the following:

$$J_{vol} \cong -\frac{qn_i w}{\tau_g} \cong -\frac{n_i}{\tau_g} \cong -\frac{n_i}{\tau_g}\sqrt{\frac{2q\varepsilon_s}{N_D}V_{bias}} \qquad \textit{I-15}$$

Where τ_g is the carrier generation lifetime. The temperature has a significant impact on the leakage current value since whether n_i and τ_g essentially depend on device operating temperature. Detectors requires cooling conditions in order to minimize the leakage current. The following equation from [10] set out to predict the leakage current at temperature T_2 with reference to the leakage current T_1 :

$$\frac{I(T_2)}{I(T_1)} = \left(\frac{T_2}{T_1}\right)^2 exp\left[-\frac{E_{eff}}{2k}\left(\frac{T_{2-}T_1}{T_1T_2}\right)\right] \qquad \textit{I-16}$$

where Eg=1.21eV is the effective gap energy, k is the Boltzmann’s constant. A possible approximation is that the volume current doubles every 7 K.

At high reverse bias, the free carrier that is thermally generated will gain a lot of kinetic energy because of the high electric field. If it collides with the Silicon lattice, there is a chance that it can break a Silicon bond and free up an additional electron that will be subjected to the same process; this multiplication process is well known as impact ionization. The Avalanche breakdown occurs when this process goes to infinity due the high electric field, the leakage current will be large enough leading to uncontrollable self-heating mechanism known as **thermal runaway**.

The approximation of the maximum operating voltage can be given as the following equation:

$$V_B \cong \frac{\varepsilon_s}{2qN_D}{E_B}^2 \qquad \textit{I-17}$$

E_B =4×10^5 V/cm, it describes the critical electric field for avalanche multiplication in Silicon at T=300°K.

The Silicon bulk devices capacitance can be estimate as the following:

$$C_{bulk} \cong \begin{cases} A\sqrt{\frac{\varepsilon_s}{2\mu\rho V_{bias}}}, & V_{bias} \ll V_{fd} \\ A\frac{\varepsilon_s}{w_{depl}} = const, & V_{fd} > V_{bias} \end{cases} \qquad \textit{I-18}$$

From the previous approximation, it is possible to find the full depletion voltage V_{fd} when the bulk capacitance saturates to its minimum.

I.2.3. Silicon as a Detector Material:

Since many years, Silicon sensors have been dominated the field charged particles and High-energy-X-rays detection, which can vary depending on both the detection material and the radiation type.

I.2.3.1. Interaction of Charged particles with

The Silicon sensor is a reverse-biased semiconductor junction, which has an extended depletion region throughout the entire structure because of its high resistivity. These features free the device from carriers. When charged particles move through matter, they lose a part of their energy through elastic collisions with electrons. This process ionizes the lattice atoms and frees some charges, which play the key role in detection operation. The created electron-hole-pairs separated by the applied electric field and drift toward the readout electrodes, which will be detected as signal. **Figure I.4** provides the working principle of a Silicon stripe sensor that is based on p-n junction structures. More details about the features of p-n junction will be given in the following chapter.

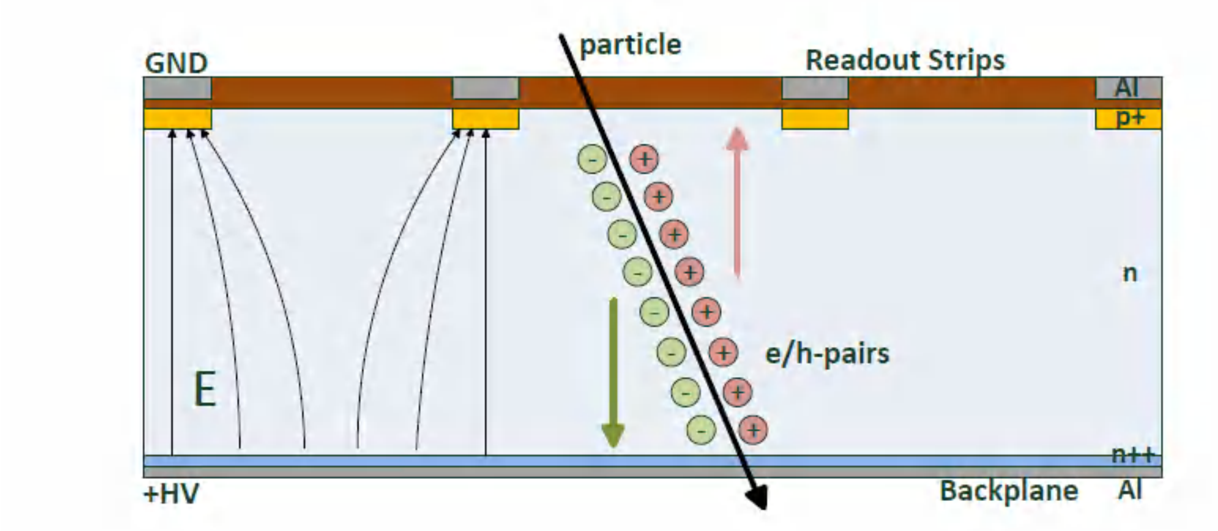

Figure I.4: The working principle of a Silicon strip sensor

The average energy loss per distance can be estimated using the Bethe-Bloch formula:

$$-\frac{dE}{dx} = 4\pi N_A {r_e}^2 {m_e}^2 c^2 z^2 \frac{Z}{A}\frac{1}{\beta^2}\left[\frac{1}{2} ln\left(\frac{2m_e c^2\beta^2\gamma^2 T_{MAX}}{I^2} - \beta^2 - \frac{\delta(\gamma)}{2}\right)\right] \qquad I\text{-}19$$

Where z represents charge of the incident particle, Z the atomic number, N_A is Avogadro′s number, A is the atomic mass of the considered material, $\mathbf{4\pi m_e c^2 = 2.817 \times 10^{-13}}$ cm , m_e the electron mass, $\mathbf{r_e}$ is the classical electron radius, $\mathbf{T_{MAX}}$ the maximum kinetic energy that can be imparted to a free electron in a single collision, I the mean excitation energy ;$\boldsymbol{\beta} = \mathbf{v/c}$, the velocity of a traversing particle in units of speed of light, $\boldsymbol{\gamma} = \frac{\mathbf{1}}{\sqrt{\mathbf{1-\beta^2}}}$, $\boldsymbol{\delta}$ the density effect correction.

Figure I.5 displays the stopping power of different particles. What can be clearly seen from this curve is that Particles providing such minimum values of energy loss present at $\boldsymbol{\beta\gamma\approx 3}$. Minimum ionizing particles (MIPs) are considered as particles that have such kind of energy loss which each system must have an intrinsic noise low enough to detect. Some statistical fluctuations in the collision number happen when a particle interacts with a material. Generally, this phenomenon is modeled on a Poisson distribution. Simultaneously, another phenomenon of energy transfer per scattering occur, this later described by “straggling function".

Rarly, the interaction produces δ-rays or δ-electrons, which provide enough energy to become ionizing particles. This phenomenon affects the symmetry in the collected spectrum, associated with a longer tail toward higher energies. This consequent asymmetry spectrum distribution is referred as the Landau distribution [11]. Generally, the most probable value of the energy transfer is around 30% smaller than the average value. The average energy required to create an electron-hole pair in Silicon is 3.6 eV, around three times the band gap, this is because a portion of energy is needed for phonons generation. Therefore, the most probable signal for a MIP is 72 electron-hole-pairs per micrometer. Thereby, the total collected charge for a device with an active thickness of 300 µm is around 21,600 e-h pairs [12].

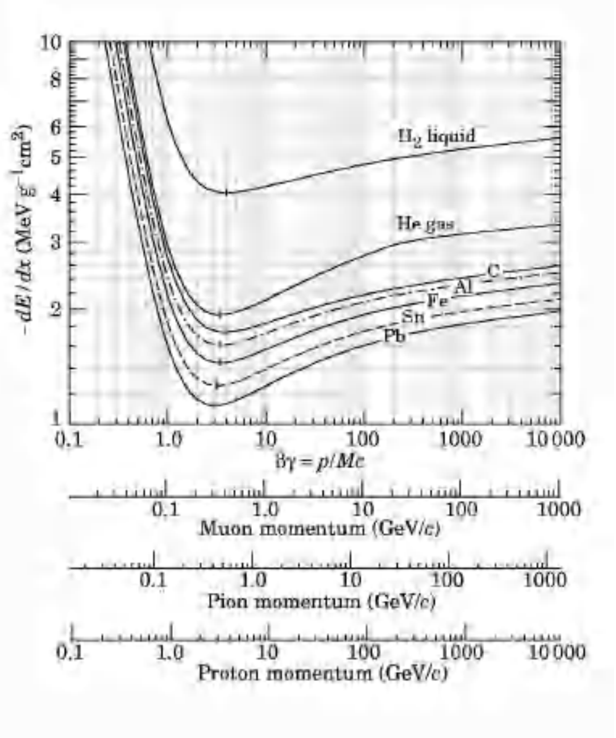

Figure I.5: The mean Energy loss of different particles in different materials as a function of their energy

When dealing with charged particles, the so-called Multiple Scattering is an important phenomen to take into account: the Colomb interaction with the nuclei of the material makes the particle's moving through the material trajectory scattered several times by small angles. In addition to charged particles, the Silicon can be sensitive to the Electromagnetic radiation ranging from visible light to the X-ray, this feature makes it very appealing for some other applications such as cameras or medical imaging.

I.2.3.2. Interaction of Photons with silicon

The interaction between photons and Silicon can be occurred in three various processes: (i) **photoelectric effect**, (ii) **Compton effect and** (iii) **pair production**. Whereas the photon is entirely absorbed in both photoelectric absorption and pair production modes, the Compton mode is scattered by a large angle. The relation between the photon penetrating through the material and the depth (x) of active thickness is defined by Beer's law:

$$\boldsymbol{I(x) = I_0 e^{-x/\mu}} \qquad \textbf{\textit{I-20}}$$

Where I_0 is the beam intensity, μ is the attenuation length. The probability of interaction between photon and 300 µm Silicon is shown in **Figure I.6.** Simultaneously it compares the Silicon with high-Z materials as in the case of CdTe.

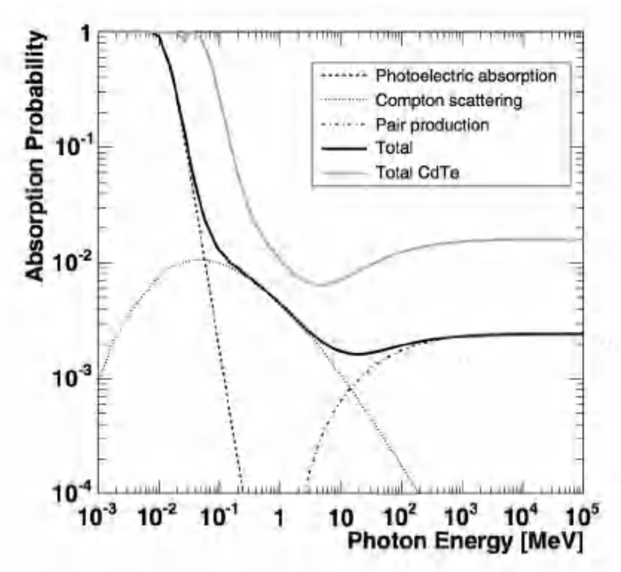

Figure I.6: The mean energy loss of different particles in different materials as a function of their energy [13].

The passing particle creates a moving charge carrier that drifts inside an electric field leading to induce electric charge on the detector electrodes. Then, an output signal is obtained by the conversion of this collected charge is the readout part. This induced charge Q can be calculated using Ramo's theorem by a free moving point charge q [14], only one sensor's electrode is selected.

The following charge is induced by a charge moving from point $\overline{x\iota}$ to a point $\overrightarrow{xf}$:

$$Q_L = \int_{\vec{x}_i}^{\vec{xf}} q\overrightarrow{E_0}.d\vec{x} = -q[\phi_0(\overrightarrow{xf}) - \phi_0\ (\overrightarrow{x_\iota})] \qquad \text{I-21}$$

Where $\overrightarrow{E_0}$ and ϕ_0 are the weighting field the weighting potential respectively, which can be obtained by applying the unit potential to a chosen electrode and keep all others grounded. Consequently, all charges are removed. The solution can be done for the given configuration by the Poisson equation (where the electrodes layout is known). Thus, the weighting potential values confined between 0 and 1. The induced charge on the collection electrode can be described as a fraction of the free moving charge.

I.2.4. Magnetic Field Effects:

An additional advantage of using semiconductors detectors is the ease of operation within magnetic field to allow measurements of particles momentum. Few consequences though need to be recognized and taken into consideration. The magnetic field affects in addition to the particle penetrating the detectors, the free charge carriers that move within the Silicon sensor. Thus, the Lorentz force deflects the generated electron-hole pairs, which are separated by the electrostatic force and moving toward the electrodes.

$$\boldsymbol{F} = \boldsymbol{q}(\boldsymbol{E} + \boldsymbol{v} \times \boldsymbol{\beta}). \qquad \textit{I-22}$$

This leads to a lateral displacement of the charge from the electric field lines described with an opening angle Θ_L vary typically between a few degrees and 20° and described as the following.

$$\tan \emptyset_{L,n} = \mu_{H,n}\, \boldsymbol{\beta}_{\perp} \qquad \textit{I-23}$$

$$\tan \emptyset_{L,p} = \mu_{H,p}\, \boldsymbol{\beta}_{\perp} \qquad \textit{I-24}$$

Where the superscript H stands for "Hall", indicating that the Hall mobility differs somewhat from the used drift mobility, $\beta_{\perp}$ is the magnetic field component.

The generation and recombination of carriers plays a crucial role in the efficiency of the system in the real environment. The band to band transition (electron, hole) for indirect semiconductors as Silicon is not simply given by the width of the Bandgap as in the case of direct semiconductors. Since the top of the valence band and the bottom of conduction band are placed at different momenta, it is not possible to conserve both energy and momentum without additional momentum (lattice interactions).

The thermal generation and recombination in Silicon described by Shockley-Read-Hall (SRH) process [9] , which uses localized energy levels within bandgap, primarily caused by lattice imperfection or unwanted impurities in Silicon (e.g. Au, Cu, Fe). These localized band-gap states directly influence the carrier lifetimes. For more detail review [8].

In order to reduce thermal generation, a very high purity of the substrate and the efficiency of the manufacturing process are required.

I.3. Radiation Damage in Silicon:

When Silicon radiation detectors operate in harsh radiation environment, expanding our understanding of the impact of radiation damage on the detector performance plays a vital role to their successful operation. The effects of radiations on Silicon sensors may be divided according to their location in two main categories:

1) Surface damage where all defects are located nearby the Silicon crystal surface or the interface area between the Silicon and passivation layer. This causes modifications in the breakdown properties, surface recombination and inter-electrode isolation.

2) Bulk defects where defects are located deeper within the Silicon sensor effecting the full depletion voltages, charge trapping and the leakage currents. The so-called Non Ionizing Energy Loss (NIEL) hypothesis explains the production of bulk damage.

I.3.1. Surface Damage:

Silicon dioxide (SiO_2) is widely-used as a surface layers in Silicon devices. The damage done on these layers causes the majority of the surface damage induced in Silicon devices. The two common defects are **the Interface trap charge (Interface states)** : positive or negative charges produced by structural defects, oxidation defects, metal impurities or radiation induced bond breaking, it contributes to surface recombination **leading to higher leakage current**; it is located at the interface of Si-SiO_2. **The oxide charge**, which plays a crucial role for the device performance, it may be divided to three main sub-groups:

Fixed oxide charge: The electric field is modified by near the Si-SiO2 interface, which attract electrons close to the interface.

Oxide trapped charge: Positive or negative charge resulting from avalanche injection, ionizing radiation or other mechanisms, it is possible that these defect annealed at low temperature.

Mobile oxide charge: resulting from ionic impurities (Na, Li and possibly H).

Figure I.7 shows the mechanisms of formation of oxide charges with a density (N_{ox}) and interface traps with density (Nit) in a positive biased MOS capacitor. Both defects induced by X-ray ionizing radiation, which depends mainly on dose. More details will be discussed in chapter 2.

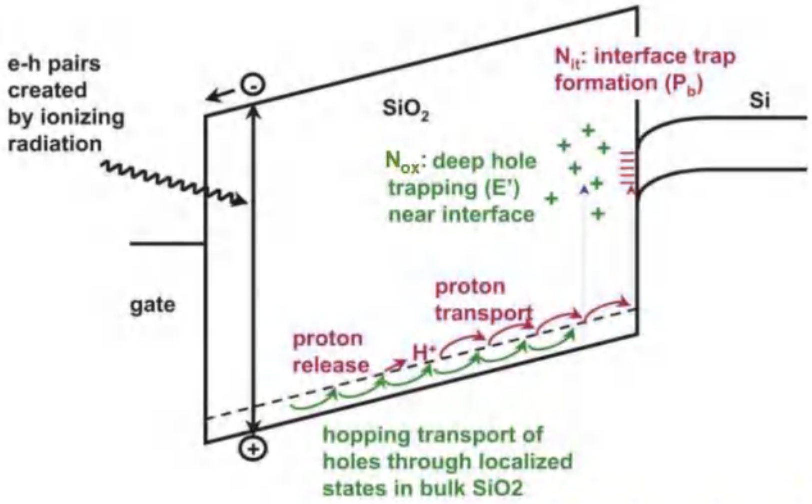

Figure I.7: Mechanisms of formation of oxide charges and interface traps, shown in band diagrams of SiO2, Si-SiO2 interface and Si, [15].

The radiation effects the intrinsic properties of these defects [16]. When a particle passes through the SiO2 layer with the required energy, electron-hole (e-h) pairs will be generated then most of these charges will recombine while a fraction of them does not.

Since electrons and holes have very different mobility values (μ_n=20 cm^2/V.s) (μ_p=2x10^{-5} cm^2/V.s) respectively, electrons can drift too fast, while holes diffuse into interface traps, leading to an increase of the total oxide charge. Moreover, the radiation on SiO_2 increases the interfaces states concentration leading to higher surface recombination velocity and leakage current. More details about the evolution of these defects with radiation fluence can be found in [17]. Figure I.8 displays the variety of surface recombination and oxide charge concentration according to the radiation fluence. Radiation causes an enhancement on the accumulated Total Ionizing Dose (TID) by at least one order magnitude in case of no biasing, whereas, in the biasing condition case the oxide charge could be enhance to further values.

What can be also clearly seen from this Figure is that the oxide charge saturation after certain accumulated TID. This is because of the dangling bonds of oxide are fully terminated. In contrast, the leakage current is proportional to the ionizing radiation damage because of the surface generation.

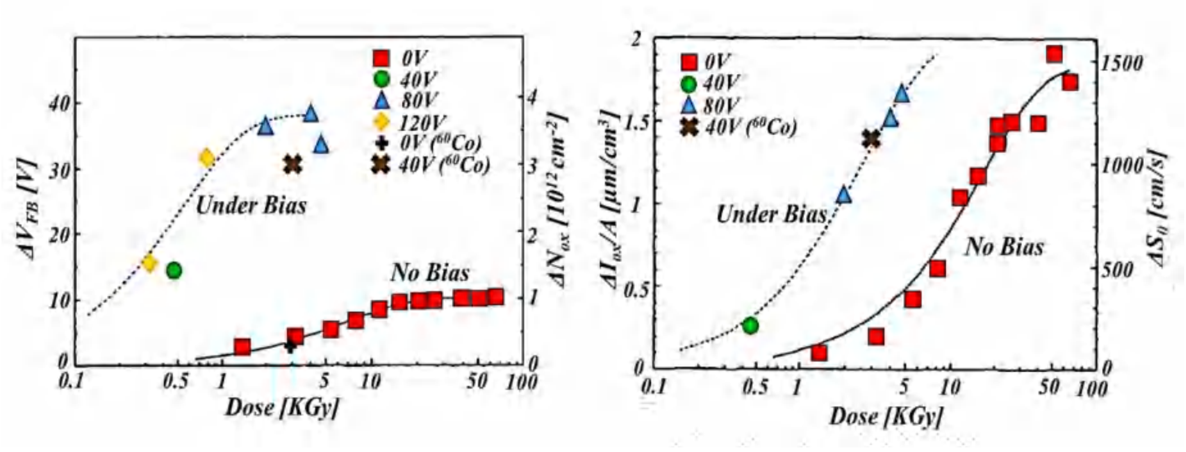

(a) (b)

Figure I.8: MOS with SiO2 dielectric layer under proton irradiation: a) the oxide charge enhancement at different applied voltage condition at accumulated TID, b) the leakage current enhancement at different applied voltage condition at accumulated TID. (X) Is the data relevant to ɤ-ray irradiation with 60 Co source [16].

I.3.2. Bulk Damage:

The passing particle makes damage to the bulk of Silicon detectors mainly characterized by the loss of the energy within the Silicon lattice; this is due to several collision with atoms. When the particle's energy exceeds the displacement threshold energy (Ed ~ 25 eV), the Primary Knock-on Atom (PKA) is displaced, resulting the creation of Vacancy-Interstitial (V-I) pairs (Frenkel-defect) [16].

The required neutron's energy to such a point defect is around 175 eV or more, whereas, electrons need at least 260 KeV to do so [18]. At lower energies, the only created defects are the well-known Primary Knock-on Atoms (PKAs). Nevertheless, if the PKA travels within the crystal with sufficient energy, further Frenkel defects will be created. If the PKA's energy is high enough, clusters will be formed. Generally, they are formed when almost Silicon's atom energy is lost. They are usually found at the end of the PKA's path. The so-called secondary knock-on atoms are additional defects created only at very high energies by the point defects created by the PKA. If the PKA has an energy about 50 KeV, it can create around 1000 additional defects pairs, nearby 600 of them will recombine again. The simulation in Figure I.9 shows the defects created by a PKA carried an energy of 50 KeV. For 1 MeV neutron scattering in Silicon, this is a typical energy. What can be clearly seen in this Figure is the tree-like structure and several sub-clusters. The secondary knock-on atoms with lower energy create the sub-clusters. A PKA carried higher energy than the previous one will create more branches [19].

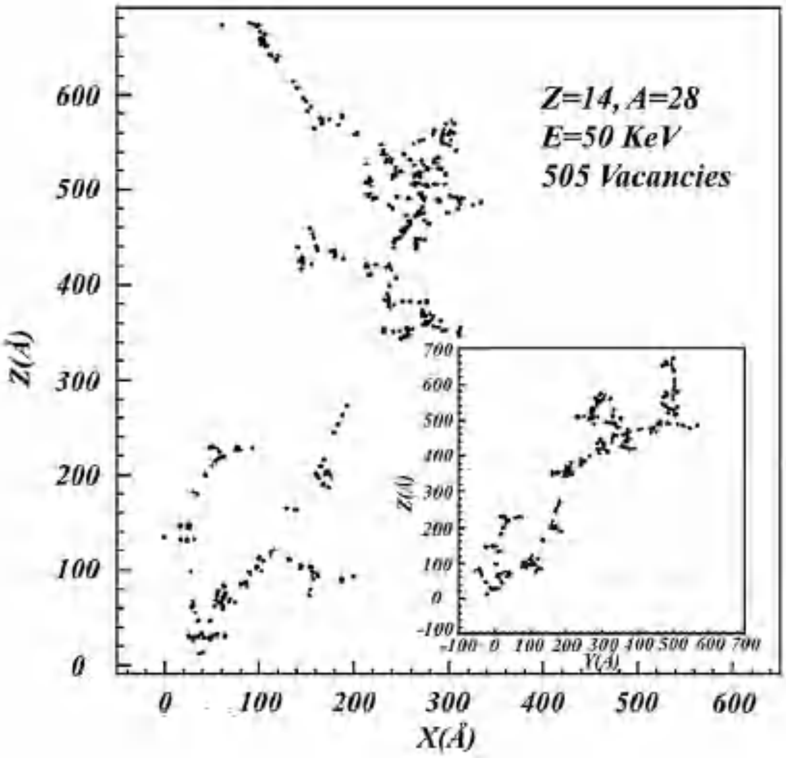

Figure I.9: Simulated point and cluster defect in Silicon by PKA of 50 KeV. The inset Figure 1.9 represents the transverse projection [18].

For a comparative analysis of irradiated samples, the Non Ionizing Energy Loss (NIEL) hypothesis is used. The damage produced by highly energetic particles can be scaled to the same damage that would be caused by 1MeV neutrons using the same equation: $\emptyset_{eq} = k\emptyset_p$ Where k is the hardness factor, $\emptyset_{eq}$ is the neutron equivalent fluence and $\emptyset_p$ presents the total fluence.

I.4. Damage Effect on Sensor Performance:

Since Silicon sensors are operated in highly radioactive environments, their performance is limited by the accumulation microscopic defects. There are three crucial properties for Silicon detectors:

When the recombination-generation centers increases, the leakage current will increase leading three mains changes: the signal to noise ratio, the power consumption and the detectors cooling systems.

The defects density affect the effective doping concentration, thus, the depletion voltage will be affected also. The type-inversion is an important phenomenon occurs in sensors of n-type substrates; it is due to highest number of p-type defects compared to the n-type ones. The increase of the trapping centers may have contributed to decrease the Charge collection efficiency. This lead to performance degradation of the detector in terms of resolution.

I.5. Three-dimensional integration in the ICs:

Inside electronics devices there are many small semiconductor chips, they need to be protected from the damaged getting from handling or assembling these devices. Moreover, they require providing some electrical connections between different chips. Making semiconductor packaging and interconnect solutions that were smaller, thinner, higher performance, higher reliability and in many cases lower cost becomes very important. 3D interconnect is more efficient and wonderful technology, it should drive the semiconductor industry and more broadly the electronics industry in the few coming years.

I.5.1. Limitation of conventional technologies:

In the last 50 years, Moore’s law has worked fantastic for the industry, and it has really enabled all of the electronics that we see and utilize every single day. This law is about doubling the transistors density every 18 to 24 months. The issue is we are starting to come up against fundamental limits , we just can't make these features much smaller , so the industry is moving away from two-dimensional approach (Moore’s law) , to a three dimensional approach to exploit the volume. The paths of microelectronics technology evolution are shown in Figure I.10

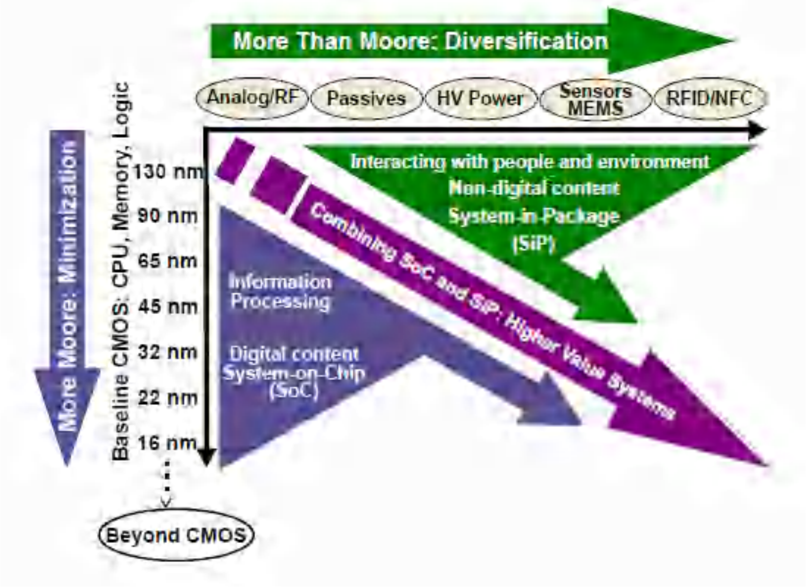

Figure I.10: Moore's Law and its perspectives: 'More Moore' focuses on component miniaturization, 'More Than Moore' focuses on functional diversification [20].

The first "More Moore" approach consists of the miniaturization of transistors based on CMOS (Complementary Metal Oxide Semiconductor) technology. This approach proposes to bring together several functions carried out in the same technological node. Mainly allowing the performance of the circuits to be increased. At the same time, the emergence of other 'More Than Moore' approaches and Beyond CMOS have opened up horizons for the miniaturization of systems. Semiconductor industries are working a lot on this path through the diversity of components and on the combination of SoCs (System on Chip) and SiP (System in Package) in order to optimize their components .

I.5.2. System on Chip (SoC):

SoC is an integrated circuit that combines components of various electronic systems on the same surface to achieve a common goal. All the components of the SoC are designed from the same node technological as shown in Figure I.11. SoC can be comparable to general-purpose computer because it can have many or even all the components that a general-purpose computer has ,it's just much smaller, SoC' s have a lower manufacturing cost because various electronic components are placed into one tiny chip. Some SOC can have reprogrammable Hardware if the chip has an FPGA integrated.

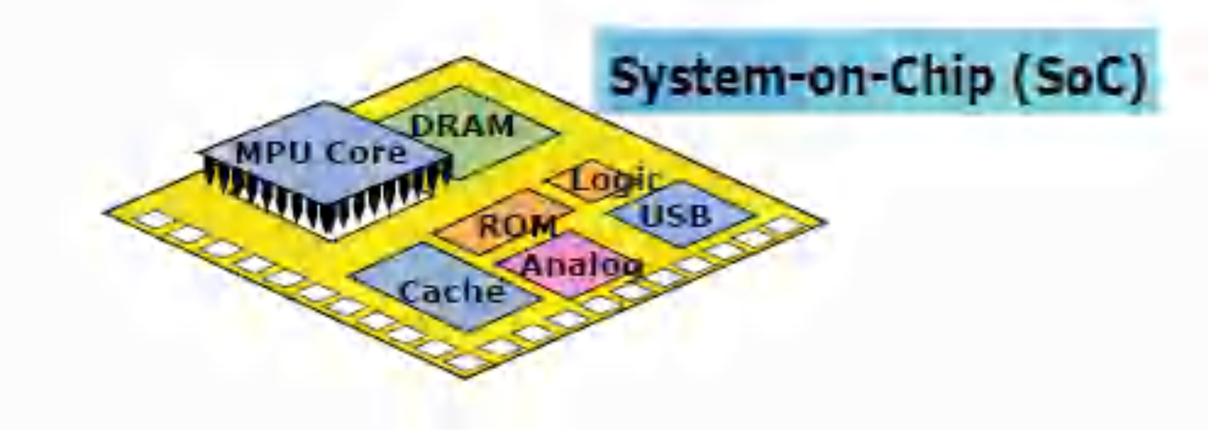

Figure I.11: Elements can be grouped together on the same chip of a SoC system.

I.5.3. System in Package (SiP):

The system in package is a complete circuit (logic circuits, memories, ASICS, microcontrollers, etc.) modeled in a package as it is shown in Figure I.12

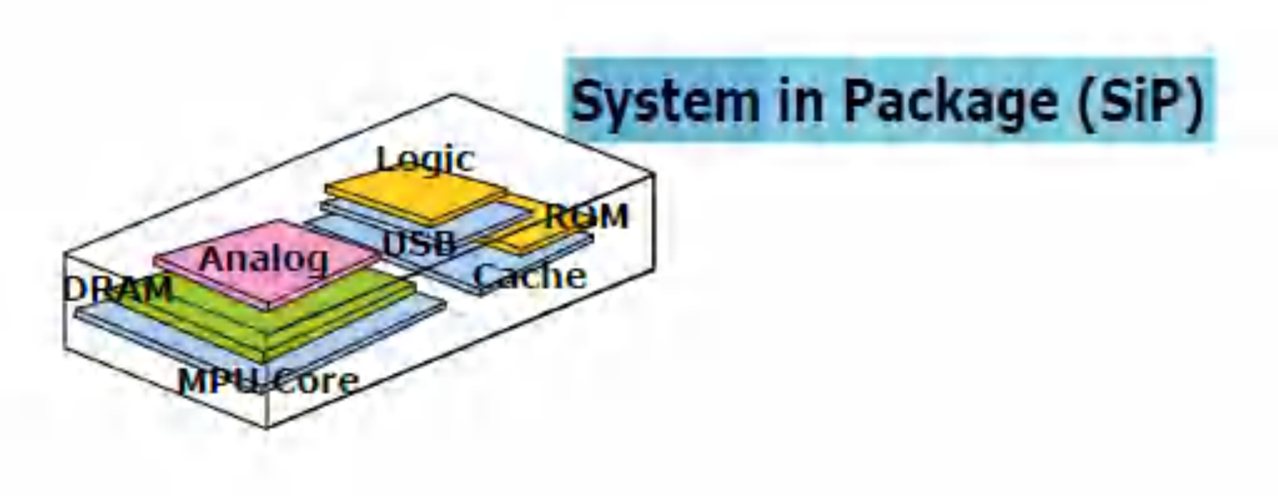

Figure I.12: Set of elements can be grouped together on the same chip of a SiP system.

It is far less sensitive to incorrect placement. Therefore, it provides more accurate and reliable measurements it can be accommodated inside a completely / molded package this airtight assembly resists the entering of liquids, and is perfectly suitable for the harshest environments. In addition, a system in package is flexible in its installation and orientation, for example, it can be bent along two axes, which allow a variety of positioning. Silicon chips can be stacked using either by wire bonding, or by flip chip technology as can be seen in Figure I.13

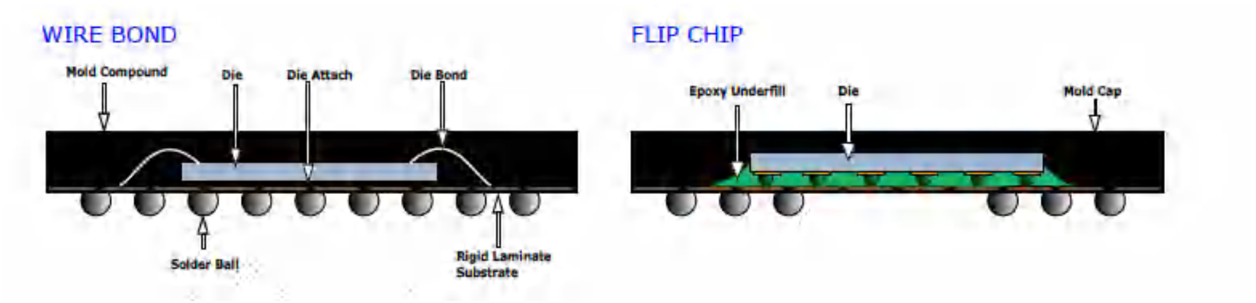

(a) **(b)**

Figure I.13: a) Wire bonding technic, b) flip-chip technic

I.5.3.1. The wire bonding:

It is one of the widely-used technique for the electrical connection between chips in the industrial. The main interest of this technique is to make the superposition of several electronic chips with a large number of I / O connections, all this is done at a reduced price. However, since the cable connections are at the periphery of the chips, in order to avoid short circuits, this requires additional dedicated space.

I.5.3.2. The flip chip:

It is kind of solder balls used to connect a semiconductor chip to some type of board, which might be in a cell phone, laptop….etc. Therefore, there is a different technique for increasing the number of connections in a given area, in the case of conventional flip chip technology; it might get approximately 45 contacts per square millimeter, while on the micro pillar technology it is possible to do a significant jump to 625 contacts per square millimeter. As an example, the FE-I4 readout chip is used to cope the (IBL) requirements. It was designed using the flip chip technic in a 130 nm feature size bulk CMOS process and with a pixel size of 250 x 50 μm^2. Figure I.14 provides the size reduction of pixel from about 100-µm pitch (the FE-I4 readout chip) to vary small pitch in the order of 2µm.

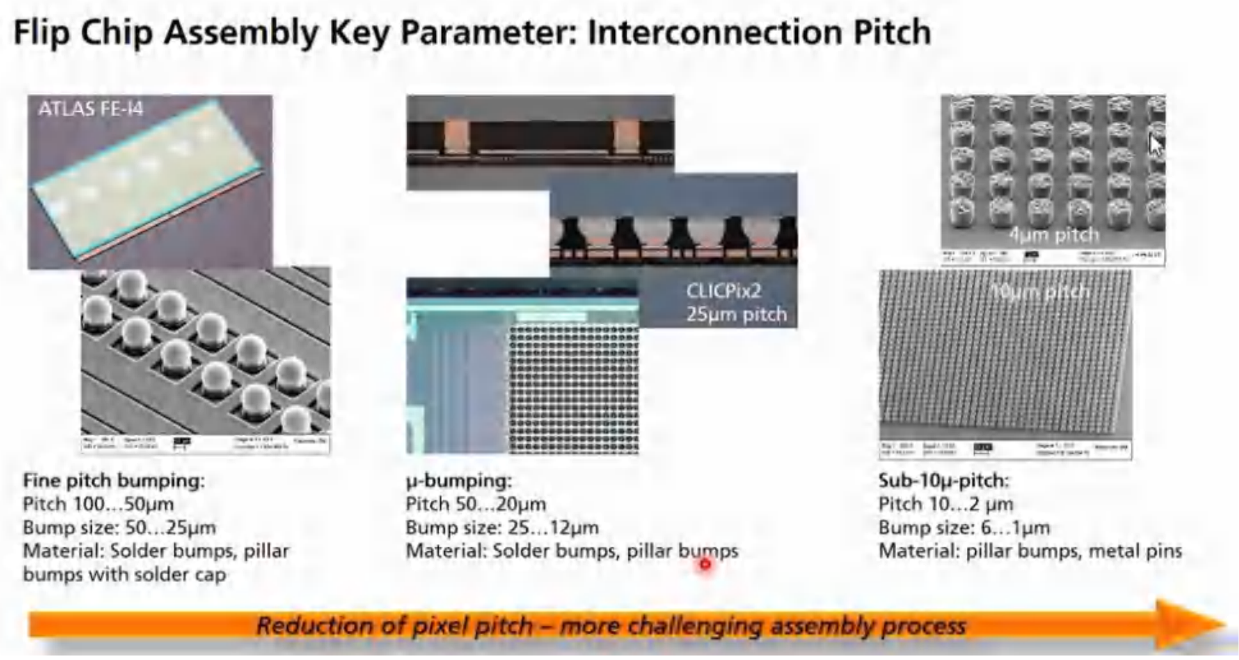

Flip Chip Assembly Key Parameter: Interconnection Pitch

Fine pitch bumping:
Pitch 100…50µm
Bump size: 50…25µm
Material: Solder bumps, pillar bumps with solder cap

µ-bumping:
Pitch 50…20µm
Bump size: 25…12µm
Material: Solder bumps, pillar bumps

Sub-10µ-pitch:
Pitch 10…2 µm
Bump size: 6…1µm
Material: pillar bumps, metal pins

Reduction of pixel pitch – more challenging assembly process

Figure I.14: The flip chip technic and its impact on pixel pitch.

I.6. Integration 3D:

Conventional integrated circuit architectures in terms of 2D planar technology are now constrained, both technologically for the realization of future generations of components and conceptually due to the growing complexity of circuits. 3D electronics used vertical interconnect between the IC layers, this makes the electronics faster, denser, cheaper with a very lower power due to lower interconnect capacitance. Furthermore, it is possible to integrate dissimilar technologies (sensor, analog, digital, optical) as it shown in Figure I.15 and Figure I.16.

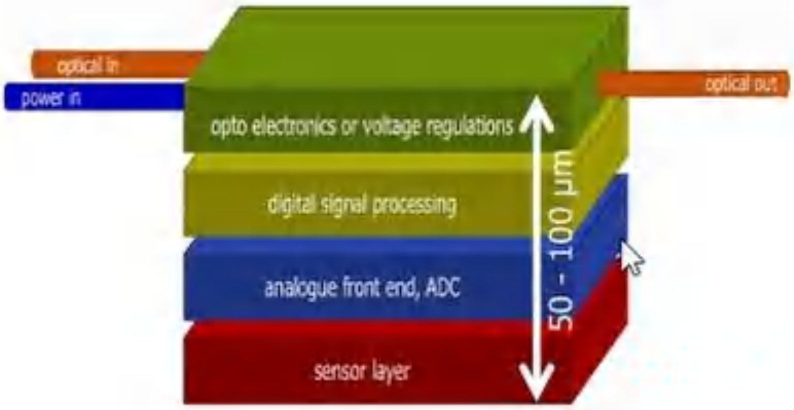

Figure I.15: A schematic of 3D dissimilar technologies integration.

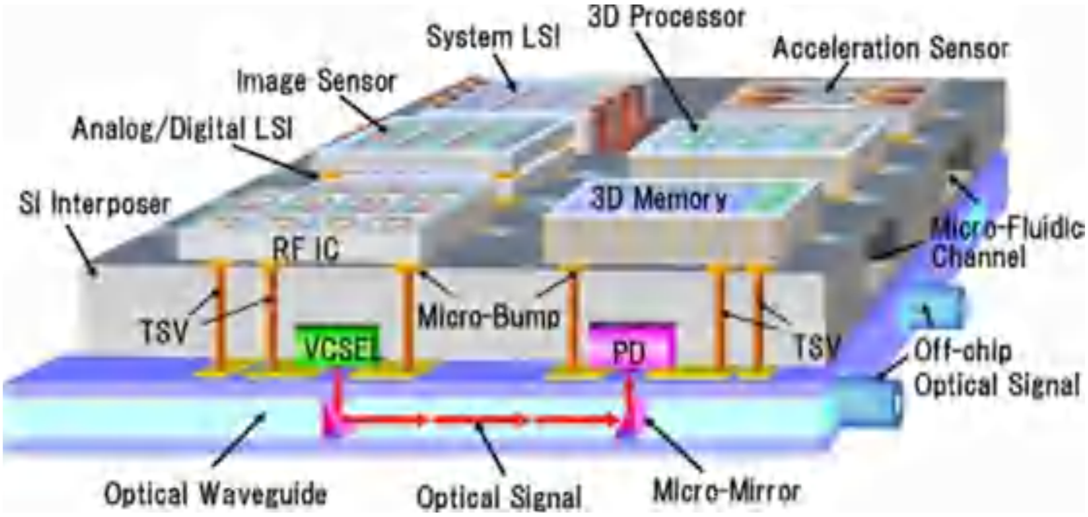

Figure I.16: Conceptual 3D integrated sensor module for intelligent vehicle applications. This heterogeneous integration includes both electrical and optical interposer substrates [21].

Figure I.17 presents a simple configuration of a 3D-SiP circuit assembled vertically with two chips stacked on top of each other. The bottom chip is made with flip-chip using micro bumps, while the top one is connected to the packaging substrate with wire bonding technique.

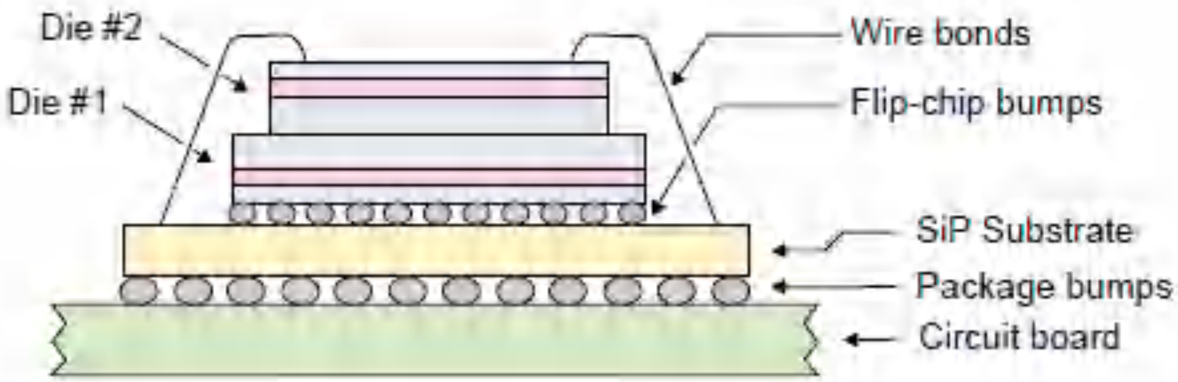

Figure I.17: Example of 3D circuit.

The use of the third dimension in integrated circuits is constantly evolving with the use of new interconnection processes. Thus, a promising path has emerged using short electrical connections or Vias between electronic components, directly through the different layers. These last ones are well known as **Through Silicon Vias** (TSVs). Using this configuration of vertical connection between the different Silicon layers has become one of the best choices of 3D integration (Figure I.18).

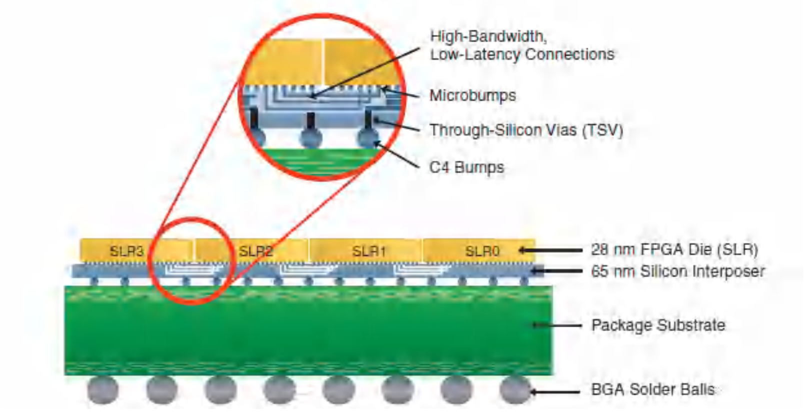

Figure I.18: 2.5D SiP integration using TSV and micro-bumps [22]

About 15 years ago, 3D technologies aroused a lot of interest in view the VERTEX detectors design and readout electronics. The pixel sensors has been working with several companies providing 3D integration technologies (Through-Silicon Vias, low mass bonding…..) Figure I.19 presents a hybrid detector where the electronics chip and the sensor have the same pixels size, bonded to each other by means of bump contacts.

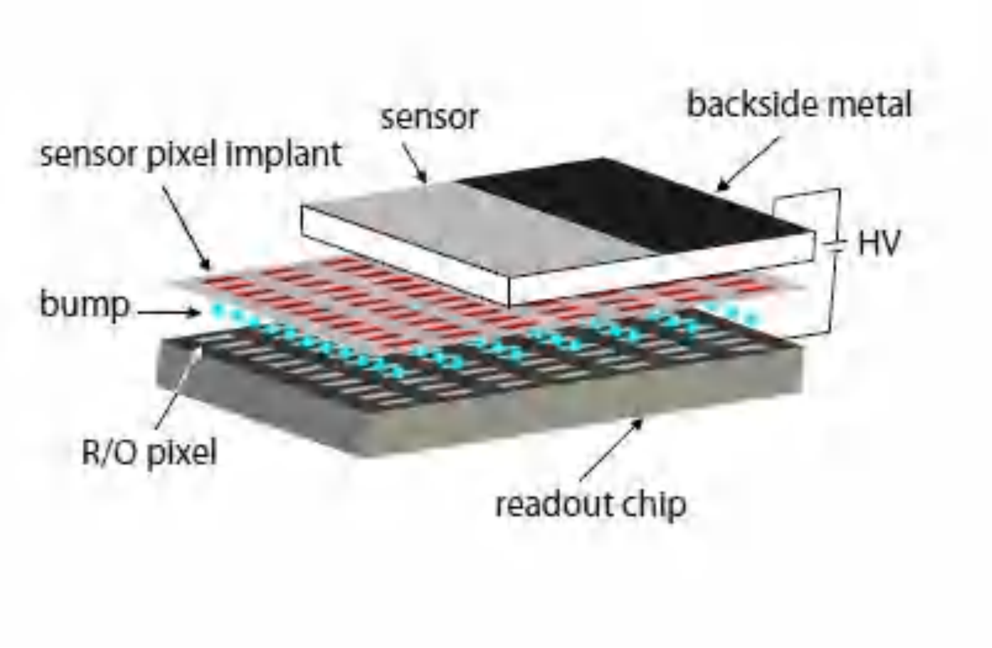

Figure I.19: Hybrid pixel matrix detector; the sensor and electronics chip have the same pixels size, bonded to each other by means of bump contacts.

I.7. Conclusion

In this chapter, we have presented a general state of the art on the topic of radiation detector, starting from a simple PN junction, moving to the main principle of detection when using the most known Silicon material for either photons, or charged particles. In addition, we have presented the types of damages caused by radiations and different approaches of 3D integrations that are recently used on radiation detectors technology.

In the next chapter, we will give a short introduction for the European X-ray Free Electron Laser-XFEL and Compact border termination detector, which we developed for such kind of applications.

I.8. References

[1] J. Kemmer, Fabrication of Low Noise Silicon Radiation Detectors by the Planar Process, Nuclear Instruments and Methods in Physics Research A, 169 (499–502), 1980.

[2] S.I. Parker et al., "3D - A proposed new architecture for solid state radiation detectors", Nuclear Instruments and Methods in Physics Research Section A, Vol. 395, Issue 3, 21 August 1997, pp. 328-343.

[3] S. Terzo et al., “Novel 3D Pixel Sensors for the Upgrade of the ATLAS Inner Tracker,” Front. Phys., vol. 9, p. 624668, Apr. 2021.

[4] DMS Sultan, Development of Small-Pitch, Thin 3D Sensors for Pixel Detector Upgrades at HL-LHC, PhD thesis, Trento university, Italy, June 2017.

[5] A. Boughedda, M. Lakhdara, S. Latreche, R. Mendicino, and G. F. Dalla Betta, “TCAD simulation of small-pitch 3D sensors for pixel detector upgrades at High Luminosity LHC,” *J. Phys.: Conf. Ser.*, vol. 1766, no. 1, p. 012014, Jan. 2021.

[6] A. H. Seidel, Handbook of Radiation Effect, Oxford University Press 2002.

[7] F. Hartmann, "Evolution of Silicon Sensor Technology in Particle Physics", Springer Tracts in Modern Physics, Springer-Verlag Berlin Heidelberg, , Vol 231, 2009

[8] H. Spieler, "Semiconductor Detector Systems", Oxford University Press 2005.

[9] C. Adolphsen, R. Jacobsen, V. Luth, G. Gratta, L. Labarga, A. Litke, A. Schwarz, M. Turala,C. Zaccardelli, A. Breakstone, C. J. Kenney, S. I. Parker, B. Barnett, P. Dauncey, D. Drewer, and J. Matthews, “The Mark II Silicon strip vertex detector,” Nuclear Instruments and Methods A, vol. 313, pp. 63–102, 1992.

[10] S. M. Sze, "Physics of Semiconductor Devices", New York Wiley, 1981, pp 90.

[11] M. Meschini, “Performance and upgrade plans for the CMS detector,” Nuclear Instruments and Methods in Physics Research Section A: Accelerators, Spectrometers, Detectors and Associated Equipment, vol. 718, pp. 1–6, Aug. 2013.

[12] Hartmann, F.: Evolution of Silicon Sensor Technology in Particle Physics. Springer, 2009 (cited on pages 16, 20, 24, 25, 26 and 47.)

[13] L. Rossi, et al., Pixel Detectors From Fundamentals to Applications, Springer, 2006.

[14] C.J. Kenney, et al., Silicon detectors with 3-D electrode arrays: fabrication and initial test results, IEEE Transaction of Neuclear Science, 1999, 46 (1224-1236).

[15] Zhang, Jiaguo, et al. "Investigation of X-ray induced radiation damage at the Si-SiO2 interface of silicon sensors for the European XFEL." Journal of Instrumentation 7.12 (2012): C12012.

[16] M. Moll, PhD thesis, "Radiation Damage in Silicon particle Detectors", 1999.

[17] R. Wunstorf et al., "Damage-induced surface effects in Silicon detectors", Nuclear Instruments and Methods In Physics Research A, Vol. 377, pp. 290-297, 1996.

[18] E. Fretwurst, Radiation damage in Silicon detectors, Nuclear Instruments and Methods in Physics Research A, 512(30-43), 2003.

[19] M. Huhtinen, Simulation of non-ionising energy loss and defect formation in Silicon, Nuclar Instruments and Methods in Physics Research A, 491(194-215) , 2002.

[20] ITRS Executive Summary 2005, Available online: http ://www.itrs.net/Links/2005ITRS/ExecSum2005.pdf

[21] K. W. Lee, A. Noriki, K. Kiyoyama, T. Fukushima, T. Tanaka, and M. Koyanagi, "Three-Dimensional Hybrid Integration Technology of CMOS, MEMS, and Photonics Circuits for Optoelectronic Heterogeneous Integrated Systems," IEEE Transactions on Electron Devices, vol. 58, pp. 748-757, 2011

[22] L. Madden, E. Wu, N. Kim, B. Banijamali, K. Abugharbieh, S. Ramalingam, et al., "Advancing high performance heterogeneous integration through die stacking," in 2012 Proceedings of the ESSCIRC (ESSCIRC, pp. 18-24), 2012.

Chapter 02

II. Chapter 02: Compact border termination detector for the Synchrotrons and X-Ray Free Electron Lasers application 33

II.1. Introduction

About two to three decades earlier, synchrotron science was almost exclusively the province of physicists and physical chemists. In contrast, modern-day synchrotron users come from all walks of scientific and academic life, from art history, paleontology, and cultural ethnology, to molecular biology, materials science, and high-tech industry etc...

To accommodate this growing demand, there are now several tens of synchrotrons around the world.

The Synchrotrons provide intense sources of electromagnetic radiation over large ranges of wavelengths, typically spanning values marginally shorter than that of visible light (i.e., beginning at approximately 100 nm in the so-called vacuum ultraviolet regime) to hard X-rays with wavelengths that are one to two orders of magnitude shorter than typical chemical bond lengths. This brilliant source of tunable radiation requires the development of new detectors based on the direct X-rays conversion inside semiconductors [1], [2], [3].

This chapter starts with a brief de a brief description of the European X-ray free electron laser-XFEL. The main goal in this part of the thesis is to discuss the results of our proposed new compact border termination for active-edge planar radiation detectors as compared a detector design carried out within the framework of the European PixFEL project.

II.2. The european X-ray Free Electron Laser-XFEL

The European X-Ray Free-Electron Laser Facility (European XFEL) is a research laser facility for X-rays. After producing the first laser, it was launched and inaugurated in 2017. Located in DESY Hamburg, this facility emits intense X-ray pulses much brighter than those produced by conventional Synchrotron light sources. It has a wavelength ranging from 0.05 to 4.7 nanometers; this feature leads to incredible resolution in the atoms size**. Figure II.1** provides the distribution of synchrotrons and the XFELS facilities around the world.

The XFELs with 3.4 km of length provides-rays pulses for the first time up to 27000 pulse.s^{-1}. They can be simultaneously distributed among three sources with a duration that can be less than 100 femtoseconds. This feature makes the European XFEL proclaim an advantage over its competitors [4].

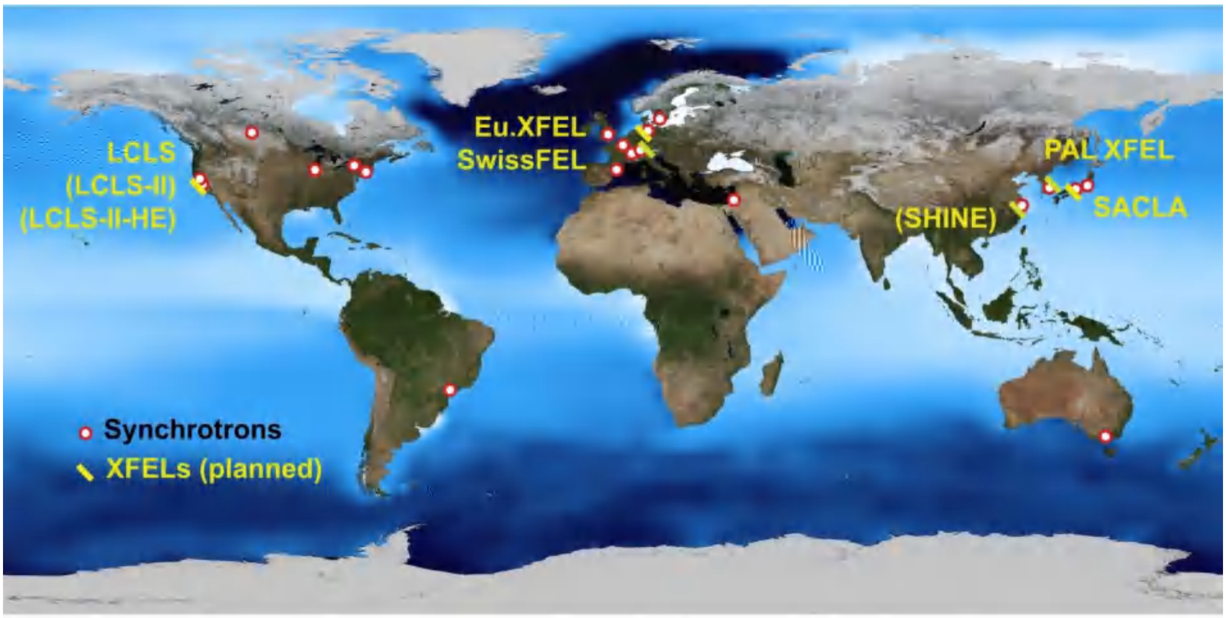

Figure II.1: The distribution of synchrotrons and XFELS facilities around the world [4].

The architecture of XFELs is also very different from that of synchrotrons. A short electron bunch is generated by irradiating a metallic target with a femtosecond laser pulse. These electrons are first accelerated within an accelerator of particles in a tunnel of 1.7 km long with an energy of 17.5 GeV [4], and then they enter a long array of alternating north-south, south-north magnet dipoles. This magnet array, called an "Undulator" and it is required to induce a phenomenon known as self-amplified spontaneous emission, or SASE as shown in Figure II.2 the result of SASE is that, after exiting the long Undulator magnet array, the electron bunch are altered in a way that it is now divided into many micro-bunches. Each bunch has a duration of only a few femtoseconds. These bunches produce the femtosecond x-radiation characteristic of XFELs.

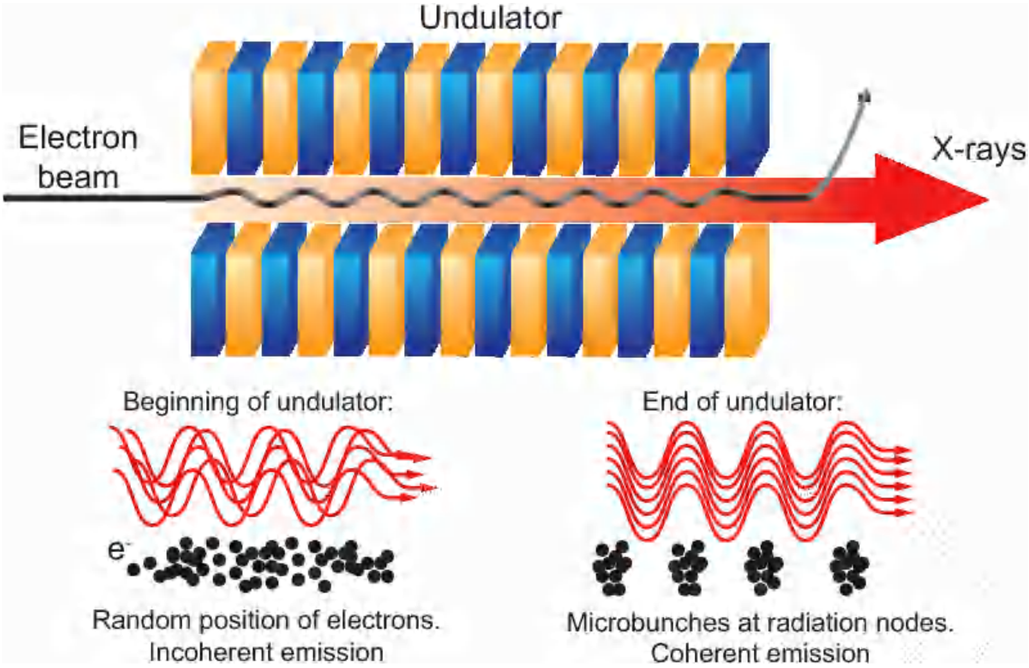

Figure II.2: The basic principle behind the generation of coherent x-rays in an XFEL source [05].

An electron beam passing through an undulator forces the electrons to move in a sinusoidal path and to emit X-ray photons. At first, in the beginning of the undulator, all electrons are randomly distributed and the emitted photons are out of phase with each other. However, as the electrons move along the undulator, they will be directed by the emitted X-ray electromagnetic field and begin to form micro-bunches at the nodal positions of the electromagnetic wave. At the end of the undulator, all electrons are emitting in-phase and the resulting X-rays are coherent.

By birth of XFEL project, there was no detector able to fill the need of this new generation of extremely powerful radiation sources with extraordinary performance specifications: in three years of operation doses of up to 1GGy, up to 10^5 12 keV photons per pixel of 200 µm × 200 µm which arrives within less than 100 fs with a time interval between XFEL pulses of 220 ns. **Figure II.3** and **Figure II.4** present a summary of the European XFEL bunch time pattern and the XFEL challenges for the Silicon detectors. Three main projects were launched after that by the European XFEL to fulfill the following requirements [6]: Adaptive Gain Integrated Pixel Detector (AGIPD), the Large Pixel Detector (LPD), and the DEPFET with signal compression (DSSC). Some other projects were followed in recent years, among which, we can mention the pnCCD detector [7], the FCCD detector [8] and the **PixFEL detector** [9].

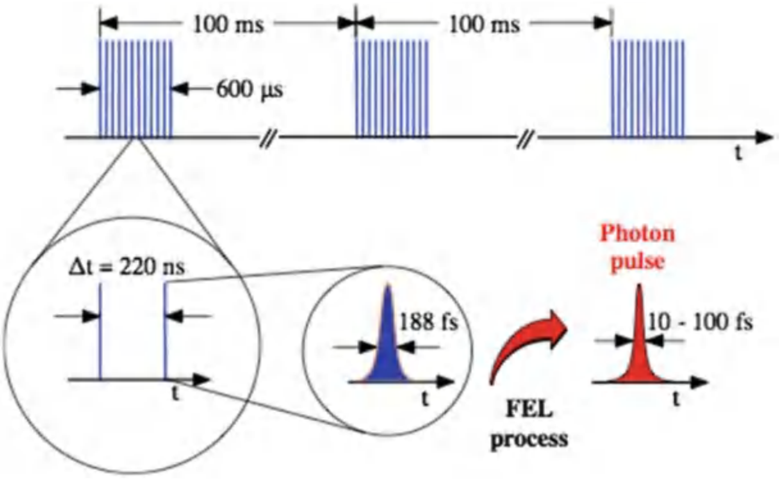

Figure II.3 European XFEL bunch time pattern

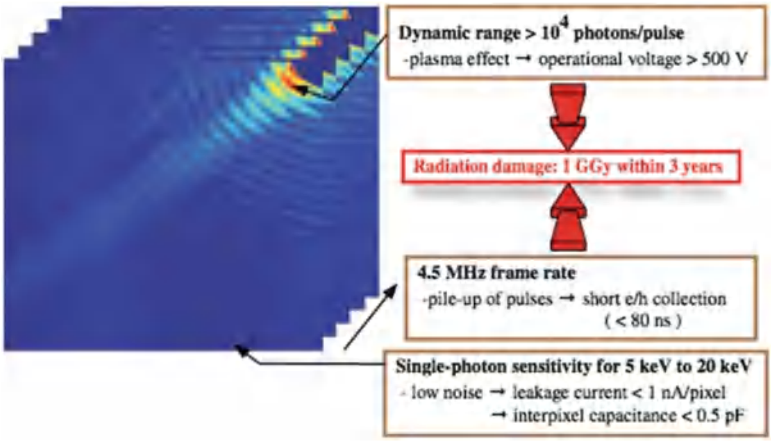

Figure II.4: Challenges of silicon Detectors used at the European XFEL [10].

II.3. The PixFEL Detectors

Recently, there has been renewed interest in free-electron laser (FEL) applications. There has been substantial research undertaken on the role of developing advanced X-ray imaging instrumentation for applications at the FEL facilities. Several attempts have been made to fabricate pixelated edgeless sensors precisely the planar sensors to be used in this field among them **PixFEL project**. This project was funded by the **Italian Nuclear Research Institute (INFN)** in collaboration with various universities: **Trento, Bergamo, Pisa, Pavia and Constantine University** [11]**.** The main goal was the development and the realization of a two-dimensional pixelated-imaging camera to cope with the challenging requirements of its experiments [12]. The overall structure of the sensor consists mainly of a detector part connected to an ASIC electronic part as shown in **Figure II.5.**

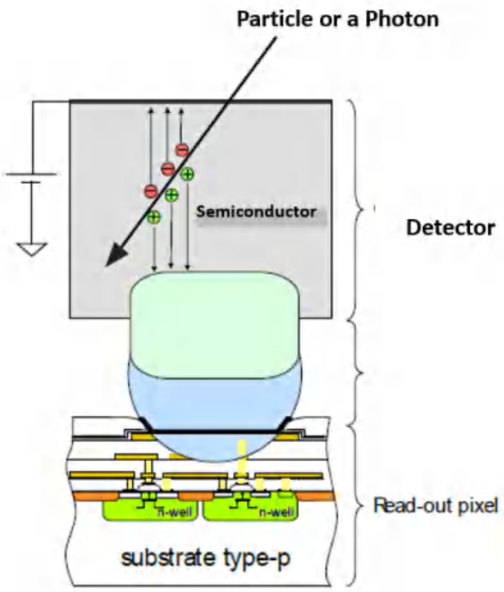

Figure II.5: Schematic view of the overall structure of the radiation detector[13].

The camera is based on hybrid multilayer tiles made of active-edge high resistivity pixel sensors. The later bump-bonded to two 65-nm CMOS front-end ICs. Vertical 3D integration technologies (TSV) are considered for connecting the ICs, resulting in four-side buttable readout chips with a small pixel pitch and all of the necessary functionalities on board.
A conceptual sketch of the PixFEL matrix of the 4- side buttable tiles is presented in **Figure II.6**

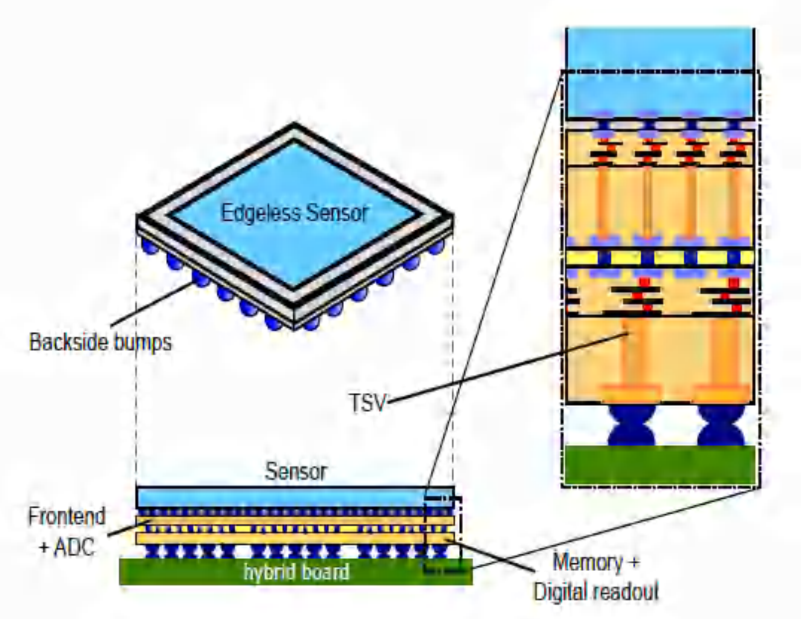

Figure II.6: Overview of a 4-side buttable module composed of a multilayer device [13].

II.3.1. Active edge sensors

The active edges are trenches etched and doped at the periphery of a silicon radiation detector by deep reactive ion etching machine (DRIE) to act as a wall to terminate the active area. It was first developed at the Stanford Nanofabrication Facility (SNF) as an additional features of 3D technology [14]. Later, they have been applied to planar detectors [15]. Trenched electrodes have been utilized at **FBK** for active edge [16] and slim edge terminations [09]. Nowadays they are used at the pixel level as 3D trenched electrode sensors [17], [18]. Such technology is used in order to enable the development of large area tiled silicon pixel detectors with small dead area between modules by utilizing edgeless sensors, this improves the geometrical inefficiencies of different applications in high energy physics, X ray experiments at synchrotrons and Free Electron Lasers (FELs), and medical imaging. This is evident in the case new pixel sensors for the High Luminosity LHC (HL-LHC) upgrade of the ATLAS pixel tracker, the area insensitive must be significantly reduced in order to avoid the overlapping adjacent modules with a maximum of geometrical acceptance [19]. Furthermore, full signal sensitivity up to a few micrometers from the physical edge can be obtained [15]. These advantages come with some increase in the fabrication process complexity due to the DRIE step and the need of a support wafer to hold different sensors together once the trenches have been etched and it must be removed at the end of the process.

Recently, some other processing facilities in Europe, such as SINTEF (Norway) [20], VTT (Finland) [21], and a technological partner in the PixFEL project FBK [22], [23] have developed the active-edge technologies.

Figure II.*7* shows a schematic cross-section of a planar active sensor. The considered PixFEL sensors are p-on-n. The choice of such structure was dictated by the requirements of radiation tolerance. The reverse bias voltage makes the electric field oriented from Si / SiO2 interface to the SiO2 surface, thus, minimizing the concentration of positive oxide charges induced by radiation which are expected to reach a value of $3x10^{12}$ cm^{-2} at high X-ray doses [12]. In contrast to pixel sensors for High Energy Physics applications, which require thin substrates, the FEL applications imply the use of thick sensors in order to achieve a high detection efficiency (~90%) for x-ray energies that exceed 10 KeV. To this end, a detector with a thickness of 450 µm would allow reaching an efficiency up to ~87% at 12 KeV as it is shown in **Figure II.8**.

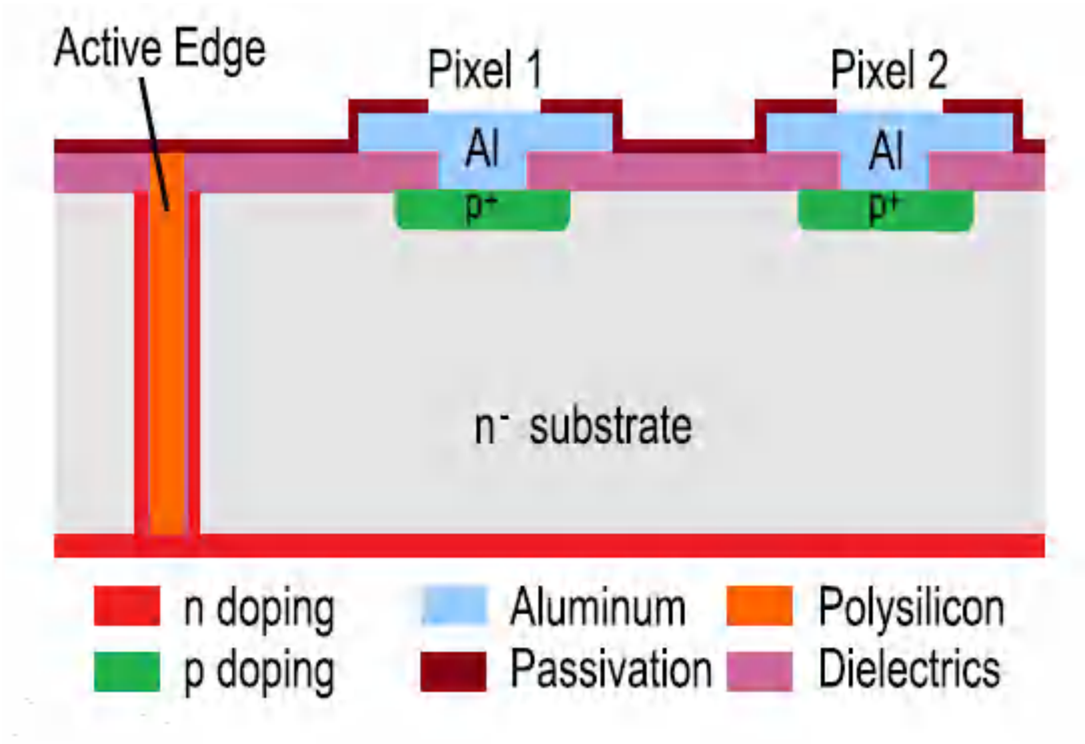

Figure II.7: A schematic cross section of the detector structure based on Active edge technology [22].

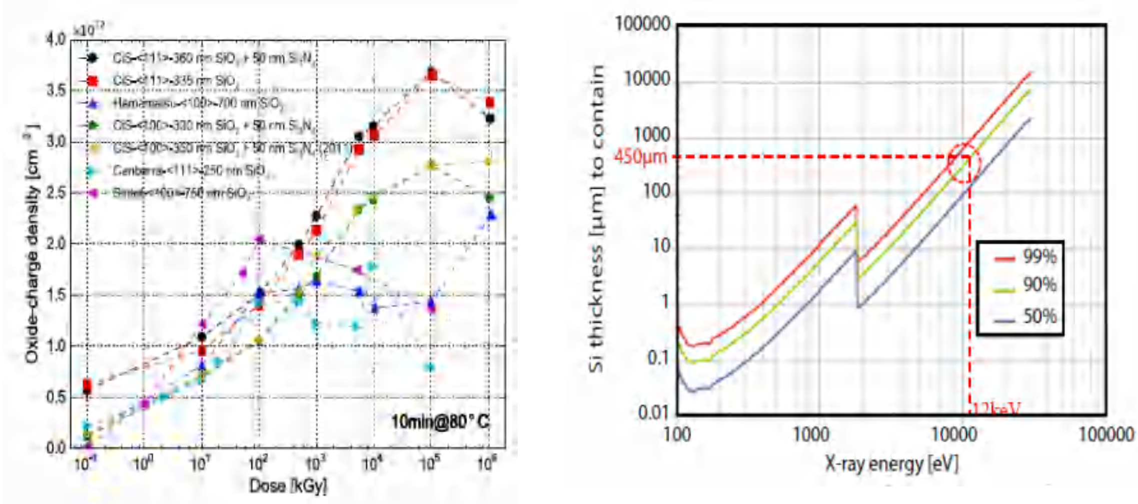

(a) (b)

Figure II.8: a) Oxide charges density as a function of the X-radiation dose obtained from different text structures. b) Analytical estimation of the active thickness of the sensor as a function of the energy of an X-ray [13]

One of the most important issues to consider in FEL applications is the so-called plasma effects. This is due to the large hitting number of photons per pixel at the same time (10^4 photons per pixel). Thus, a large number of carrier's densities will be generated. This could lead to a deterioration in the electrical performance of the sensor, unless a high voltage is applied to mitigate these effects. The recommended value in [24] is **500 V.**

It has been confirmed that the use of guard rings with an external field plate structure in the dead area allows a uniform electric field distribution around the active area of the sensor and can lead to high breakdown voltage, as well as reducing the leakage current [19]. On one hand, it is possible to achieve such values by using multiple guard rings termination, however, a wide dead area is required at the edge (more than 1 mm) [25]. On the other hand, the use of the active edge can minimize the dead area but with the expense of a very high electric field, this could lead to an early breakdown voltage.

The termination of the PixFEL detector reported in [9] is based on four floating guard rings with a standard field plate arranged in a total size of 150 µm. This detector can withstand approximately 400 V reverse biased in all operating conditions. It was optimized and designed by means of Technology Computer-Aided Design (TCAD) simulations. The findings were in very good agreement with experiment data from the prototype fabricated at Fondazione Bruno Kessler (FBK (Trento, Italy)). In this part of the thesis, we present a design variant using TCAD simulations that reduces the dead area and increases the breakdown voltage with a small increase in fabrication complexity. The results represent a further step towards developing such kinds of sensors. The following part describes the PixFEL structure and the simulations results.

II.3.2. Description of the PixFEL structure and its simulations results

The considered structure is a p-on-n sensor. It presents a single electrode made on a high-resistivity (n^-) substrate ($2e10^{11}cm^{-3}$), which has a crystal orientation <100> and a thickness of 450 µm. n^+ Ohmic contact regions at the backside and along the trench at the edge with 5µm wide. The device termination has four floating guard rings with standard field plates (5 µm wide) having a total size of 150 µm. **Figure II.9** provides a schematic of the considered structure.

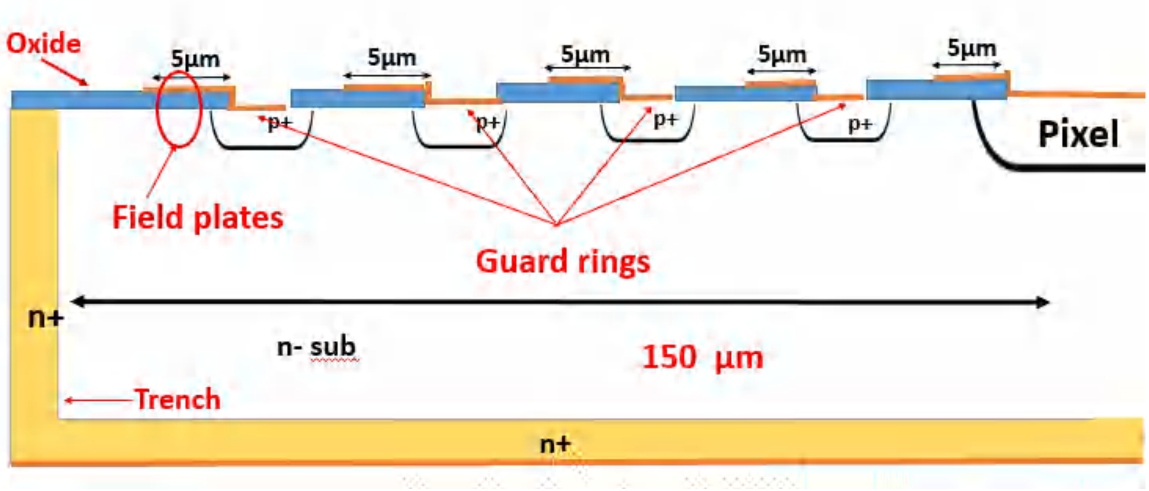

Figure II.9: The structure of planar detector (one pixel and four guard rings)

According to published works [9], [26], the new four guard-rings structure permits to improve the breakdown voltage when high oxide charges are taken into consideration. In order to investigate the effects of high fluencies on the p-on-n sensor, the breakdown voltage is evaluated according to the depth of the junction (X_j) using a different oxide charge density (**Figure II.10**). The most significant result which emerges from the data is that the breakdown voltage reaches values up to 427 V for Xj = 2.4 µm and an oxide thickness of about 300 nm under 3 × 10^{12} cm^{-2} of oxide charge. These results are very similar to those reported and confirmed by an experiment in [9].

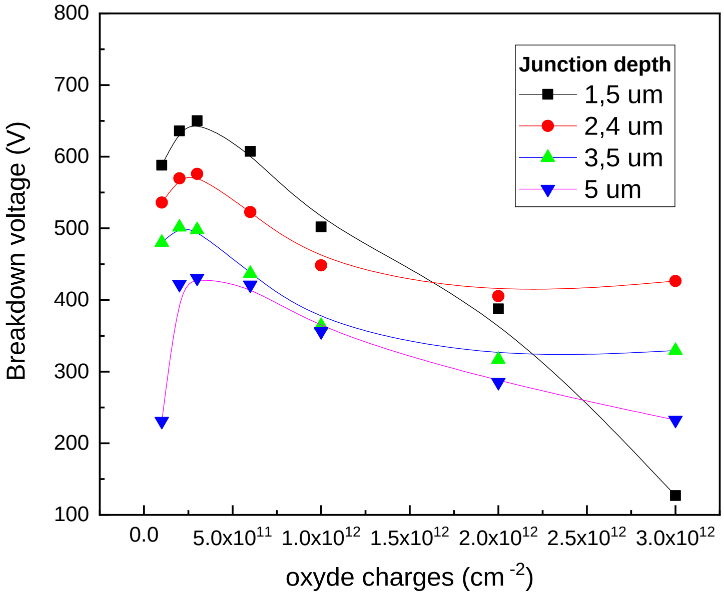

Figure II.10: The breakdown voltage versus the oxide charges and parameterized by the junction depth.

II.3.3. The limits of the PixFel structure

As we mentioned before, the FEL applications heightened the need for silicon pixel sensors, which can withstand high X-ray doses up to 1GGy with a minimum of dead area. The PixFEL sensors were optimized taking into account the most relevant geometry and process parameters, allowing 4GR structure terminations with 150-µm size to withstand up to 400 V in all operation conditions. However, the fabrication and the electrical characterization of devices are well done and demonstrated to be functional, a slightly smaller breakdown voltage was found compared to the one predicted in simulation [9].

Further investigations were required to shed the light on structure geometry. No previous studies have investigated the exact position in where the breakdown occurs. Figure II.10 illustrates that the electric field is highest at the end of the first field plate.

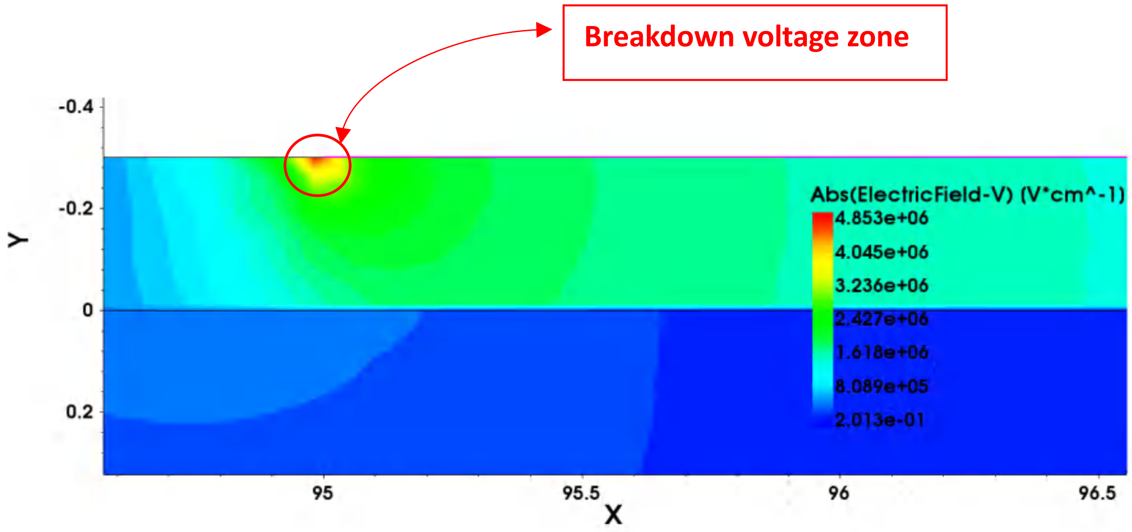

Figure II.11: The Electric field distribution of the structure with the new modification with the standard Guard ring.

Using different widths of field plates were not a very useful solution; however, trying a new design of it may lead to good results. **Figure II.12** shows the Electric field distribution of a new proposed structure. More details will be done on the following parts of this chapter.

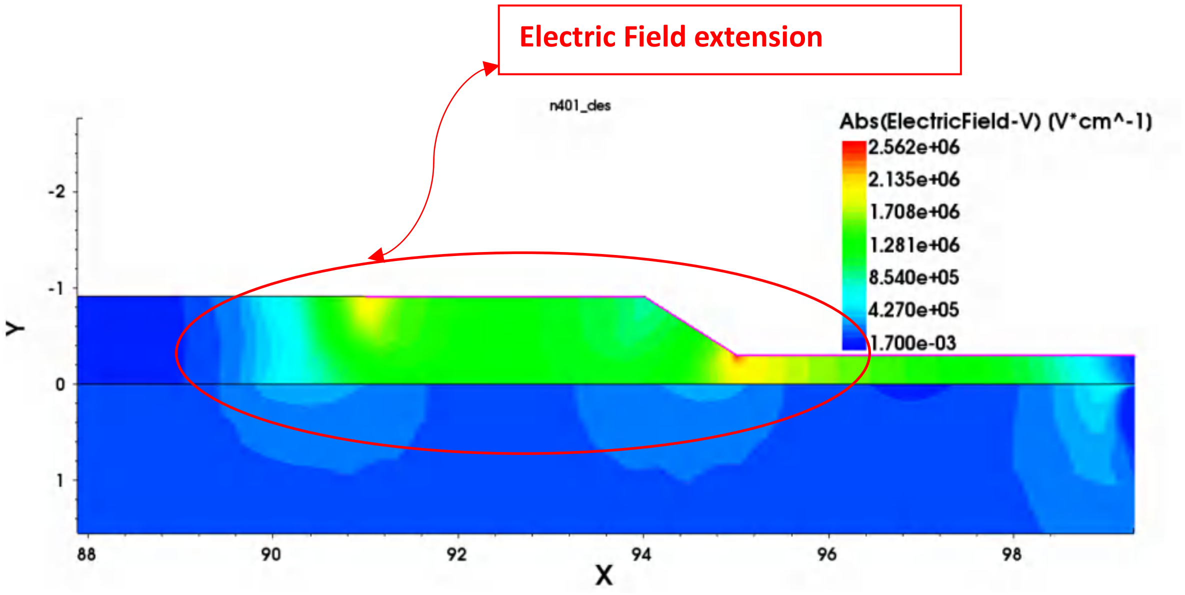

Figure II.12: The Electric field distribution of the structure with the new modification

II.4. The description of the news proposed structure

New field plate designs are proposed in this part aiming to obtain higher breakdown voltage. Firstly, we introduce these concepts to a simple structure with only the main detector junction separated from the active edge with a distance of 100µm.

Figure II.13 sketches the cross-section of the new field-plates designs in comparison with the existing one. Figure II.13a provides the structure cross-section of the standard field plate with the optimal oxide thickness, that was found and proved experimentally in our previous work [9]. Figure II.13b provides a design variant features a field-plate that we proposed in shape conformal to a sloped side-wall oxide layer, starting from the same 300-nm thickness and ending at 910 nm (Tox2) [27]. Grey-tone lithography [28] could be used to obtain the oxide thickness modulation required to fabricate this structure. In the field of power transistors, this so-called ‘slant field plate’ and has been proved to be reliable [29]. As far as we know, it has not been applied yet to the radiation sensors field. Its effect is similar to multi-step field plates but with a smaller area occupation, providing a smoother electric field distribution at the junction's edge.

Alternatively, Figure 2.13c displays a slant field plate achieved in a typical CMOS local oxidation of silicon (LOCOS) method [30] by depositing the metal on top of the bird's beak area while keeping the overall oxide thickness the same.

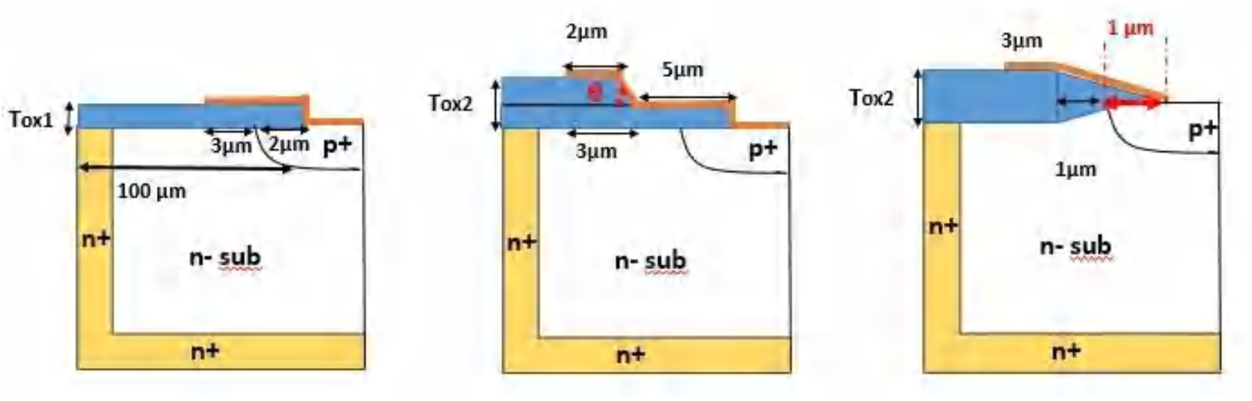

(a) (b) (c)

Figure II.13: Schematic cross sections of different field-plate structures applied to main detector junction with active edge (not to scale). a Existing device with uniform, 300-nm thick oxide layer [9] b,c Proposed variants with sloped side-wall oxide layer

II.5. Results

II.5.1. Benchmark of the two proposed border termination and the standard one

In order to compare the impact of different field plate designs, TCAD simulations incorporating FBK technology have been performed. As a starting material, a silicon substrate with a high resistivity doping of 2 x 10^{11} cm^{-3} and 450 µm were considered. The p^+n^- junction depth value is 2.4 µm, the considered value is the optimal one obtained in [9], which was also confirmed to be the best choice for the slant field plate. At the Si/SiO2 interface, different densities of positive oxide charge, corresponding to different X-ray doses, are added into account for surface radiation damage. There are two main reasons why we did not use more advanced models like [31], [32] , which also take into account the interface traps : (i) up to this time, no model has been validated experimentally for edge breakdown at high X-ray doses of interest for FEL applications; (ii) The positive oxide charge will be partially compensated by the interface traps. This effect will lead to larger simulated breakdown voltage values than those obtained only in the presence of oxide charge. From this perspective, in our simulations, we used the model that represents the worst-case scenario to predict the breakdown voltage.

In Figure II.14, the simulated breakdown voltage (V_{bd}) is plotted as a function of the oxide charge density (N_{ox}), up to 3 x10^{12} cm^{-2}, which is the worst-case for the extremely high ionizing radiation in FEL applications [14].

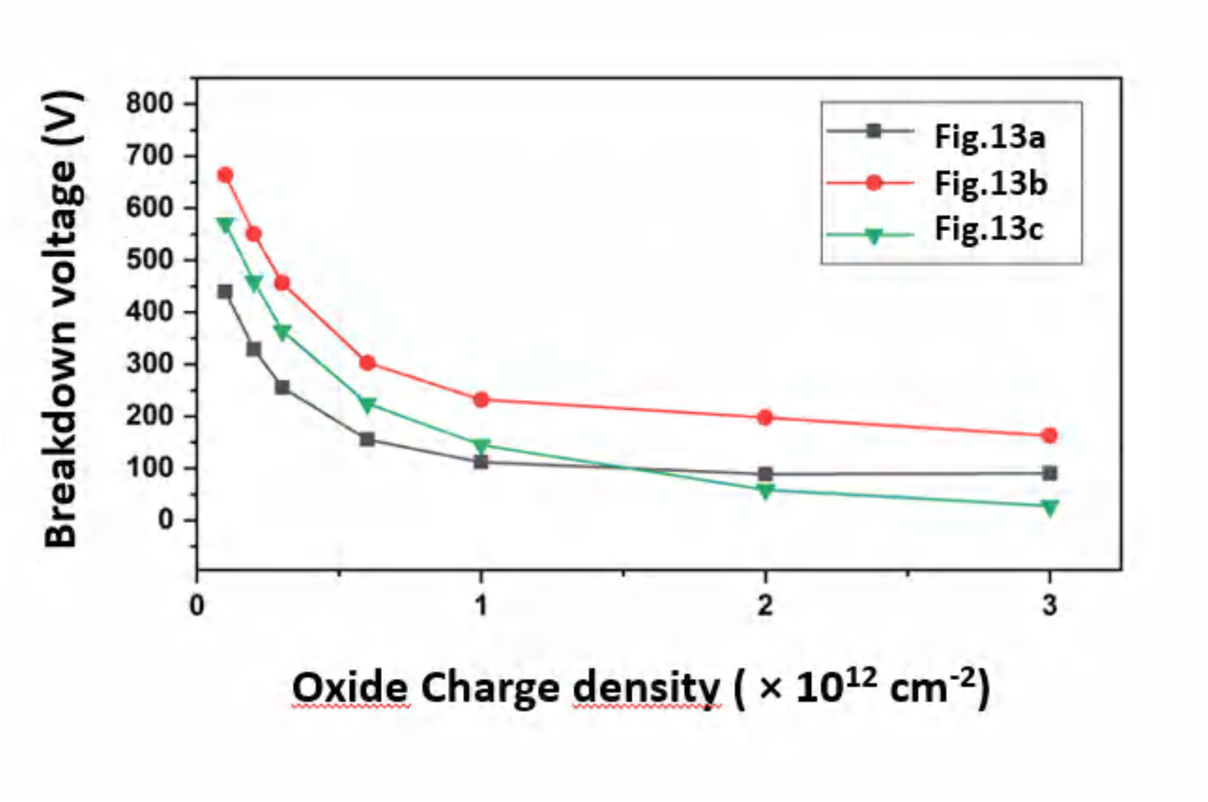

Figure II.14: Simulated breakdown voltage as a function of the oxide charge density for the three structures of Figure II.13.

Looking at this figure, it is obvious that the slant field plate presented in Figure II.13b has larger breakdown voltages compared to the standard one at all Nox values, while the results of Figure 2.13c are advantageous for only small N_{ox} values.

The improved breakdown performance of the slant field plate structure can be explained with the aid of Figure II.15. it compares the 1D distributions of the electric field along X at 0.1 µm depth in silicon for the structures of Figure II.13a and Figure II.13b at the maximum Nox at 80 V bias. The slant field plate lowers the electric field peaks, both at the junction and more markedly in the outward region, the latter absorbing most of the electric field increase at 110 V.

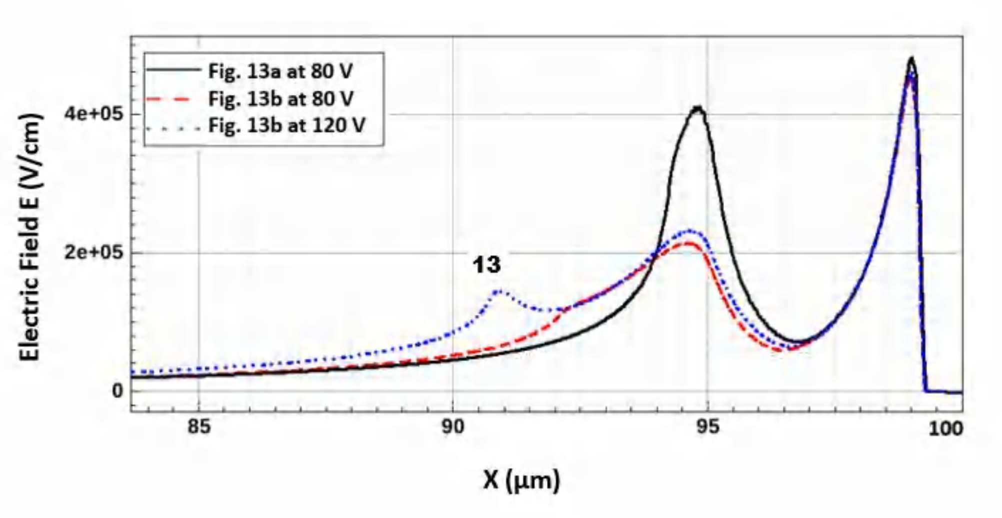

Figure II.15: Simulated 1-D distributions of the electric field along X at 0.1µm depth in silicon for the structures of Figs. 1a (80 V bias) and 1b (80 V and 110 V bias) at the maximum oxide charge density of 3×10^{12} cm^{-2}.

II.5.2. The optimal angle and the best size for the border termination with slant field plate

The slant field plate angle that corresponds to the optimal value in order to obtain maximum breakdown voltage at N_{ox}=3×10^{12} cm^{-2} is θ~30° as provided in Figure II.16, which is used in the simulation of in Figure II.14 and Figure II.15.

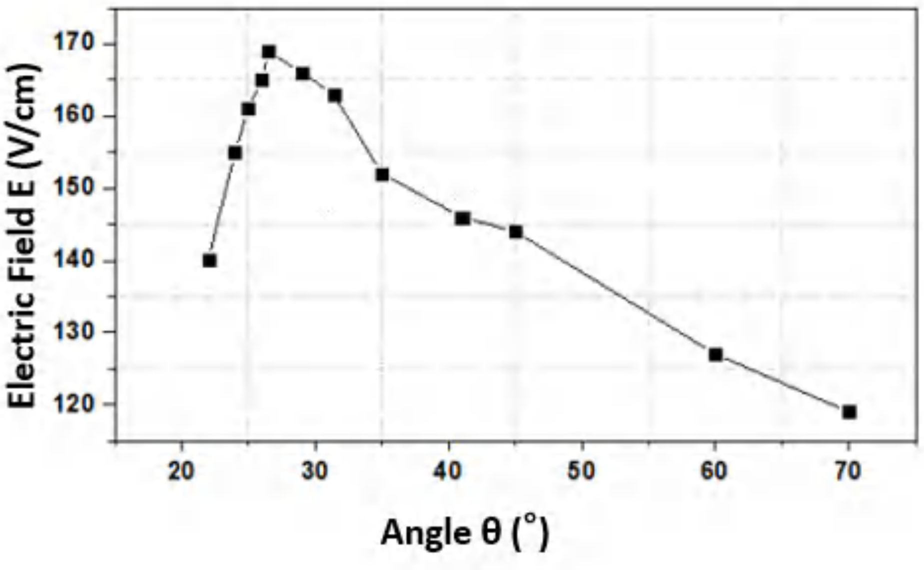

Figure II.16: Simulated breakdown voltage as a function of the slant field-plate angle θ at an oxide charge density of 3×10^{12} cm^{-2} for the structure of Figure 2.13b.

Based upon these observations, various border terminations using various number of guard rings ranging from 1 to 4, all equipped with slant field plate has been designed and applied to the main detector junction. The substrate thickness, junction depth, and doping concentration were all the same as in previous simulations. 150 µm is the overall size of the edge region, which is the same one considered in [9]. Figure II.17 shows the simulation domain for the structure with four guard rings, with details of the relevant geometries.

Of course, reducing the number of floating rings allows for a decrease in the overall size of the edge region. As in [9], the guard ring implants are 15-µm wide (+ 2 µm of lateral diffusion) and the spacing between them were defined to maximize the breakdown voltage at the largest oxide charge concentration (note that, depending on the number of guard rings, this choice might slightly reduce the breakdown voltage at very low N_{ox}).

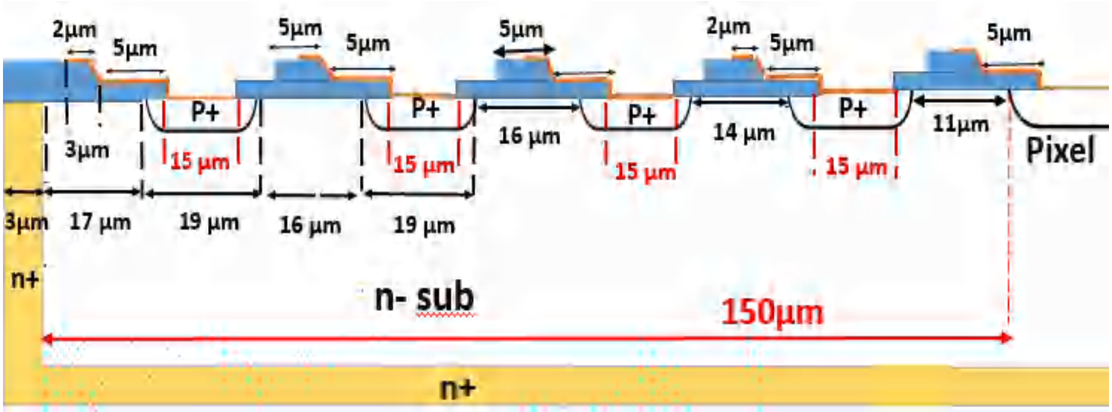

Figure II.17: Simulation domain for border termination with four floating guard rings equipped with the field-plate of Fig. 1b (not to scale).

The breakdown voltage simulation of multi-guard-rings terminations is illustrated in Figure II.18 as a function of oxide charge density; it is compared also with the existing termination with four guard rings as in [9].

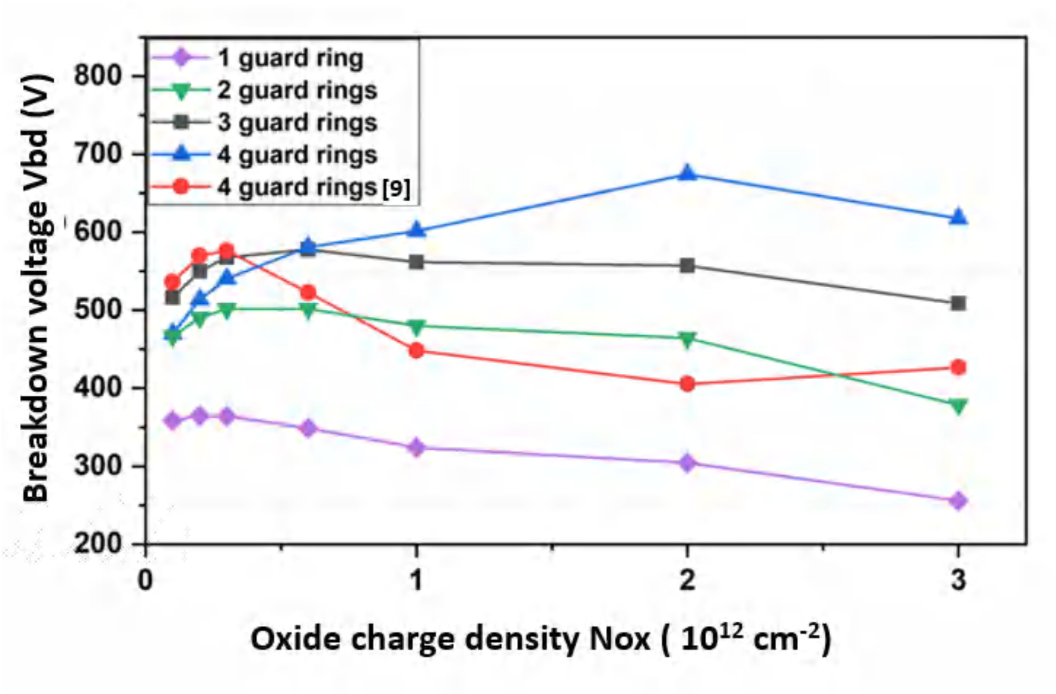

Figure II.18: Simulated breakdown voltage as a function of the oxide charge density for different multi-guard-ring border terminations.

Apart from the one guard ring case, where a relatively low-breakdown voltage is yielded in all N_{ox} conditions with a minimum value of ~250 V at 3×10^{12} cm^{-2} (for the considered substrate thickness, this value is not high enough for the considered FEL applications [9]); all the proposed slant field plates structures show extremely high-breakdown voltages at all Nox values. Under all conditions, the four guard rings structures yield to a value of $V_{bd} > 470$ V, with greatly increased values at high N_{ox} exceeding 600V. What is notable about the structure with two guard rings is that an edge with only ~90 µm size yields a minimum V_{bd} of ~380 V at N_{ox} of 3×10^{12} cm^{-2}, which is almost identical to the existing structure [9]. Since the structure with only three guard rings is less sensitive to the oxide charge variation, it seems to offer the best overall trade-off, with a breakdown voltage value >500 V under all conditions.

The simulated minimum breakdown voltages and the edge region sizes for all the considered border terminations are summarized in Table II-1 in comparison with the existing structure with four guard rings. The advantages provided by the slant field-plate are obvious.

Table II-1: Summary of the main characteristics of different multi-guard-ring border terminations based on slant field plates also in comparison to the 4 guard-ring termination with standard field plate of [5].

Termination design	Size of edge region (µm)	Minimum Breakdown Voltage (V)
1 guard ring	**52**	**256**
2 guard rings	**87**	**379**
3 guard rings	**117**	**509**
4 guard rings	**150**	**470**
4 guard rings [9]	**150**	**406**

II.6. Conclusion

In this chapter, we have achieved an analysis and a conception of the detectors carried out within the framework of the European PixFEL project. We presented first, an overview of the PixFEL detector. Subsequently, we have presented a new compact border termination as compared to an existing design with four guard rings; owing to the use of slant field plates, the proposed design with two guard rings yields almost the same minimum breakdown voltage with an overall size smaller by ~60 µm. Whereas, with three guard rings we obtained both a ~100 V increase of the minimum breakdown voltage and an overall size decrease by ~30 µm. These characteristics make the proposed terminations appealing for X-ray imaging applications at FEL facilities, with a minor increase in the fabrication process complexity coming from the use of Greystone lithography to tailor the slope of the side-wall oxide layer in the field plate regions. We plan to experimentally validate this approach in a batch of test diodes at FBK in next year.

II.7. References

[01] Emma, Paul, et al. "First lasing and operation of an ångstrom-wavelength free-electron laser." *nature photonics* 4.9 (2010): 641-647.

[02] Ishikawa, Tetsuya, et al. "A compact X-ray free-electron laser emitting in the sub-ångström region." *nature photonics* 6.8 (2012): 540-544.

[03] Abela, R., et al. *XFEL: the European X-ray free-electron laser-technical design report*. No. DESY-06-097. DESY, 2006.

[04] https ://www.xfel.eu/

[05] Nilsson, Daniel. *Zone Plates for Hard X-Ray Free-Electron Lasers*. Diss. KTH Royal Institute of Technology, 2013.

[06] Hatsui, Takaki, and Heinz Graafsma. "X-ray imaging detectors for synchrotron and XFEL sources." *IUCrJ* 2.3 (2015): 371-383.

[07] Strüder, Lothar, et al. "Large-format, high-speed, X-ray pnCCDs combined with electron and ion imaging spectrometers in a multipurpose chamber for experiments at 4th generation light sources." *Nuclear Instruments and Methods in Physics Research Section A: Accelerators, Spectrometers, Detectors and Associated Equipment* 614.3 (2010): 483-496.

[08] Denes, P., et al. "A fast, direct x-ray detection charge-coupled device." *Review of Scientific Instruments* 80.8 (2009): 083302.

[09] Benkechkache, M. A., et al. "Design and first characterization of active and slim-edge planar detectors for FEL applications." *IEEE Transactions on Nuclear Science* 64.4 (2017): 1062-1070.

[10] Seibert, M. Marvin, et al. "Single mimivirus particles intercepted and imaged with an X-ray laser." *Nature* 470.7332 (2011): 78-81.

[11] Rizzo, Giuliana, et al. "The PixFEL project: development of advanced X-ray pixel detectors for application at future FEL facilities." *Journal of Instrumentation* 10.02 (2015): C02024.

[12] Zhang, Jiaguo, et al. "Investigation of X-ray induced radiation damage at the Si-SiO2 interface of silicon sensors for the European XFEL." *Journal of Instrumentation* 7.12 (2012): C12012.

[13] Benkechkache Mohamed El Amine PhD thesis in *Impact des TSVs (Through Silicon Vias) sur les circuits CMOS nanom´ etriques–Etude et conception d'un détecteur d'un d´etecteur verticalement intégré de rayon X.* Diss, université des frères mentouri constantine 1,2018.

[14] Kenney, Christopher J., Sherwood Parker, and Edith Walckiers. "Results from 3-D silicon sensors with wall electrodes: near-cell-edge sensitivity measurements as a preview of active-edge sensors." *IEEE Transactions on Nuclear Science* 48.6 (2001): 2405-2410.

[15] Kenney, C. J., et al. "Active-edge planar radiation sensors." *Nuclear Instruments and Methods in Physics Research Section A: Accelerators, Spectrometers, Detectors and Associated Equipment* 565.1 (2006): 272-277.

[16] Povoli, Marco, et al. "Development of planar detectors with active edge." *Nuclear Instruments and Methods in Physics Research Section A: Accelerators, Spectrometers, Detectors and Associated Equipment* 658.1 (2011): 103-107.

[17] Mendicino, Roberto, et al. "3D trenched-electrode sensors for charged particle tracking and timing." *Nuclear Instruments and Methods in Physics Research Section A: Accelerators, Spectrometers, Detectors and Associated Equipment* 927 (2019): 24-30.

[18] Forcolin, G. T., et al. "3D trenched-electrode pixel sensors: Design, technology and initial results." *Nuclear Instruments and Methods in Physics Research Section A: Accelerators, Spectrometers, Detectors and Associated Equipment* 981 (2020): 164437.

[19] Koybasi, Ozhan, et al. "Edgeless silicon sensors fabricated without support wafer." *Nuclear Instruments and Methods in Physics Research Section A: Accelerators, Spectrometers, Detectors and Associated Equipment* 953 (2020): 163176.

[20] Kalliopuska, Juha, et al. "Processing and characterization of edgeless radiation detectors for large area detection." *Nuclear Instruments and Methods in Physics Research Section A: Accelerators, Spectrometers, Detectors and Associated Equipment* 731 (2013): 205-209.

[21] Povoli, Marco, et al. "Development of planar detectors with active edge." *Nuclear Instruments and Methods in Physics Research Section A: Accelerators, Spectrometers, Detectors and Associated Equipment* 658.1 (2011): 103-107.

[22] Dalla Betta, Gian-Franco, et al. "Edgeless and slim-edge solutions for silicon pixel sensors." *PoS (Vertex2013)* 42 (2013).

[23] Dalla Betta, Gian-Franco, et al. "Design and TCAD simulations of planar active-edge pixel sensors for future XFEL applications." *2014 IEEE Nuclear Science Symposium and Medical Imaging Conference (NSS/MIC)*. IEEE, 2014.

[24] Becker, Julian, et al. "Impact of plasma effects on the performance of silicon sensors at an X-ray FEL." *Nuclear Instruments and Methods in Physics Research Section A: Accelerators, Spectrometers, Detectors and Associated Equipment* 615.2 (2010): 230-236.

[25] Schwandt, Joern, et al. "Design and first tests of a radiation-hard pixel sensor for the European X-ray Free-Electron Laser." *14th European Conference on Radiation and Its Effects on Components and Systems (RADECS)*. IEEE, (2013) 1-8.

[26] Rizzo, Giuliana, et al. "The PixFEL project: development of advanced X-ray pixel detectors for application at future FEL facilities." *Journal of Instrumentation* 10.02 (2015): C02024.

[27] Boughedda, Abderrezak, et al. "Compact border termination for active-edge planar radiation detectors with enhanced breakdown voltage." *Micro & Nano Letters* 15.13 (2020): 969-971.

[28] Henke, Wolfgang, et al. "Simulation and process design of gray-tone lithography for the fabrication of arbitrarily shaped surfaces." *Japanese journal of applied physics* 33.12S (1994): 6809.

[29] Dora, Y., et al. "High breakdown voltage achieved on AlGaN/GaN HEMTs with integrated slant field plates." *IEEE Electron Device Letters* 27.9 (2006): 713-715.

[30] Franssila, Sami. *Introduction to microfabrication*. John Wiley & Sons, 2010.

[31] Zhang, Jiaguo, et al. "Study of radiation damage induced by 12 keV X-rays in MOS structures built on high-resistivity n-type silicon." *Journal of Synchrotron Radiation* 19.3 (2012): 340-346.

[32] Moscatelli, F., et al. "Surface damage characterization of FBK devices for High Luminosity LHC (HL-LHC) operations." *Journal of Instrumentation* 12.12 (2017): P12010.

Chapter 03

III.1. Introduction

The big bang is the beginning of the universe according to many philosophies throughout history, and much research and scientific theories were conducted over the last 100 years. In the Holly Quran, Allah Almighty says; << **Do those who disbelieve ever consider that the heavens and the earth were at first one piece, and then We parted them as separate entities; and that We have made every living thing from water? Will they still not come to believe?** >> This means that the heavens and earth were one piece and the God separated them. Today scientists try to understand what happened immediately after the separation and how the universe was formed in order to know what the mean component of everything in life is. At first, there was something called singularity, which we do not know too much about it, and if there was something before it or not, was there time and space? What we know about it is that: it was the starting point, and that is where the big bang happened. In one trillionth of second after the Big Bang, the size of the universe expanded trillions times, the well known Quark was created, which is the small particle form of the matter. Another particle was formed called Higgs Boson, this particle gives the other particles their masses. Then, the universe started cooling down, and the Quarks particles started to cluster and form protons and neutrinos. The Particles physics emerged to study the tiniest particle of matter and trying to understand how the Quantum mechanics works, in order to understand how the world functions. For this purpose, scientist needs three things; a particle collider, a data centers with a powerful analyzing abilities and particle accelerators to make this particles reach a velocity close to the speed of lights in order to simulate the same big bang conditions. Therefore, CERN built a powerful equipment to reveal these particles and to give the opportunity to experimentally investigate the theories relevant to Higgs, Dark Matter and extra dimension.

This is chapter is composed of two complementary parts. The first one deals with high physics at the LHC, the second one will be devoted to 3D radiation detectors. More precisely the Small-pitch 3D pixel sensors, which are the best candidates for the innermost tracking layers of the major detector upgrades at the High Luminosity LHC (HL-LHC). Some experimental results obtained from our FBK group will be also summarized.

III.2. High energy physics at LHC:

The Large Hadron Collider (LHC) is the world's leading center in High Energy Physics (HEP). Its study concentrated on decoding the structure and the matter in the universe, from the tiniest particles to the building blocks of life. The European Organization for Nuclear Research built the well-known as CERN (**Conseil Européen pour la Recherche Nucléaire**) between 1998 and 2008. The main goal was finding the Higgs boson and other particles predicted by supersymmetric.

The accelerator are made up of two rings superconducting collider located inside an underground tunnel of 27 kilometer-long and 3.8-meter-wide that evolved from the Large Electron-Positron Collider (LEP) [1],[2]. The machine is constructed at a depth confined between 50 and 175 meters beneath the French Swiss border near Geneva, Switzerland.

The LHC aims to reveal the physics beyond the Standard Model with first operating mode of proton-proton collision. It delivers unprecedented luminosity (10^{34} cm^{-2}s^{-1}) and center of mass collision energies of up to 14 TeV. The LHC's second operating mode allows it to collide lead ions (Pb-Pb) with a center-of-mass energy of 1150 TeV.

For a given process, the total number of events per second produced by beam collision can be computed as follows:

$$N_{event} = L\sigma_{event} \qquad \textbf{\textit{III-1}}$$

Where σ represents the cross-section for the event under study and L is its luminosity, which must be very high while seeking for extremely uncommon events, such as the Higgs boson.

In order to improve the possibility of creating such events, only the beam parameters affect the luminosity. For a Gaussian beam distribution, it can be expressed as the following:

$$L = \frac{{N_b}^2 n f_r \gamma}{4\pi\varepsilon_n\beta^*} \qquad \textbf{\textit{III-2}}$$

N_b and n represent the number of particles per bunch and the number of bunches per beam respectively, fr is the revolution frequency. γ is the relativistic gamma factor. ε_n is the normalized transverse emittance, and β° is the beta function at the collision.

The Large Hadron Collider (LHC) is a sophisticated system made of four main colliders; LHC$_b$, ATLAS, ALICE and CMS. They are connected by a magnetic tube that has the ability to transport energy .It accelerates particles to greater energy order in successive steps. Firstly, protons accelerate to achieve an energy of 50 MeV in the Linear Particle Accelerator (LINAC2), and then the beam is pushed to the Proton Synchrotron Booster (PSB) that accelerates them to an energy of 1.4 GeV. Afterward, the beam will be boosted to reach an energy of 26 GeV scale in the Proton Synchrotron (PS). The Super Proton Synchrotron (SPS) is the final acceleration step, which accelerates protons to 450 GeV before injecting them into the LHC, where their energy can be enhanced to a maximum of 7 TeV. The beams are guided into one of the four colliding nodes, once they achieve the desired peak energy. Figure III.1 provides a schematic of the LHC layout.

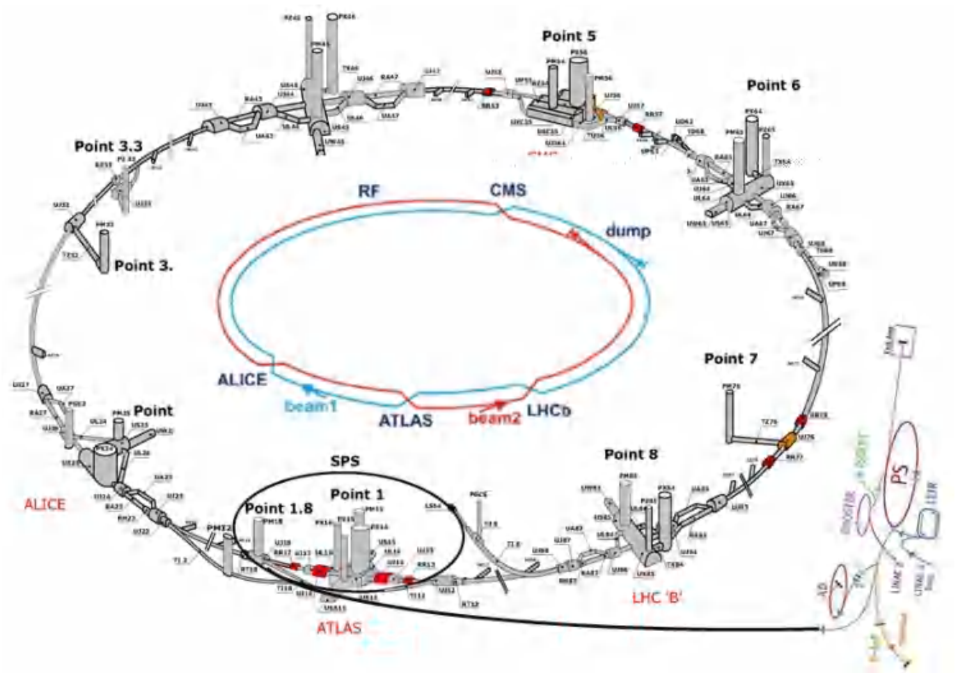

Figure III.1: LHC Layout. Inset of the bigger ring showing the two parallel beam lines and fours collision points of dedicated experiments: ATLAS, CMS, ALICE and LHCb [3].

III.3. Brief history of the LHC:

In 2012, the maximum reported energy in LHC-CERN was 8 TeV. Four years later, a new energy level record was successfully achieved; a proton-proton collision at a massive 13 trillion electron volts. This capacity presents new possibilities for supersymmetry, extra dimensions of space and time, and other “Beyond the Standard Model (BSM)” physics, as well as exploring electroweak symmetry breaking and the Higgs phenomena.

From late 2009 until the end of 2011, the LHC was producing collisions with a center of mass energy of 6.5 TeV. The first long shutdown occurred during the Phase-0 upgrade, which lasted from the beginning of 2013 until the end of 2014.

The machine was tuned to achieve a nominal luminosity of 10^{34} $cm^{-2}s^{-1}$, a center mass energy of up to 14 TeV, and a bunch spacing of 25ns.

In the following years, further important changes were made to comply with the luminosity growth to far greater levels than the existing one.

The second long technical shut down occurred during the upcoming Phase ‘1' upgrade between 2018 and 2020. During this time, the detector and its associated readouts, such as electronics were upgraded in order to cope the luminosity of 2×10^{34} $cm^{-2}s^{-1}$ with a center mass energy of up to 14 TeV and a bunch spacing of 25 ns.

After 2022, there will be a major machine update with an extended shutdown as part of the ‘Phase 2' upgrade. This upgrade aims to produce significantly higher integrated luminosity levels, possibly 5 times higher than those attained at the end of Phase 1. The energy of the center of mass must remain constant at 14 TeV.

However, LHC would eventually need an upgrade to increase the total number of collisions by a factor of 10. The more powerful future LHC would provide more accurate measurements of new particles and enable observation of rare processes that remain unexplored below the present sensitivity level. The future LHC would be more powerful, allowing more precise measurements of new particles, as well as detection of rare phenomena that are still undiscovered at the current sensitivity level.

Small-pitch, thin 3D Si sensors have been developed for the ATLAS Inner Tracker (ITk) and CMS experiment upgrades at the High-Luminosity (HL) LHC.

III.3.1. The ATLAS experiment

ATLAS (A Toroidal LHC ApparatuS) is one of the four main colliders at the Large Hadron Collider (LHC), its cross section is shown in Figure III.2. It is the world's largest volume of the intense magnetic field. The latter consists of many components that are needed to measure the different type of particles produced in the collision, it is important to measure the energy of the particles, which pass through the detector. The inner section measures the tracks of charged particles, which are bended by the magnetic field of a thin superconducting solenoid magnet. Outside of all these, two calorimeter devices measuring the energies of particles. Finally, the muon spectrometer, measuring the tracks of the Muons, which are bended in the field of a superconducting toroidal magnet.

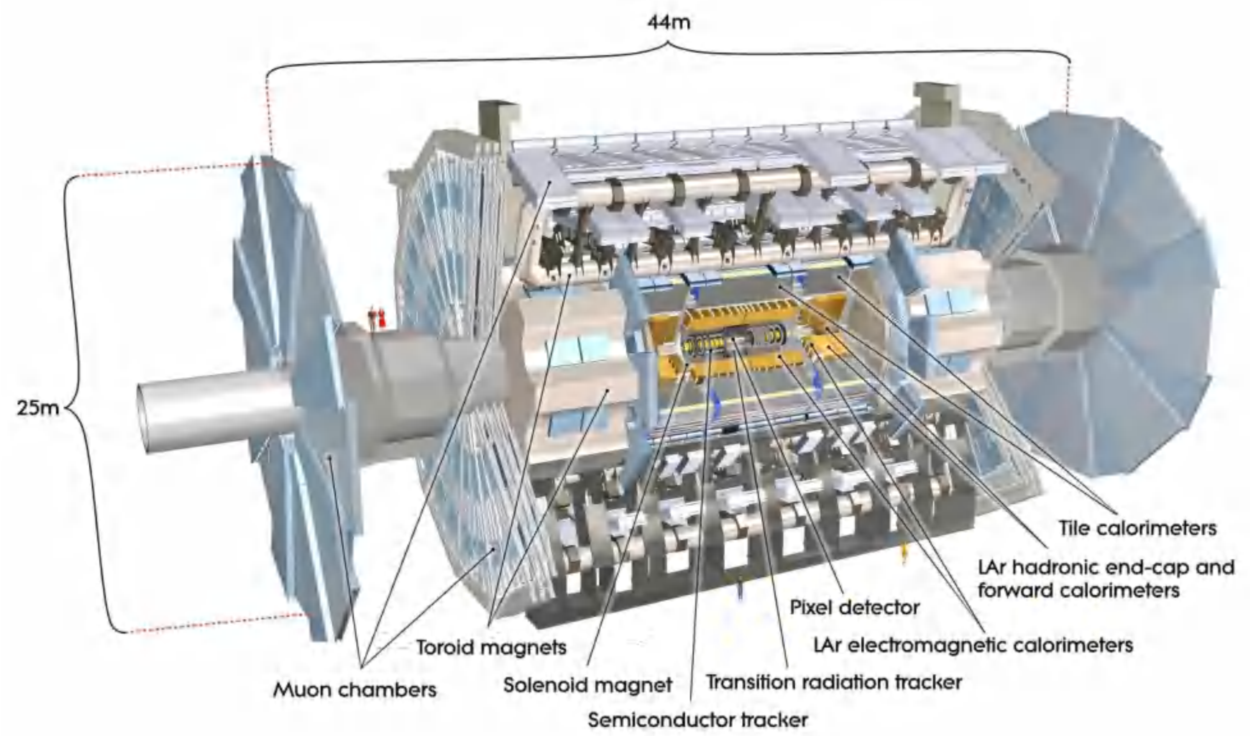

Figure III.2: Schematics of ATLAS particle detector layout [4]

Close to the heart of the detector, several components are designed to measure the trajectory of passing charge particles with an accuracy of close to one hundredth of millimeter. One component is known as the **Transition Radiation Tracker (TRT)** consists of several hundred thousand of tubes filled with gas and gold wires**.** It surrounds the so-called **The Semi-conductor Tracker (SCT).** The innermost layer is the **pixel detector layer that** is very close to the beam pipe .It is composed of several detectors built out of Silicon and divided in millions of thin strip and tiny pixels. Figure III.3 depicts the deposition of distinct layers in detail.

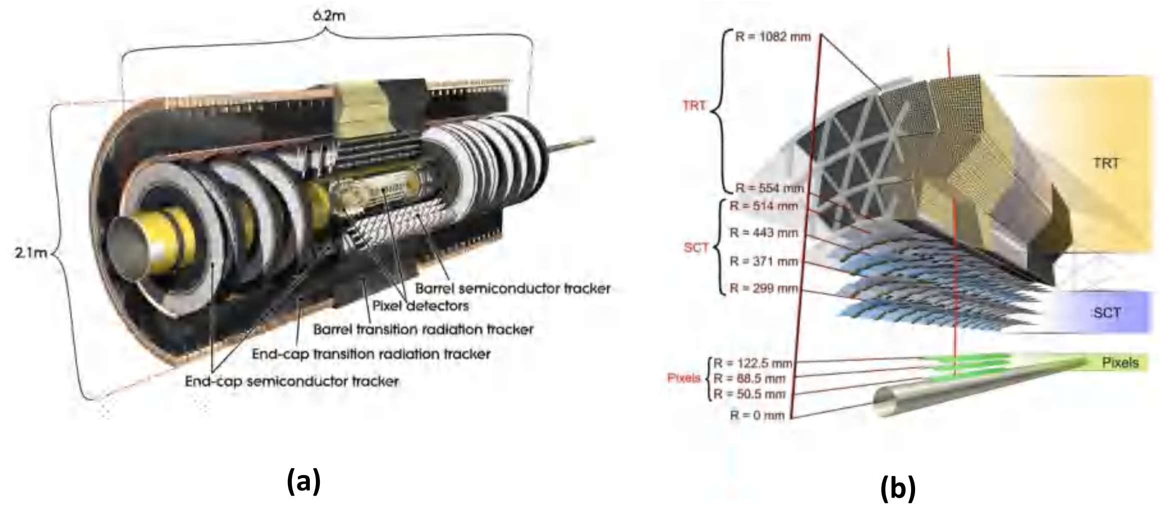

Figure III.3: ATLAS inner detector sensor structure (a) and cross-section with TRT and *(b) Insertable B-layer (IBL) [3].*

The ATLAS detector is designed to measure as many particles as possible and further detector modules are placed at the ends to measure the particles produced at small angles to the proton beams. Toroidal magnets are placed at both ends of the detector to produce the intense magnetic field that ATLAS needs.

III.3.2. The CMS experiment

The CMS (Compact Muon Solenoid) experimental site is located in the French commune of Cessy, about 10 km away from CERN's main campus. It is considered as one of the greatest human’s structures. It is made up of 10.000 tons of iron that is more than the iron in Eiffel Tower. Its gravity force is around 100,000 more than the gravity force on earth. At LHC, there are more than 150 million sensors that record DATA 40 million times per second. The recorded DATA from this collision are enormous. Although the detector is smaller than ATLAS, it performs the same function: it reconstructs high-energy proton-proton collisions produced by the LHC. The CMS is designed in slices. After construction, each slice was lowered through the shaft into the experimental cavern and then assembled on the floor. Close to the interaction region, three Silicon pixels layer were placed, allowing for better measurements of charged particle tracks. A schematic of the CMS detector is shown in Figure III.4.

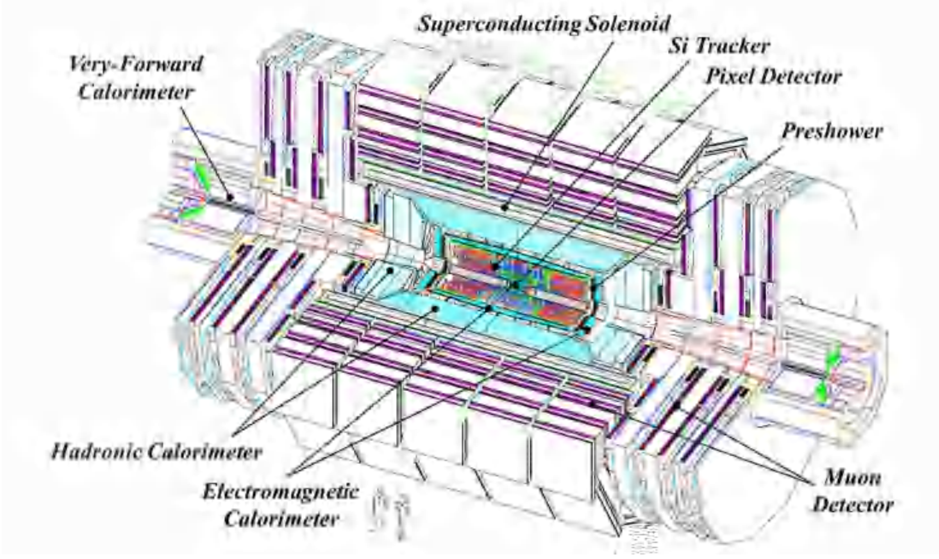

Figure III.4: A schematic of Compact Muon Solenoid (CMS) detector

In 2009, CMS recorded its first collisions between protons, and there were celebrations across the globe. On 4 July 2012, CMS collaboration announced the discovery of a new particle to the world, now confirmed to be a Higgs boson. Physicists continue to search for many new particles and phenomena to resolve the many remaining unanswered questions. Discovering the Higgs boson in 2012 has helped to cement our knowledge of how fundamental particles in the entire universe gain masses. This was the first step for the LHC and it will take years to study the properties of this newly discovered particle. This requires the development of a new generation of pixel sensors. Since the date of the first collision record, only planar sensors are used in the CMS pixel detector.

The 3D Si sensors are still being considered as the most promising detectors for future LHC (HL-LHC). Since this chapter focuses on 3D sensors, the following parts discuss these tempting devices and go more deeply to the sophisticated new Small-pitch 3D pixel sensors.

III.4. 3D radiation detectors

3D Silicon sensors have applications in a wide scope of fields; most outstandingly, they have gotten ready for the use in experiments at the Large Hadron Collider (LHC) because of their high luminosity [4], [5] lower power dissipation and enhanced radiation hardness. Planar detectors have reached their limits at high fluences and are not preferred in this case [3]. The increase in the effective doping concentration would not allow to reach full depletion, and charge trapping could lead to the charge carrier drift length to be at most 50 µm, so that the collected charges would be drastically diminished [6]. Because of that, 3-D detectors emerged.

Indeed, parker et al proposed the first standard 3D detectors in 1997 [7]. This structure presents a 3-D array of vertical columnar electrodes arranged in adjacent cells etched perpendicularly to the wafer surface and penetrating through the entire substrate of a high resistivity Silicon. This architecture certainly offers some advantages with respect to the planar one [8], making 3D detectors ideal candidates for important applications such as in high energy physics (HEP). In 3D detectors, the depletion voltage and collected charges do not depend on the substrate thickness as in the case of planar detectors, but they rather depend on the substrate concentration and the detectors layout. The lower the inter-electrodes distance collected more charges with less collection time. Figure III.5 shows the arrangement of the electrodes; also, how equipotential lines for a quarter of elementary cell are distributed.

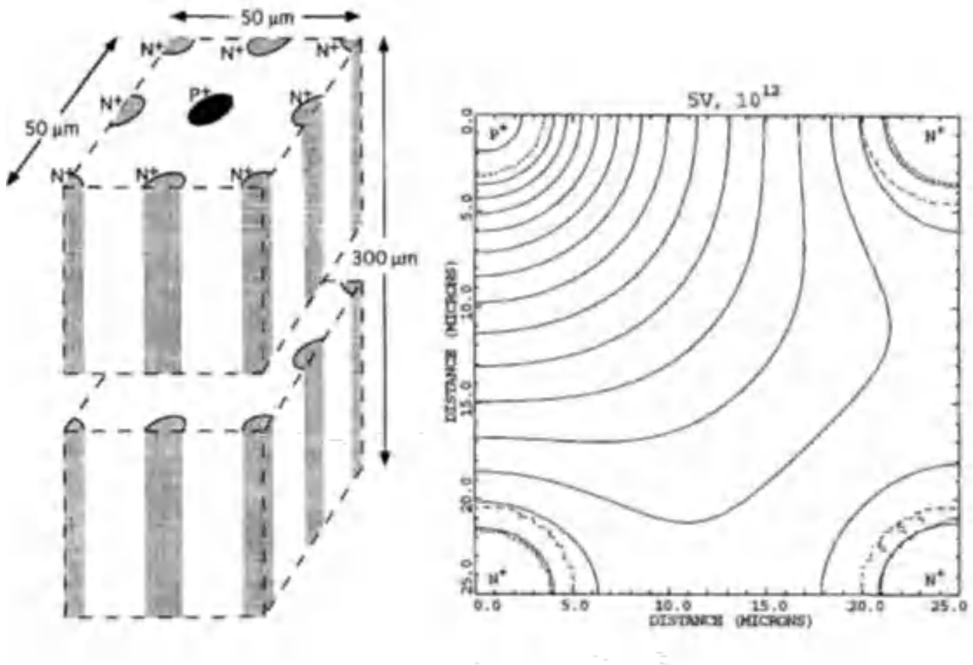

Figure III.5: Simulation results of full 3D detectors. Elementary cell of a 3D detector (a), simulated equipotential lines for a quarter of elementary cell with bulk doping equal to 10^{12} *cm*$^{-3}$ *and bias voltage equal to 5V [7].*

III.4.1. Small-pitch 3D pixel sensors

The innermost tracking layers at the High Luminosity LHC (HL-LHC) would have to tolerate very high radiation fluences up to 2 MeV equivalent neutrons per square centimeter (n_{eq} cm $^{-2}$) [9]. In order to cope with this enhanced luminosity, the INFN-FBK group has developed new low pitch 3D sensors with very dense pixel granularity [10]. They feature pixel sizes of 50×50 µm^2 with 1 readout column, and 25×100 µm^2 with 1 or 2 readout columns (1E and 2E). Figure III.6 illustrates the Layout of these new Small-pitch 3D pixel sensors.

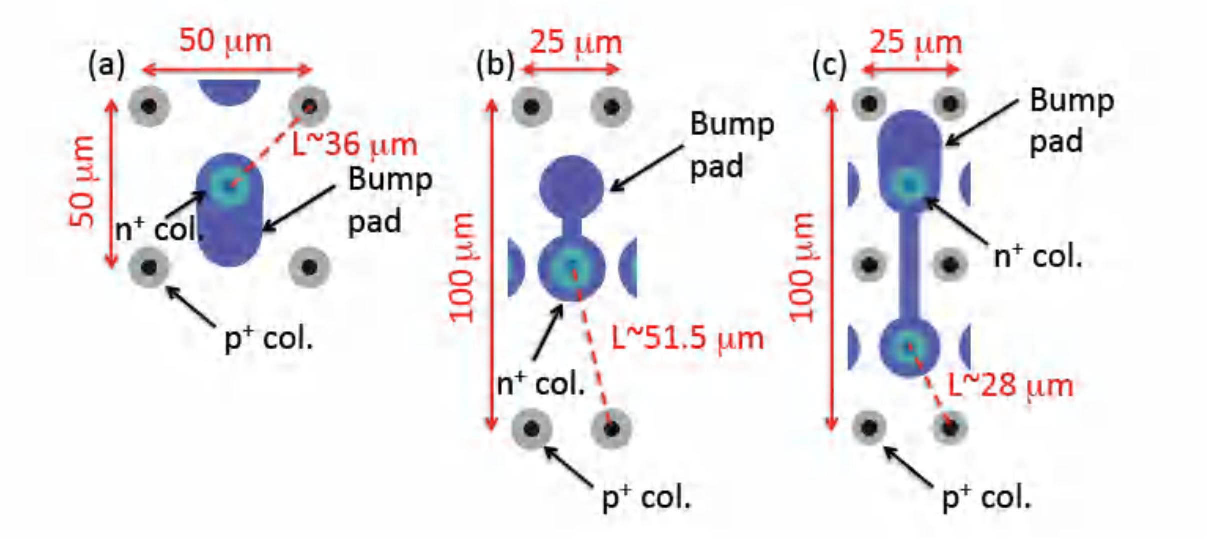

Figure III.6: Layout of small pitch 3D pixels made with single-sided FBK technology : (a) 50×50 µm^2, (b) 25×100 µm^2 (1E), and (c) 25×100 µm^2 (2E) [10] .

These devices are extremely radiation hard owing to the small inter-electrode distance, ranging from ~28 µm to ~51 µm in the considered layouts [11] . In Si-Si Direct Wafer Bonded 6” substrates, devices are produced using the single-sided Technology [12]. The active layer is a high-resistivity, p-type Float Zone Silicon wafer with a thickness of 130 µm (t_{FZ}) that is directly bonded on top of a low-resistivity, p-type handle wafer with a thickness of 500 µm. The depths of the p$^+$ and n$^+$ columns are different. The former penetrates the handle wafer in order to bias the sensor from the backside. The latter, on the other hand, stops 20 µm before attending the handle wafer in order to have a larger breakdown voltage. Both types of columns are passivated after partially filling with doped poly-Si. Metal contacts the n$^+$ columns on the front side, which are isolated by a p-spray layer at the surface. Figure III.7 shows schematic cross-section of the device.

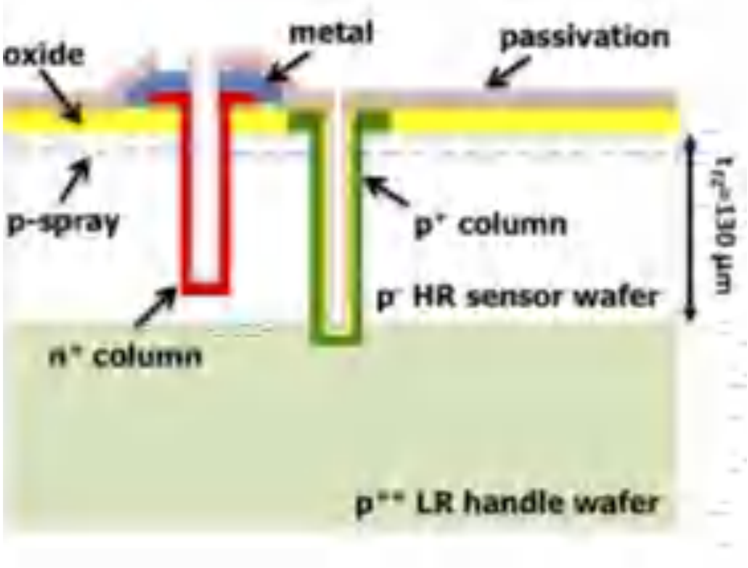

Figure III.7: Schematic cross section of the 3D diodes [13].

The layout of small pitch 3D sensor is very simple, the major drawback is on the basic of the bump-bonding pad which has a very specific size (see Figure III.6, referring to FBK technology with 5 µm column diameter and 20 µm bump pad diameter).

For the size of the two-pixel cases 50×50 μm^2 (Figure 3.6.a) and the 25×100 μm^2 with one read-out electrode (1E, Figure 3.6.b), the bump pad can be positioned safely away from the columns. Although it is so important to mention that for the latest layout there is a serious limitation due to the ~ 51.5 µm inter-electrode spacing (L) that is insufficient for the request of high radiation hardness. A neater solution for this problem is to improve the design by adding another readout electrode (2E,Figure III.6.c) , leading to L ~ 28µm. Although this solution is interesting, it suffers from closer distance between the read out and the Ohmic columns. Consequently, it is very important to use a better lithography system. Another solution is to place the bump-pad directly on top of the columns.

Small-pitch 3D pixel sensors have excellent electrical properties both before and after irradiation [14]. In addition, they exhibit a very promising beam test results, with hit efficiency of 99 percent and 97 percent before and after an irradiation fluence of 1×10^{16} n_{eq} cm^{-2} respectively [12]. The results of position resolved laser tests performed on 3D diodes of various geometries after neutron irradiation up to an extremely high fluence of 3.5×10^{16} n_{eq} cm^{-2} obtained in [13] will be discussed in the following part.

III.4.2. Characterization of FBK small-pitch 3D diodes after neutrons irradiation up to 3.5 10^{16} n_{eq} cm^{-2}

3D diodes from FBK's first batch of small-pitch 3D pixel sensors manufactured using a single-sided technique were under test [15] .The layouts of the considered structures are shown on Figure III.8. As it is shown, devices have distinct small-pitch geometries; each one features an inter-electrode spacing (L). The pixel sizes are 50×50 μm^2 (L~35 µm), 25×100.2E μm^2 (~28 µm) and 25×100.1E μm^2 (~51 µm).

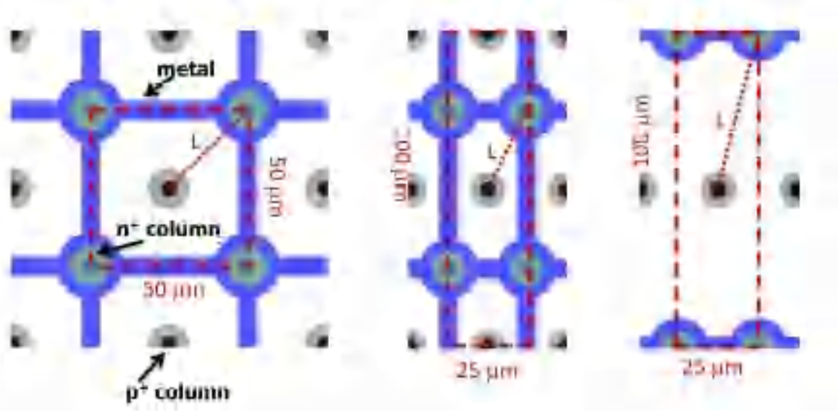

(a) (b) (c)

Figure III.8: Layouts of the different geometries under test, corresponding to the regions of interest for position resolved laser measurements a) 50×50, b) 25×100(2E), and c) 25×100(1E) [13].

At the TRIGA Mark II reactor at JSI (Ljubljana, Slovenia), sensors were irradiated without bias with neutrons at three distinct fluences: 1 × 10^{16}, 2 × 10^{16}, and 3.5 × 10^{16} n_{eq} cm^{-2}. In order to avoid annealing, all irradiated samples were kept in the freezer.

The vacuum chamber was used for functional test, which allow operating the samples at temperature as low as -10 °C without any condensation issues. The samples had a backside biasing, while the microneedles contacted the probing pads on the front side and read out the signals.

Two-dimensional maps of the relative signal intensity across neighboring 3D basic cells are collected using a position resolved pulsed laser (wavelength 1064 nm, nominal pulse width 40 ps); at varied bias voltages, from 25 V to 225 V in increments of 25 V, or until breakdown occurs. The laser pulses are concentrated on the sensor surface, with a Gaussian spatial distribution and a standard deviation of roughly 5 µm for the laser point. The laser is moved with 1 μm accuracy in both the X and Y axes by PC-controlled motorized stages.

The measurements with a laser are not typically recognized as a good tool to have absolute value of efficiencies, but they are rather a good tool to have an idea of a relative efficiency and the position dependence. In order to make the measurements quantitative the efficiency was scaled according to the pre-irradiation one. The radiation dependence of the light absorption coefficient (α) has been taken into account. According to [12], the value of alpha based on fluence (ϕ), wavelength (λ) and temperature (T) were determined as follows:

$$\alpha(\emptyset,\lambda,T)=\alpha_0(\lambda,T)\left[1+\frac{\emptyset}{\emptyset_{abs}\ (\lambda)}\right] \qquad \textbf{\textit{III-3}}$$

α_0 is the absorption coefficient before irradiation, computed at -10 °C using the model proposed in [16] and at λ=1064 nm, the coefficient **ϕ abs** has been considered to be 3.37 ± 0.36 × 10^{16} cm^{-2} .

Therefore, after irradiation, there is a change in the penetration depth or the absorption coefficient of the light. As so, it is not possible to make a straight forward normalization of the signal post dividing to signal before, that would not give an accurate result . It is necessary to check how much the absorption depth before and after irradiation, giving the finite thickness of the active region (the light absorption length at 1064 nm ~1mm is significantly longer than t_{FZ}=130 μm) in the two cases, which is the parameter on which it should normalize both the pre-irradiation and the post irradiation numbers. Then, it is possible to make the ratio of the two quantities.

Equation III-4 based on Lambert-Beer equation has been used to calculate the charge in the various samples:

$$\alpha(\emptyset,\lambda,T,t_{FZ})=Q_0(\lambda,T)[1-\exp(-\alpha(\emptyset,\lambda,T).t_{FZ})] \qquad \textbf{\textit{III-5}}$$

Q_0 represents the proportionality factor, which is in the end deleted in the signal normalization.

Table III-1lists all of the relevant values that were utilized in the calculations. The signals measured in irradiated samples were divided by the scaling factor given in the last column of Table III-1, which corresponds to the charge released by the laser in irradiated and non-irradiated samples, and then normalized to the maximum signals measured before irradiation.

Table III-1: Summary of results on 1064 nm light absorption at -10 ° C and charge discharged in the 130µm thick active layer before and after fluence irradiation. In the scaling factor, the uncertainties on the values are at most 5% [13].

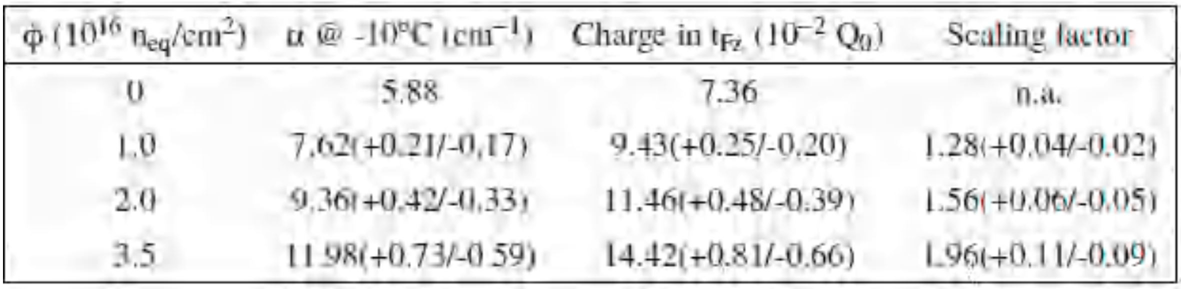

ϕ (10^{16} n_{eq}/cm^2)	α @ -10°C (cm^{-1})	Charge in t_{Fz} (10^{-2} Q_0)	Scaling factor
0	5.88	7.36	n.a.
1.0	7.62(+0.21/-0.17)	9.43(+0.25/-0.20)	1.28(+0.04/-0.02)
2.0	9.36(+0.42/-0.33)	11.46(+0.48/-0.39)	1.56(+0.06/-0.05)
3.5	11.98(+0.73/-0.59)	14.42(+0.81/-0.66)	1.96(+0.11/-0.09)

III.4.2.1. 3D diode of 50 × 50 type

The measured two –dimensional maps of signal efficiency (SE) at different voltages in the sample irradiated at 1 × 10^{16} n_{eq} cm^{-2} are provided on Figure III.9. The SE is low everywhere at 25 V, then progressively rises to high levels at 125 V, and finally exceeds a hundred percent at 225 V. In all maps, the SE has higher values in the areas close to the p^+ columns, while the lowest values are in the areas covered by metals. Due to the non-negligible size of the light spot and the fact that columns are partially empty, metal does not fully cover/shield their center; the signals are seen in the p^+ columns. However, the efficiency in these areas are not significant because the quality of the released charge cannot be estimated there.

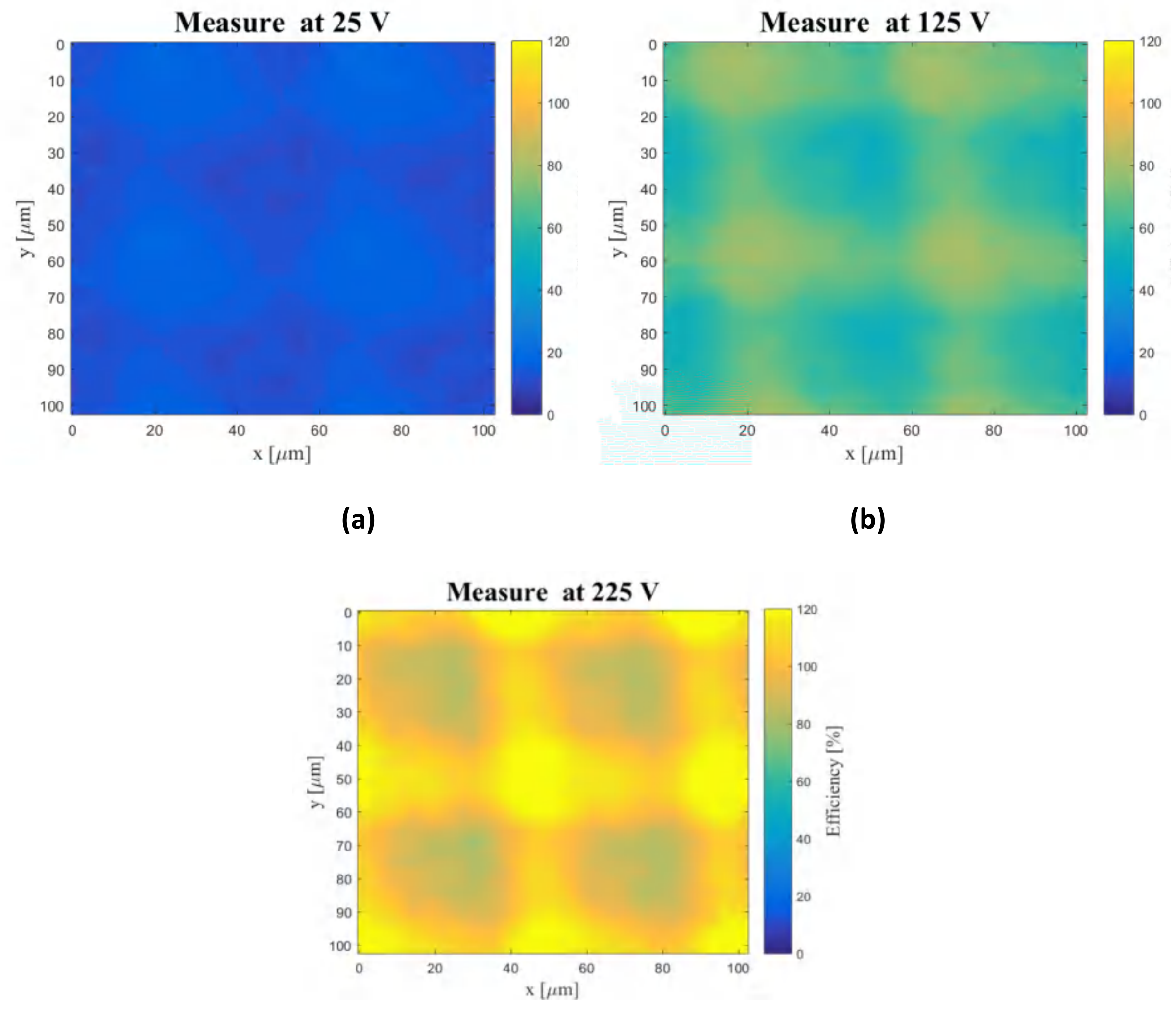

(a) (b)

(c)

Figure III.9: Signal efficiency maps in a (50µm × 50µm) 3D diode irradiated at 1 × 10^{16} n_{eq} cm^{-2} at three bias voltages: a) 25 V, b) 125 V, and c) 225 V [13].

Figure III.10 provides 1D projections of the measured signal efficiency at different Vbias for the three considered fluences are taken along cuts between the centers of readout n+ column (0) and a p+ column (~35 µm) in the slices a, b, and c. The SE increases with voltage in a consistent manner at all positions, although it is more prominent towards the p+ column, especially at the highest voltages. Figure 10d shows the average values of curves from Figure III.10 (a,b,c) as a function of applied voltage, eliminating those related to the region covered by metal. At all the fluences, the SE increases with the applied voltage, reaching values more than 100% at 1 x10^{16} n_{eq} cm^{-2} and 2 × 10^{16} n_{eq} cm^{-2}, and around 80% at 3.5 10^{16} n_{eq} cm^{-2}.

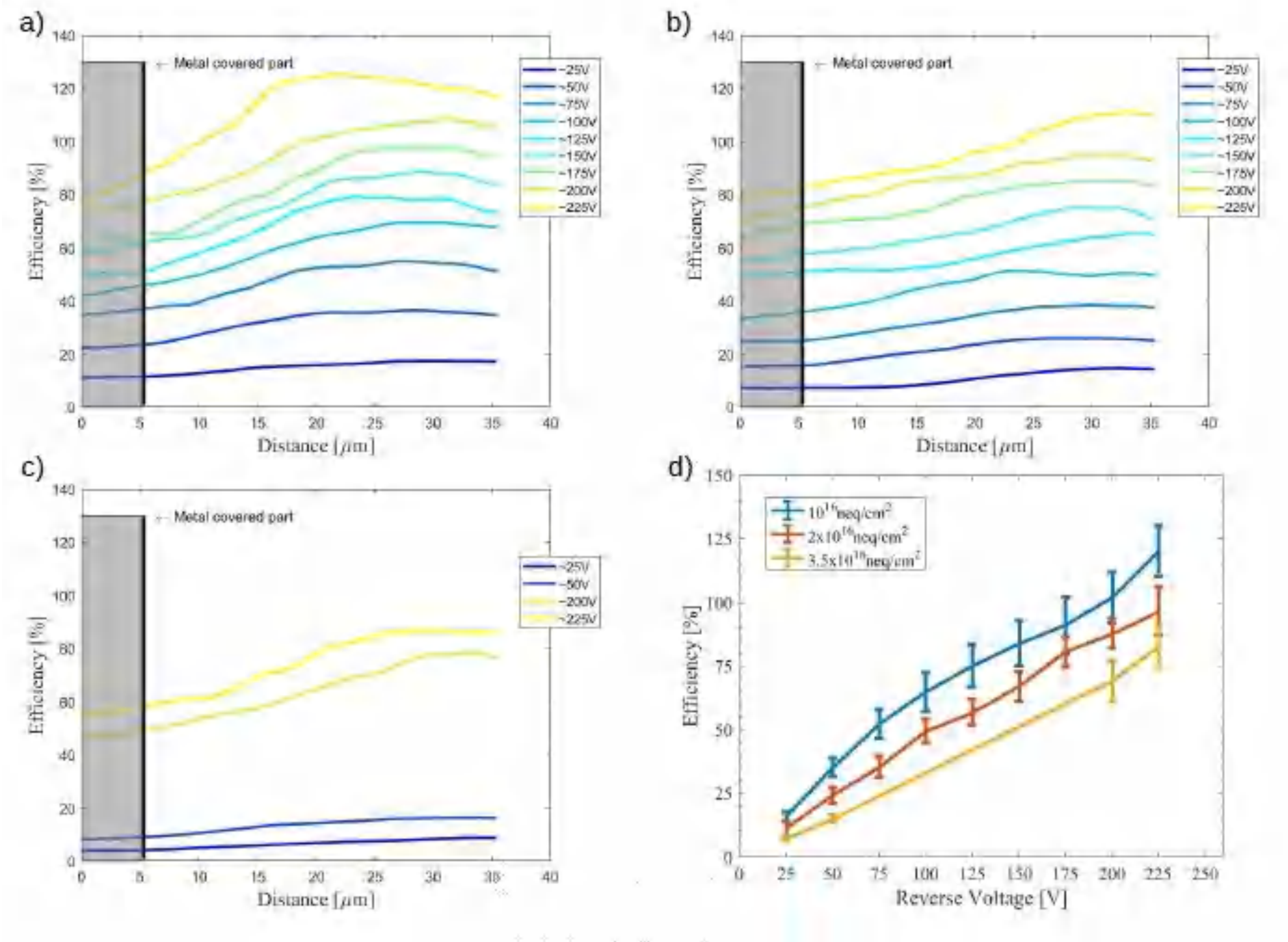

Figure III.10: 1D projections of the measured signal efficiency at different Vbias for the three considered fluences taken along cuts between the centers of readout n^+ column (0) and a p^+ column (~35 μm) in the slices : a) 1×10^{16} n_{eq} cm^{-2}, b) 2×10^{16} n_{eq} cm^{-2}, and c) 3.5×10^{16} n_{eq} cm^{-2}, d) The average values of curves as a function of applied voltage [13].

III.4.2.2. 3D diode of 25 × 100(2E) type

The measured two dimensional maps of signal efficiency (SE) in the sample irradiated at the three different fluences at 150 V are provided in Figure III.11. Less collected charges are obtained as the fluence increases; this comparison clearly shows how radiation damage has a greater impact on efficiency (higher fluence means higher radiation damage).

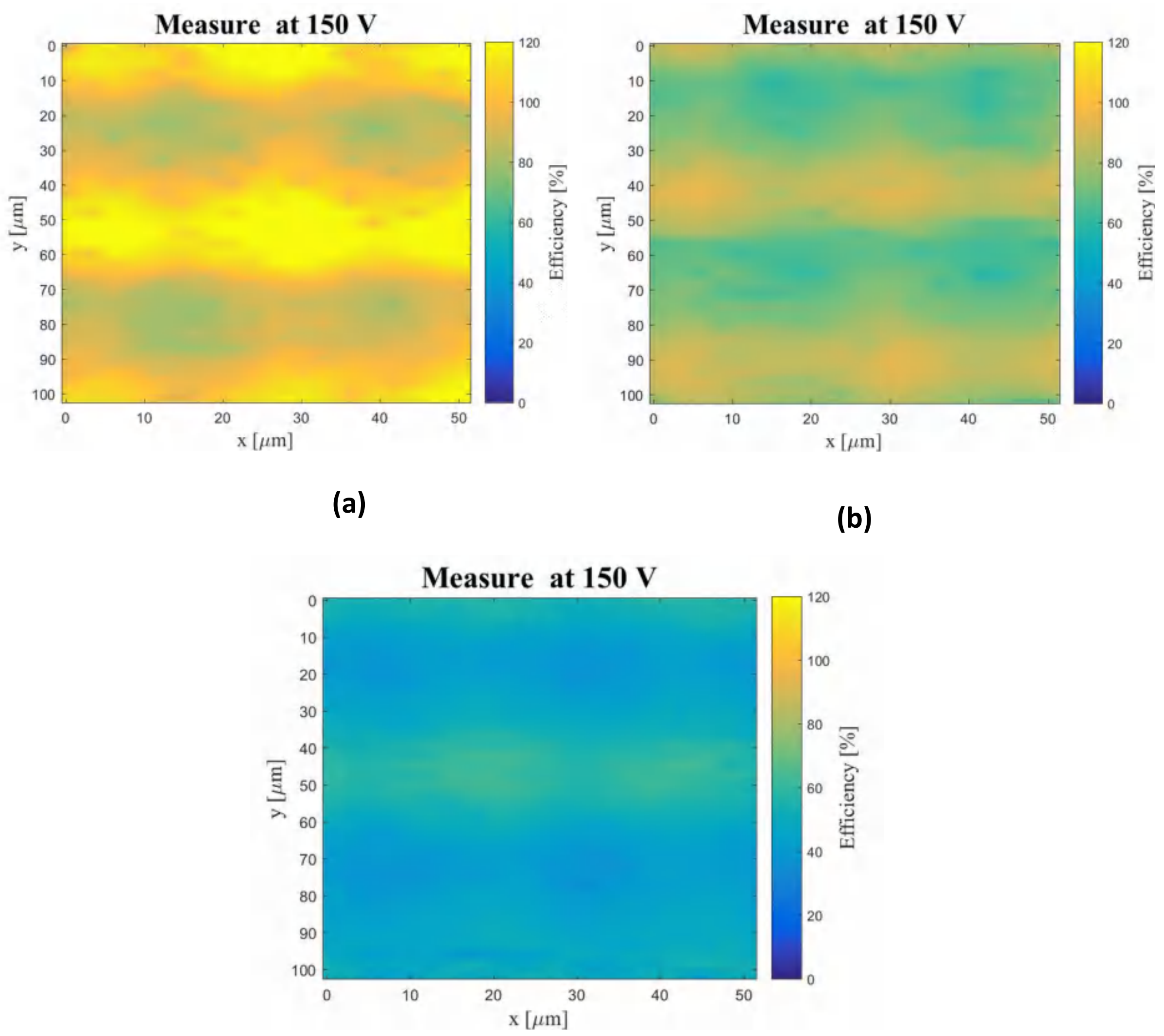

(a)

(b)

(c)

Figure III.11: The measured two –dimensional maps of signal efficiency (SE) in the 25 × 100(2E) diodes irradiated at the three different fluences at 150 V [13].

1D projections of the measured signal efficiency at different V_{bias} for the three considered fluences are taken along cuts between the centers of readout n^+ column (0) and a p^+ column (~28 µm) in the slices a, b, and c. The results are similar to those obtained for the (50 µm × 50 µm) structure. However, figure 5d shows a quasi-saturation SE due to the short inter-electrode distance (L~28 µm), which results a smaller depletion voltage. It is worth noting that in the sample irradiated at 1×10^{16} n_{eq} cm^{-2}, the curve has a smooth climb after the knee at approximately 50 V, which is consistent with the device's early breakdown at about 150 V.

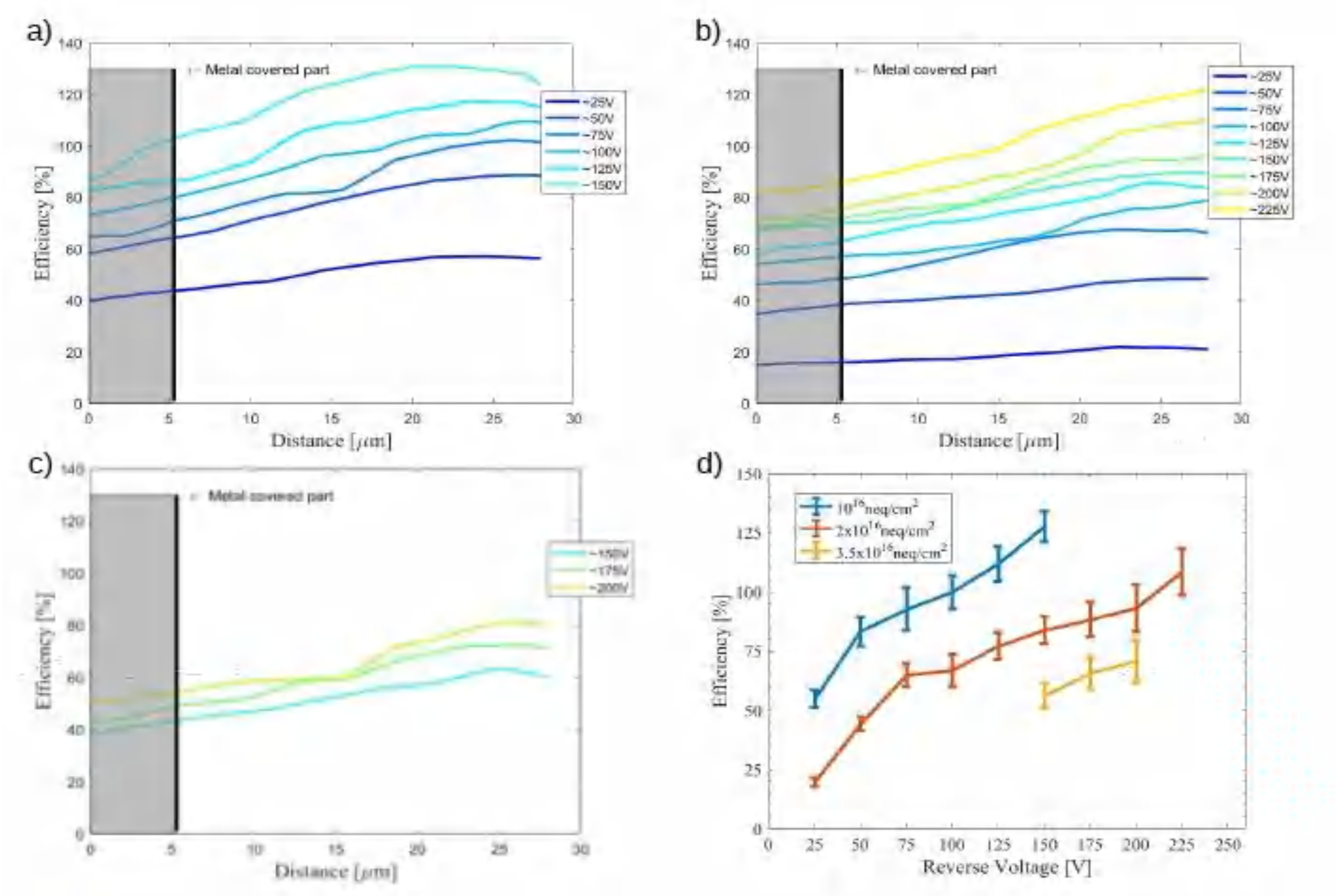

Figure III.12: 1D projections of the measured signal efficiency at different Vbias for the three considered fluences taken along cuts between the centers of readout n+ column (0) and a p+ column (~28 µm) in the slices: a) 1 × 10^{16} n_{eq} cm^{-2}, b) 2 × 10^{16} n_{eq} cm^{-2}, and c) 3.5 × 10^{16} n_{eq} cm^{-2}, d) The average values of curves as a function of applied voltage [13].

III.4.2.3. 3D diode of 25 × 100 (1E) type:

Figure III.13 provides The 1D projections of the measured signal efficiency at different V_{bias} until the breakdown for a fluence of 2 × 10^{16} n_{eq}.cm^{-2} are taken along cuts between the centers of readout n+ column (0) and a p+ column (~51µm) in the slice a. Due to the larger value of L, the efficiency in this device are significantly lower than in the others. The region closest to the n+ column has the greatest values, with a secondary peak near the p+ column.

The signal efficiencies as a function of voltage in 3D diodes of different geometries irradiated at 2 × 10^{16} neq.cm-2 is shown in slice b. The results confirms that the SE is in inversely proportional to the inter-electrodes distance.

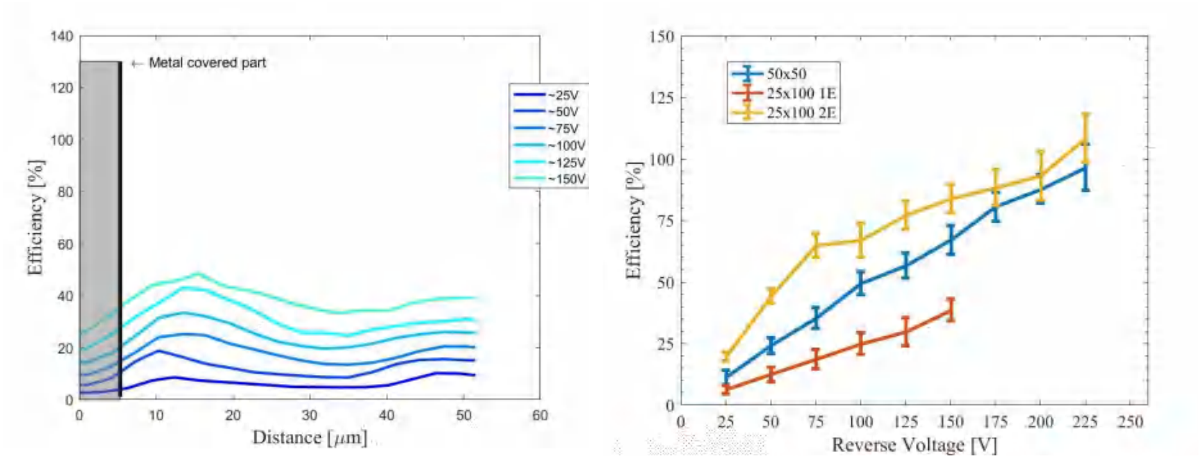

Figure III.13: a) Signal efficiency as a function of distance along a line connecting the center of a n^+ *column (0) to the center of a p+ column (~51 µm) at different bias voltages in a 3D diode of 25 × 100(1E) type irradiated at 2 ×* 10^{16} $n_{eq}.cm^{-2}$*; b) signal efficiencies as a function of voltage in 3D diodes of different geometries irradiated at 2 ×* 10^{16} $n_{eq}.cm^{-2}$

Figure III.14 and Figure III.15 provide the I-V results achieved with measurements on four $2mm^2$ FBK diodes, where the ncolumns are shorted together and irradiated in Ljubljana to a fluence of 1.0 × 10^{16} neq.cm-2 and 1.5 × 10^{16} neq.cm-2. As expected, the measurement results were in good agreement with CNM diodes 25x100-1E,they may reach an operating voltage of 100-160V. Lower voltages is required for the 50× 50 structure (90-120V).

It is clearly seen that the 25 × 100 structure are showing lower current, which lead to a smaller power dissipation at the same voltage. In addition, the spread between the different diodes is higher than the effects of higher dose [17].

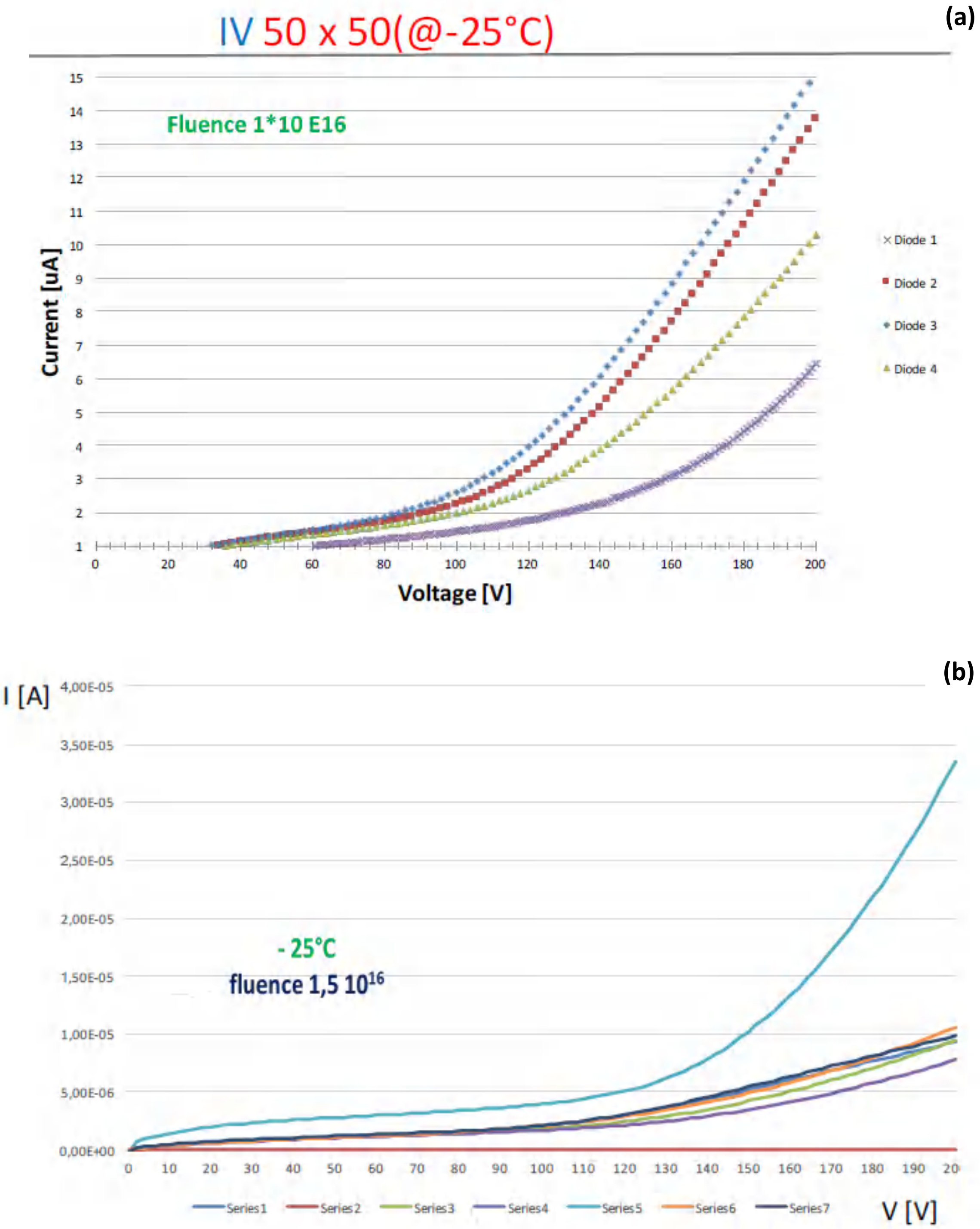

Figure III.14: The I–V results achieved with measurements on four 2mm^2 FBK 50 × 50 diodes irradiated in Ljubljana to a fluence of a) 1.0 × 10^{16} n$_{eq}$.cm^{-2}, b) 1.5 × 10^{16} n$_{eq}$.cm^{-2} [16].

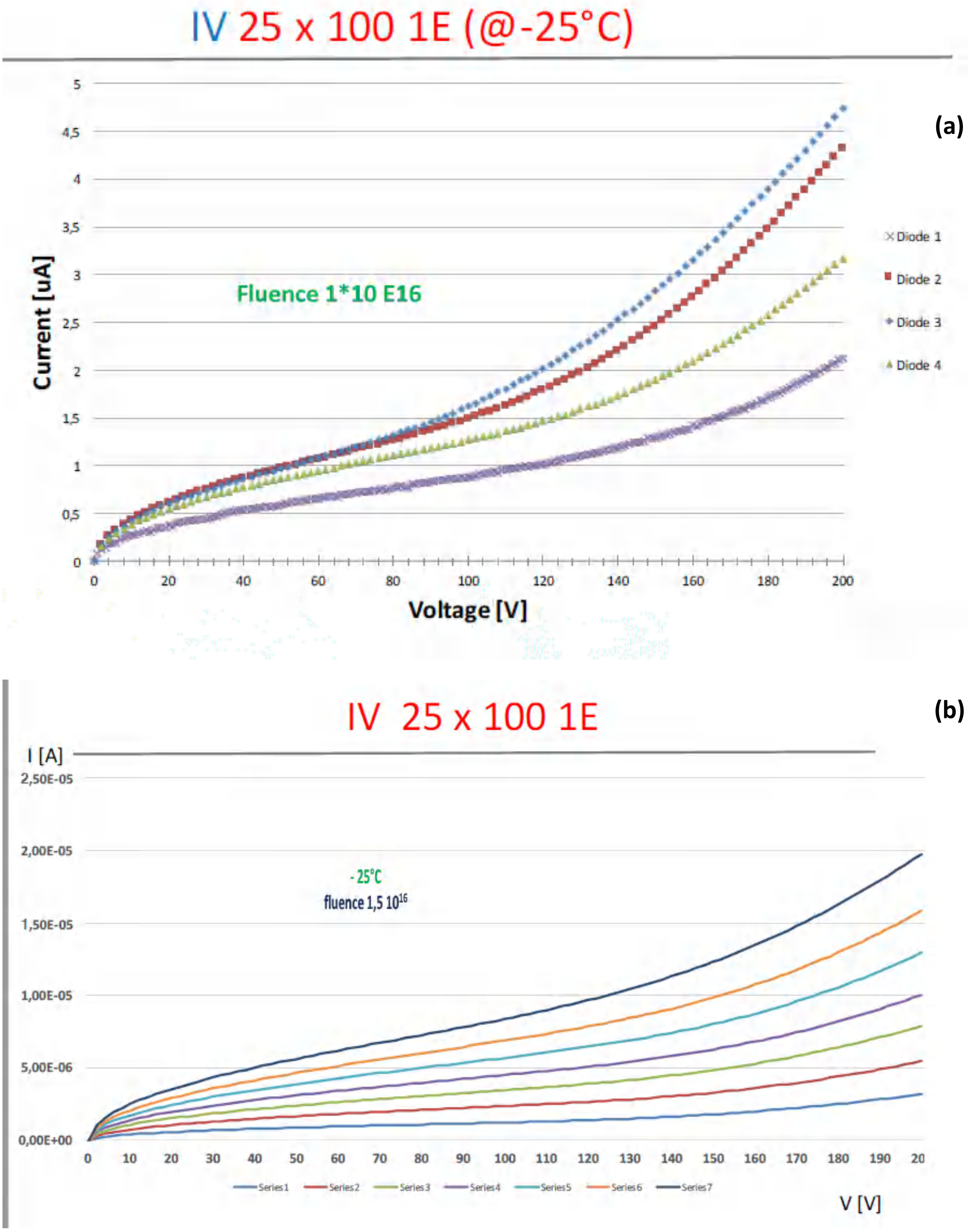

Figure III.15 :The I–V results achieved with measurements on four 2mm^2 FBK 25 × 100.1E diodes irradiated in Ljubljana to a fluence of a) 1.0 × 10^{16} neq.cm-2, b) 1.5 × 10^{16} n$_{eq}$.cm^{-2} [16].

III.5. Conclusion:

The radiation hardness of FBK small-pitch 3D sensors irradiated up to extremely large fluences has so far been measured on test structures. The results confirm that they are the natural candidates for the innermost tracking layers of the major detector upgrades at the High Luminosity LHC (HL-LHC) due to their very high radiation tolerance, very high signal efficiency, which is also boosted by charge multiplication effects. These very promising results heighten the need for further investigation using TCAD simulation in order to explain the evolution of the SE with voltage at different positions within the 3D cell, furthermore, for design/optimization of these devices. The following chapter will investigate in details the different experimental obtained quantities, using two of the most accurate radiation bulk damage models.

III.6. References

[1] Evans L " The Large Hadron Collider", *New J. Phys.* **9** 335–335, 2007

[2] "LHC design report", Volume I, "The LHC main ring", June 4th, 2004, CERN-2004-003.

[3] ATLAS website: http://www.atlas.ch/.

[4] McDuff H, Hoeferkamp M R, Seidel S, Wang R, Kenney C J, Hasi J and Parker S I The effect of humidity on reverse breakdown in 3D Silicon sensors *Nuclear Instruments and Methods in Physics Research Section A: Accelerators, Spectrometers, Detectors and Associated Equipment* **785** 1–4, 2015

[5] Kenney C J, Parker S and Walckiers E Results from 3-D Silicon sensors with wall electrodes: near-cell-edge sensitivity measurements as a preview of active-edge sensors *IEEE Transactions on Nuclear Science* **48** 2405–10, 2001

[6] Bruzzi M, Adey J, Al-Ajili A, Alexandrov P, Alfieri G, Allport P P, Andreazza A, Artuso M, Assouak et al Radiation-hard semiconductor detectors for SuperLHC *Nuclear Instruments and Methods in Physics Research Section A: Accelerators, Spectrometers, Detectors and Associated Equipment* **541** 189–201, 2005

[7] Parker S I, Kenney C J and Segal J 1997 3D — A proposed new architecture for solid-state radiation detectors *Nuclear Instruments and Methods in Physics Research Section A: Accelerators, Spectrometers, Detectors and Associated Equipment* **395** 328–43

[8] Betta G D, Bagolini A, Boscardin M, Giacomini G, Povoli M, Vianello E and Zorzi N 2011 Development of active and slim edge terminations for 3D and planar detectors *2011 IEEE Nuclear Science Symposium Conference Record* 2011 IEEE Nuclear Science Symposium Conference Record pp 1334–40

[9] Dalla Betta G-F, Boscardin M, Darbo G, Mendicino R, Meschini M, Messineo A, Ronchin S, Sultan D M S and Zorzi N 2016 Development of a new generation of 3D pixel sensors for HL-LHC *Nuclear Instruments and Methods in Physics Research Section A: Accelerators, Spectrometers, Detectors and Associated Equipment* **824** 386–7

[10] Dalla Betta G-F, Boscardin M, Mendicino R, Ronchin S, Sultan D M S and Zorzi N 2015 Development of new 3D pixel sensors for phase 2 upgrades at LHC *2015 IEEE Nuclear Science Symposium and Medical Imaging Conference (NSS/MIC)* 2015 IEEE Nuclear Science

Symposium and Medical Imaging Conference (NSS/MIC) (San Diego, CA, USA: IEEE) pp 1–4

[11] Dalla Betta G-F, Mendicino R, Sultan D, Boscardin M, Giacomini G, Ronchin S, Zorzi N, Darbo G, Meschini M and Messineo A 2017 Small pitch 3D devices *Proceedings of The 25th International workshop on vertex detectors — PoS(Vertex)* The 25th International workshop on vertex detectors (La Biodola, Isola d'Elba, ITALY: Sissa Medialab) p 028, *2016*

[12] Oide H, Alimonti G, Boscardin M, Betta G-F D, Darbo G, Ficorella F, Fumagalli E, Gariano G, Gaudiello A, Gemme C, Meschini M, Messineo A, Mendicino R, Ronchin S, Rovani A, Ruscino E, Sultan D M S, Zorzi N and Furelos D V INFN-FBK developments of 3D sensors for High-Luminosity LHC, *Nuclear Instruments and Methods in Physics Research Section A: Accelerators, Spectrometers, Detectors and Associated Equipment* **924** 73–7, 2019

[13] Mendicino R, Boscardin M and Betta G-F D Characterization of FBK small-pitch 3D diodes after neutron irradiation up to 3.5×10^{16} n_{eq} cm^{-2} , *Journal of Instrumentation* **14** C01005–C01005, 2019

[14] Betta G-F D, Boscardin M, Hoeferkamp M, Mendicino R, Seidel S and Sultan D M S Electrical characterization of FBK small-pitch 3D sensors after γ-ray, neutron and proton irradiations *J. Inst.* **12** C11028–C11028,2017

[15] Sultan D M S, Dalla Betta G-F, Mendicino R, Boscardin M, Ronchin S and Zorzi N First production of new thin 3D sensors for HL-LHC at FBK *J. Inst.* **12** C01022–C01022, 2017

[16] C. Scharf, Radiation damage of highly irradiated Silicon sensors, Ph.D. thesis, University of Hamburg, Hamburg, Germany, July 2018.

[17] A. Lapertosa et al., "Performance of irradiated FBK 3D sensors for the ATLAS ITk pixel detector", 16th Trento Workshop on Advanced Silicon Radiation Detectors, Feb. 2021

Chapter 04

IV.1. Introduction

Due to their unique architecture, featuring a short distance between vertical electrodes, 3D pixels are the most radiation-hard silicon sensors [1]. After being used for the first time in the ATLAS Insertable B-Layer [2], they have become natural candidates for the innermost tracking layers of the major detector upgrades at the High Luminosity LHC (HL-LHC). This application has pushed the requirements to the detectors at unprecedented levels in terms of very high hit-rate capabilities and extreme radiation hardness. To this purpose, a new generation of 3D pixels has been developed, having very dense granularity, and reduced active thickness (~150 µm). Two pixel sizes have been considered, compatible with the new read-out chips designed by the RD53 Collaboration [3]: 50×50 μm^2 with 1 readout column, and 25×100 μm^2 with 1 or 2 readout columns (1E and 2E). Besides maintaining the occupancy at ~% level and improving the spatial resolution, these small-pitch 3D geometries feature a reduced inter-electrode distance, ranging from ~28 µm to ~51 µm in the considered layouts, thus enhancing the radiation hardness [1, 4].

Since 2013, in the framework of an R&D program funded by INFN, several batches of small-pitch 3D sensors aimed at the ATLAS and CMS upgrades were fabricated at FBK using a single-sided technology on Si-Si Direct Wafer Bonded 6” substrates [5-7]. Pixel sensors compatible with different read-out chips (ATLAS FEI4, CMS PSI46dig, and RD53A) were tested under particle beams before and after irradiation, showing a very high hit efficiency of ~97% after an irradiation fluence of 1×10^{16} n_{eq} cm^{-2}[8-10]. Further tests aimed at assessing the performance up to ~2× larger fluences of interest for the HL-LHC experiments are under way. The radiation hardness of FBK small-pitch 3D sensors irradiated up to extremely large fluences has so far been measured on test structures: the results of position resolved laser tests performed on 3D diodes of various geometries after neutron irradiation up to 3.5×10^{16} n_{eq} cm^{-2} are discussed in [11], showing very high signal efficiency, also boosted by charge multiplication effects.

In this chapter, we are interested in developing TCAD simulations by Synopsys Sentaurus, incorporating advanced radiation damage models such as [12],[13]. The goal is the design/optimization of new 3D pixel sensors. The biggest challenge for these models is to yield a good agreement with experimental data such as the electric field, the I-V curves, the charge collection efficiency and correctly predicting the charge multiplication effects observed in the measurements at high voltages. In adition, extending our preliminary studies [14,15], we compare the accuracy of two advanced bulk damage models in predicting the signal efficiency of small-pitch 3D sensors irradiated at different fluences in the range of interest for HL-LHC, and its evolution with the bias voltage at different positions within the 3D cell. Selected simulation results will be reported in comparison to experimental data from [11].

IV.2. The used damage models

The proposed new combined TCAD radiation damage modelling scheme (Perugia model) incorporates both bulk and surface radiation damage effects. The related parameters (NOX, NIT) extracted from experimental measurement are the keys for establishing the model. This model was validated by comparing simulation findings with experimental measurements performed at very high fluence (2×10^{16} 1 MeV equivalent n_{eq} cm^{-2}) [12].

The model proposed by A. Folkestad et al. has kept the same number of bulk defect levels as The Perugia one, it has tuned for *p*-type silicon also. Both models use two acceptors and one donor but with different parameters. Table IV-1 summarizes the bulk defects for both models with the fluences limitations.

Table IV-1: The radiation damage models parameters for Perugia model [12]

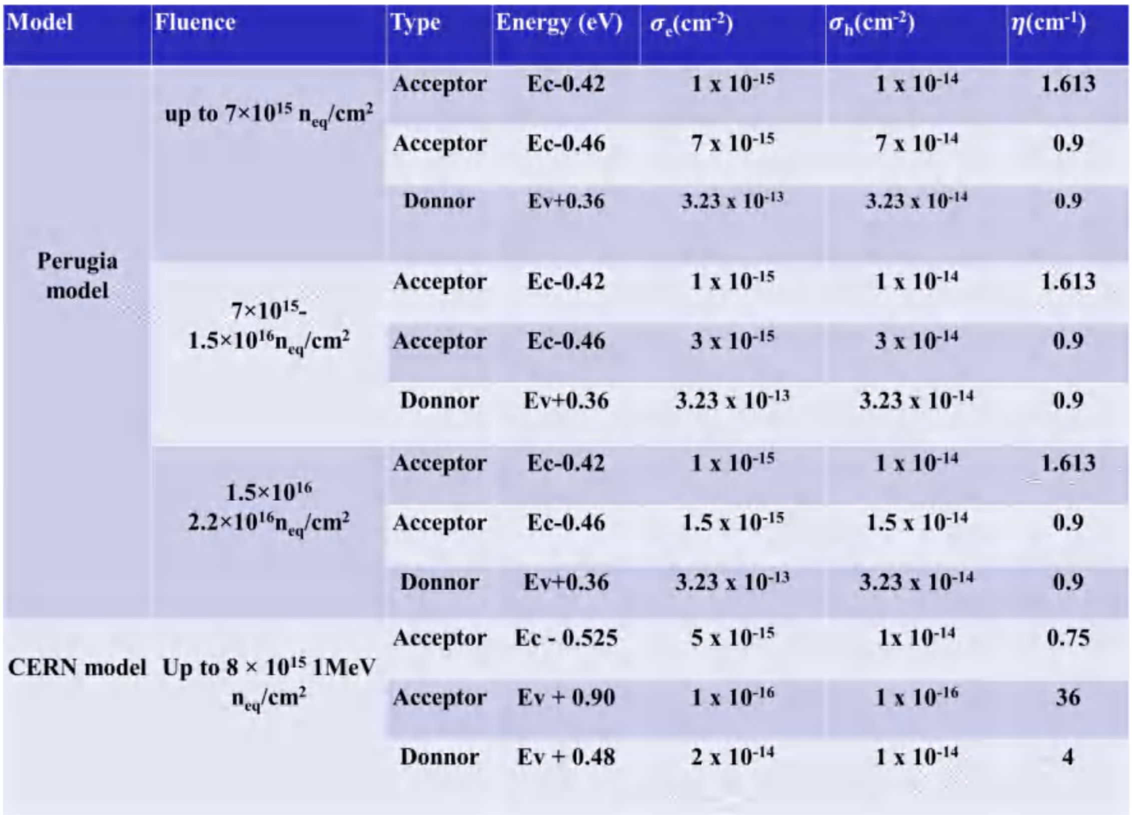

Model	Fluence	Type	Energy (eV)	σ_e(cm^{-2})	σ_h(cm^{-2})	η(cm^{-1})
Perugia model	up to 7×10^{15} n_{eq}/cm^2	Acceptor	Ec-0.42	1×10^{-15}	1×10^{-14}	1.613
		Acceptor	Ec-0.46	7×10^{-15}	7×10^{-14}	0.9
		Donnor	Ev+0.36	3.23×10^{-13}	3.23×10^{-14}	0.9
	7×10^{15}- $1.5\times10^{16}n_{eq}$/cm^2	Acceptor	Ec-0.42	1×10^{-15}	1×10^{-14}	1.613
		Acceptor	Ec-0.46	3×10^{-15}	3×10^{-14}	0.9
		Donnor	Ev+0.36	3.23×10^{-13}	3.23×10^{-14}	0.9
	1.5×10^{16} $2.2\times10^{16}n_{eq}$/cm^2	Acceptor	Ec-0.42	1×10^{-15}	1×10^{-14}	1.613
		Acceptor	Ec-0.46	1.5×10^{-15}	1.5×10^{-14}	0.9
		Donnor	Ev+0.36	3.23×10^{-13}	3.23×10^{-14}	0.9
CERN model	Up to 8×10^{15} 1MeV n_{eq}/cm^2	Acceptor	Ec - 0.525	5×10^{-15}	1×10^{-14}	0.75
		Acceptor	Ev + 0.90	1×10^{-16}	1×10^{-16}	36
		Donnor	Ev + 0.48	2×10^{-14}	1×10^{-14}	4

On the other hand, this model focused on the trap levels from EVL-model that Eber and CMS used, trying to reproduce only the bulk effects, which is not the case for the Perugia one. The CERN model has been tested for a temperature range from (-38 °C to -31 °C on a variety of sensors with different levels of radiation and profiles with fluence up to 8×10^{15} 1MeV $n_{eq}.cm^{-2}$

IV.3. Simulation approach

TCAD simulations were performed by Synopsys Sentaurus, aimed at evaluating the signal efficiency (SE) that is defined as the ratio of the charge signal amplitude after irradiation and before irradiation. To this purpose, keeping into account that the electric field in the vertical direction is uniform for most of the sensor depth, a simplified quasi-2D domain was used, consisting of a sensor slice, 1-µm thick, taken at half the depth of the structures. Simulations also exploit the inherent 3D pixel symmetry to minimize the number of grid points and therefore the simulation time.

The simulated structures consist of a 1/4 of a pixel in case of the 50×50-1E and 25×100-1E pixels, and of 1/8 of a pixel in case of the 25×100-2E pixel (see Figure IV.1).

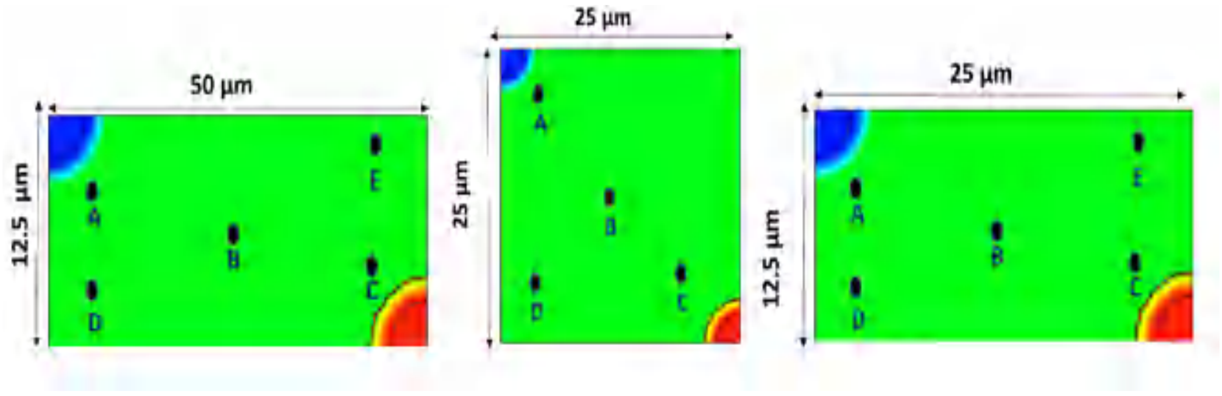

(a) (b) (c)

Figure IV.1: Simulation domains a the different 3D pixel sensors and exploiting the symmetry in the 3D cells: a) 25×100-1E, b) 50×50-1E, and c) 25×100-2E

The readout column is n shown in red at the bottom right corner, the bias column in blue at the top left corner. The simulated hitting points are also shown, and their coordinates are detailed in Table IV-2

Table IV-2: Coordinates of different hit points within the simulation domains of the three pixel structures.

Structures	**25×100-1E**		**50×50-1E**		**25×100-2E**	
Hit point	X (µm)	Y (µm)	X (µm)	Y (µm)	X (µm)	Y (µm)
A	2	4	5.6	5.6	5.9	4
B	25	6.25	12.5	12.5	12.5	6.25
C	48	8.5	19.1	19.1	19.1	8
D	2	10.5	5.6	19.1	5.9	8
E	48	2	-	-	19.1	4

Simulations use typical models (e.g., effective intrinsic density, doping dependent Shockley-Read-Hall generation/recombination and mobility, high field saturation, etc.) and default values for most parameters. However, the chosen minority carrier lifetimes are in ~ ms, which, are the typical values for FBK technology. Impact ionization effects are incorporated according to the avalanche model by Van Ovestraeten/De Man. The "Heavy Ion" model was used to release charge packets at different hit positions within the simulation domain with a uniform distribution along the vertical axis and a Gaussian distribution across the horizontal plane. Radiation damage effects in the silicon bulk are simulated using two deep-level trap models, i.e., the Perugia model [12] and the CERN model [13]. Both models are tuned for p-type silicon and use two acceptor trap levels and one donor trap level, with different values of the relevant parameters. The Perugia model has been validated at different temperatures (here we use room temperature) up to a fluence of 2.2×10^{16} n_{eq} cm^{-2}. The CERN model has been validated for a temperature range from -38.1 ºC to -31.1 ºC (here we use -37.9 ºC) up to a radiation fluence of 8×10^{15} n_{eq} cm^{-2}, but is here used beyond this limit.

Simulations start with a quasi-static analysis to save the different bias voltage conditions that are later fed as initial conditions for the transient analysis. The output of transient simulations provides current pulses at the read-out electrode as a function of time. The leakage current is subtracted from the current pulse and a numerical integration in the time domain is performed over 20 ns (compatible with LHC bunch-crossing), yielding the charge signal.

IV.4. Results

For the sake of conciseness, the analysis will be mainly focused on the 50×50-1E structure, but considerations that are more general will be drawn from the reported results and comparisons.

IV.4.1. The signal efficiency:

The signal efficiency as a function of reverse voltage at different hit points, simulated with the Perugia and the CERN models for the 50×50-1E pixel irradiated at 1×10^{16} n_{eq} cm^{-2} is shown in Figure IV.2. In both cases, data show different trends for different hit points. However, for all hit points the SE reaches high values as voltage is increased, with a smoother increase for the CERN model, and also exceeding 100% at high voltage due to charge multiplication effects.

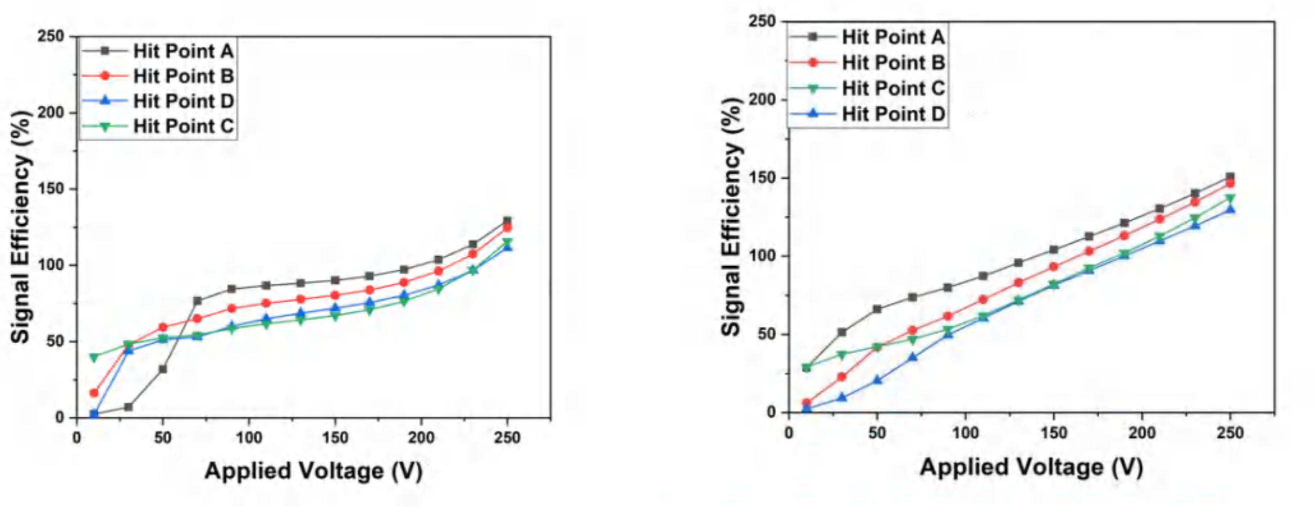

Figure IV.2: Simulated signal efficiency vs reverse voltage at different hit points for the 50×50-1E pixel irradiate at 1×10^{16} n_{eq} cm^{-2}: (left) Perugia model; (right) CERN model.

Figure IV.3 illustrates the signal efficiency as a function of reverse voltage at different hit points, simulated with the Perugia and the CERN model for the 50×50-1E pixel irradiated at 2×10^{16} n_{eq} cm^{-2}. There is a strong resemblance with the previous fluence. The data indicate various trends for various hit points. In addition, as voltage is increased, the SE approaches high values for all hit points, however, for the CERN model, the signal efficiency exceeds 100% at high voltage only at the point A, which is very close to the P-Column.

The other most striking observation to emerge from the data comparison is; at low voltages, very low signal efficiency is shown at the point A for Perugia model, this point is very close to Ohmic column. This phenomenon is less pronounced at the fluence of 1×10^{16} $n_{eq}.cm^{-2}$.

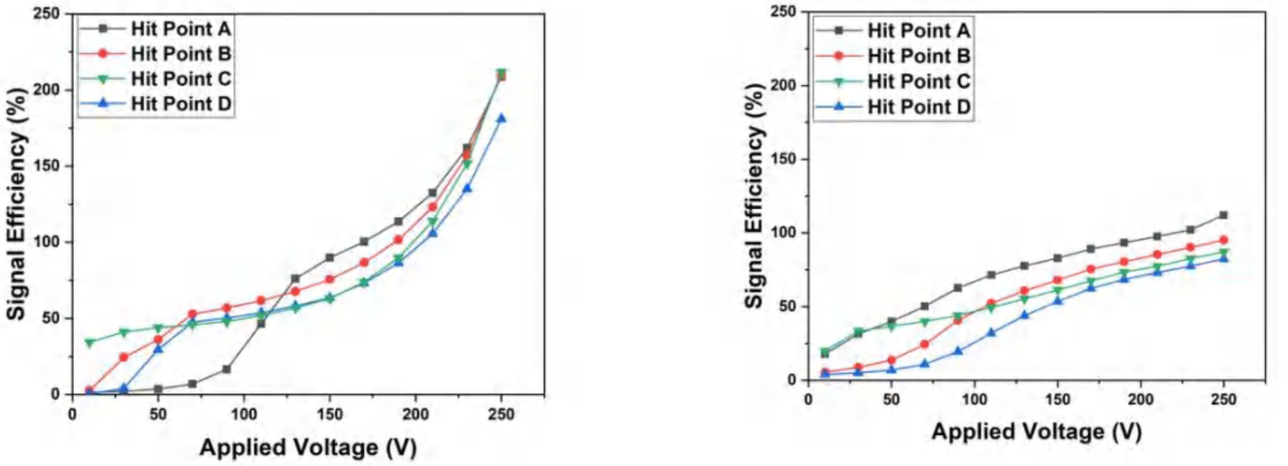

Figure IV.3: Simulated signal efficiency vs reverse voltage at different hit points for the 50×50-1E pixel irradiated at 2×10^{16} n_{eq} cm^{-2}*: (left) Perugia model; (right) CERN model.*

Figure IV.4 illustrates the signal efficiency as a function of reverse voltage at different hit points, simulated with the Perugia and the CERN model for the 100×25-1E pixel irradiated at 2×10^{16} n_{eq} cm^{-2}. The SE has a the same trend as the 50×50 structure in the CERN model case; various trends for various hit points with an increase in the SE until a reaching a maximum value, however, this time the latter is less than 70% for all the hitting points. This owing to the large inter-electrodes distance of 100×25-1E structure that leads to more trapping charge before reaching the readout electrode.

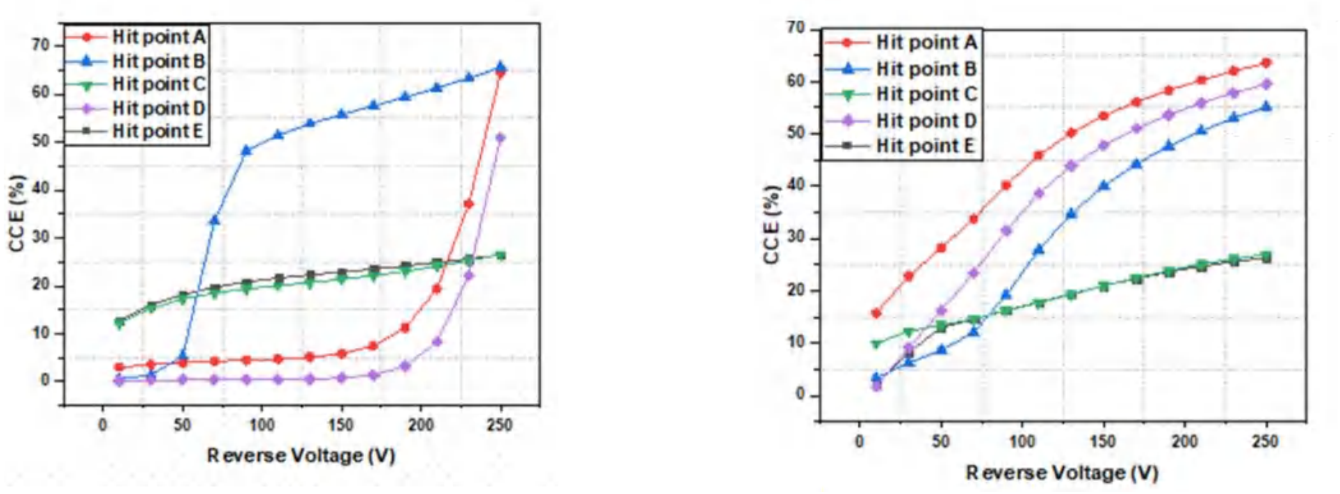

Figure IV.4: Simulated signal efficiency vs reverse voltage at different hit points for the 100×25-1E pixel irradiated at 2×10^{16} n_{eq} cm^{-2}: (left) Perugia model; (right) CERN model.

In contrary, the Perugia model shows strong position dependence, the points A and B has the smallest values of SE almost constant for all the applied voltages until the Vrev ≈ 200 V. However, similar to the CERN model, the maximum value is less than 70% for all the hitting points.

A comparison between simulation at some hitting points and the measurements obtained for the 50×50 structure at fluence of 2 × 10^{16} n_{eq}.cm^{-2} in [11] are presented in the up part of Figure IV.5. The 1D projections correspond to the measured signal efficiency at different applied voltages taken along cuts between the centers of readout column (left) and Ohmic column (right). Experimental Data are picked at the considered distances and plotted with simulations results for points A, B, and C in order to observe if the trend is correct and which is the best model choice in this aspect. In this figure, we present some position dependence comparisons. Figure IV.5.a reveals a correlation between simulation CERN results and experimental Data; the signal is larger at the side of the ohmic column and the agreement of CCE seems good. While, from Figure IV.5.b it can be clearly seen that Perugia model is confirmed to be less accurate; the correlation is good only between 125 and 200 V before attending the multiplication effect.

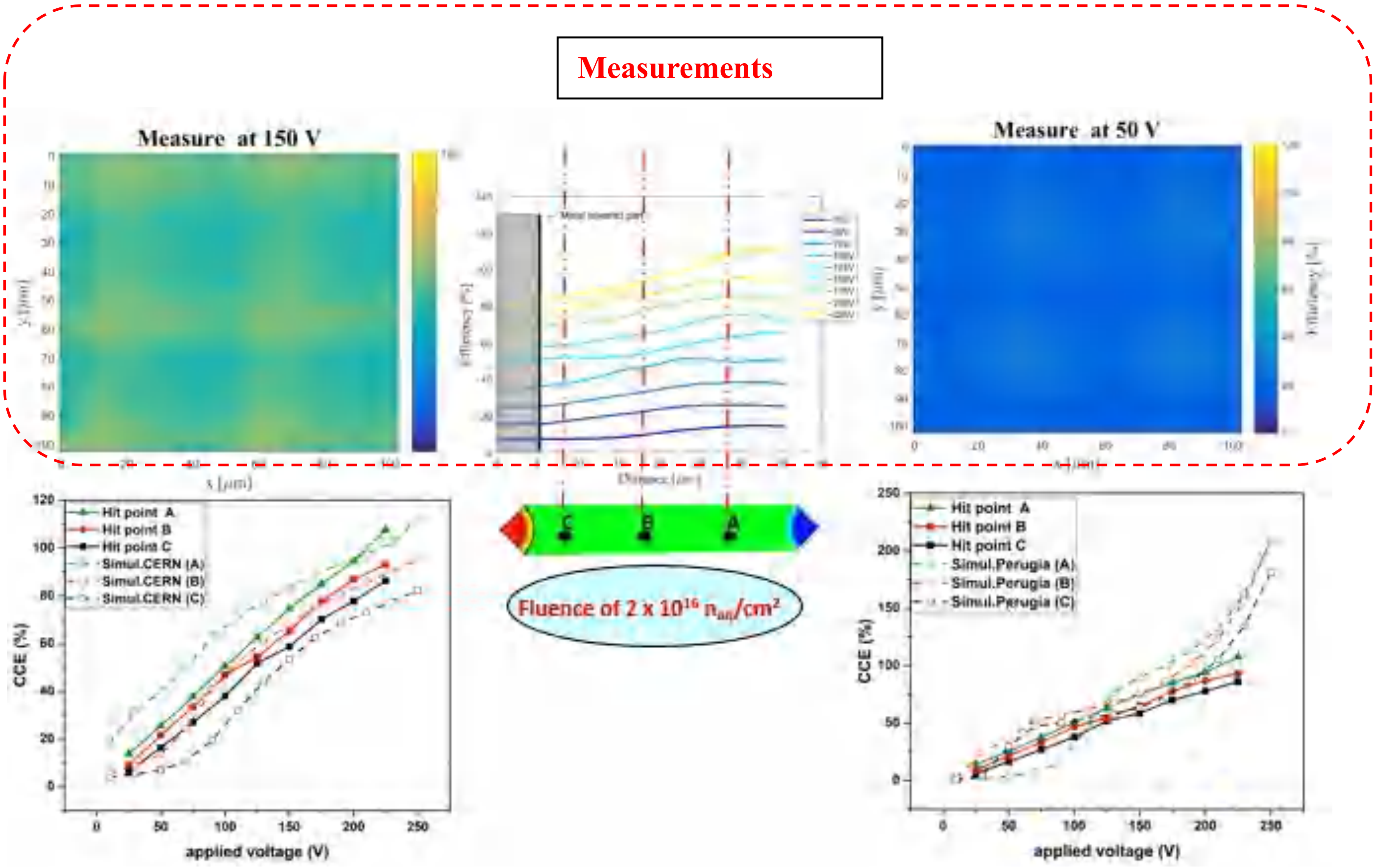

(a) **(b)**

Figure IV.5: Simulation CCE at the considered hitting points, with signal efficiency as a function of distance along a line connecting the center of a n+ column (0) to the center of a p+ column (~35 µm) at different bias voltages for 50×50-1E pixel (left) CERN model; (right) Perugia model. Results are compared to 3D diode of 50×50 type irradiated at fluence of 2 × 10^{16} $n_{eq}.cm^{-2}$ *from [11].*

To gain more insight into the outcome from the two models, Figure IV.6 compares the simulated SE at hit points A (close to the bias column) and C (close to the readout columns) to the experimental values measured on the same points from [11] for the 50×50-1E pixel irradiated at 2×10^{16} n_{eq} cm^{-2}. For hit point A, simulations using the CERN model slightly overestimate the measured SE, but the overall trend with voltage is similar. On the contrary, for the Perugia model, the SE is initially very low, and then increases abruptly as the voltage is increased, finally diverging due to charge multiplication effects. For hit point C, close to the readout column, simulations using the CERN model slightly underestimate the measured SE but show again a similar trend with voltage. On the contrary, for the Perugia model, the simulated SE initially increases more rapidly than the experimental one, reaching comparable values in the intermediate voltage range, before diverging due to charge multiplication effects.

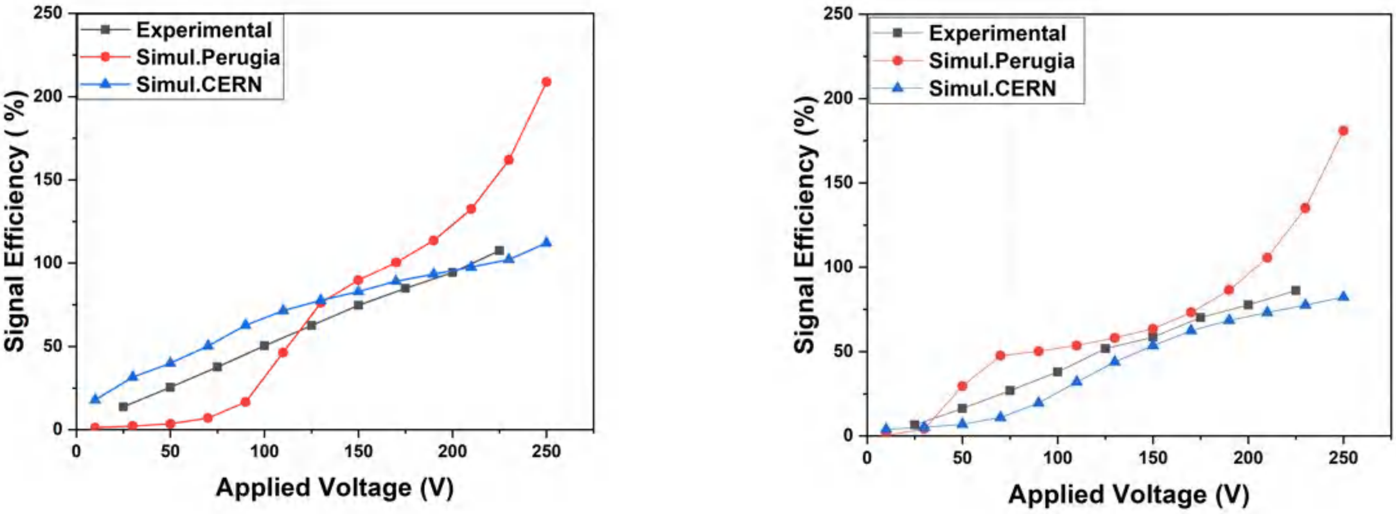

Figure IV.6: Simulated and experimental signal efficiency vs reverse voltage at different hit points for the 50×50-1E pixel irradiated at 2×10^{16} n_{eq} cm^{-2}: (left) hit point A; (right) hit point C.

Keeping into account the Ramo's theorem, and the fact that the weighting field in 3D sensors exhibits peaks close to both types of electrodes [16], the different trends in the simulated SE can be explained by the different electric field distributions obtained with the two models, that are shown in Figure IV.7 and Figure IV.*8* at reverse bias of 50 and 200 V, respectively.

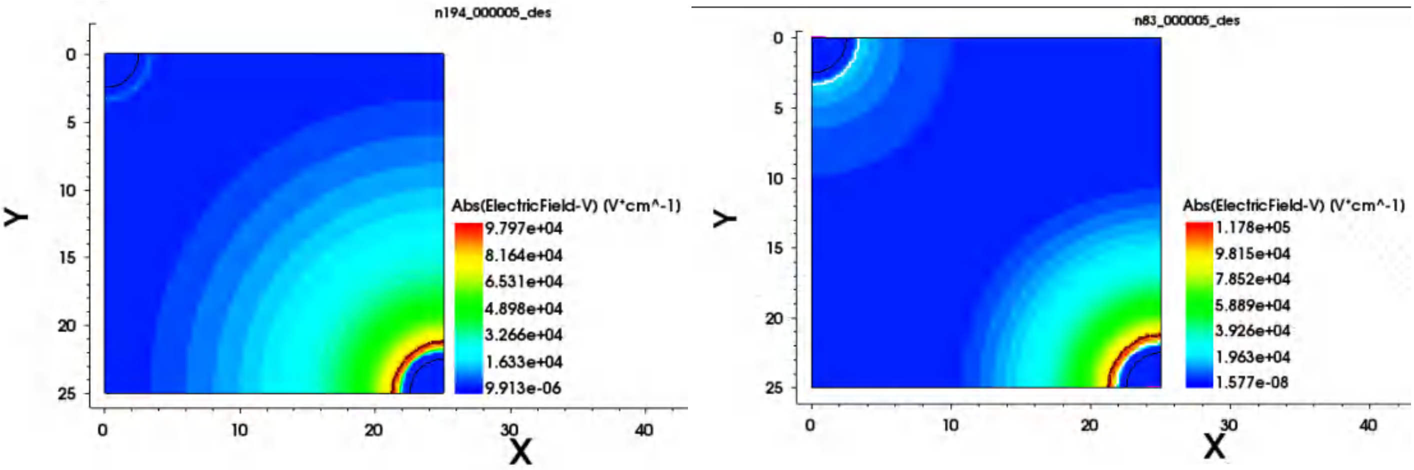

Figure IV.7: Two-dimensional maps of the electric field at 50 V reverse bias for the 50×50-1E pixel irradiated at 2×10^{16} n_{eq} cm^{-2}: (left) Perugia model; (right) CERN model.

At 50 V, the Perugia model predicts a wider depletion region spreading from the readout column, with no sign of an electric field peak at the bias column: this justifies the low SE at hit point A and the relatively high SE at hit point C, mainly due to the electron contribution to the signal. On the contrary, the CERN model shows a double peak of electric field at the two columns, with a narrower extension of the depletion region at the readout column, compatible with results observed at both points A and C, with a more balanced contribution to the signal from both electrons and holes. At 200 V, the electric field distributions are more similar, and the Perugia model also predicts a double peak of electric field, albeit less pronounced; however, the electric field intensity at the readout column is higher with the Perugia model, which can explain the greater impact of charge multiplication on the simulated SE.

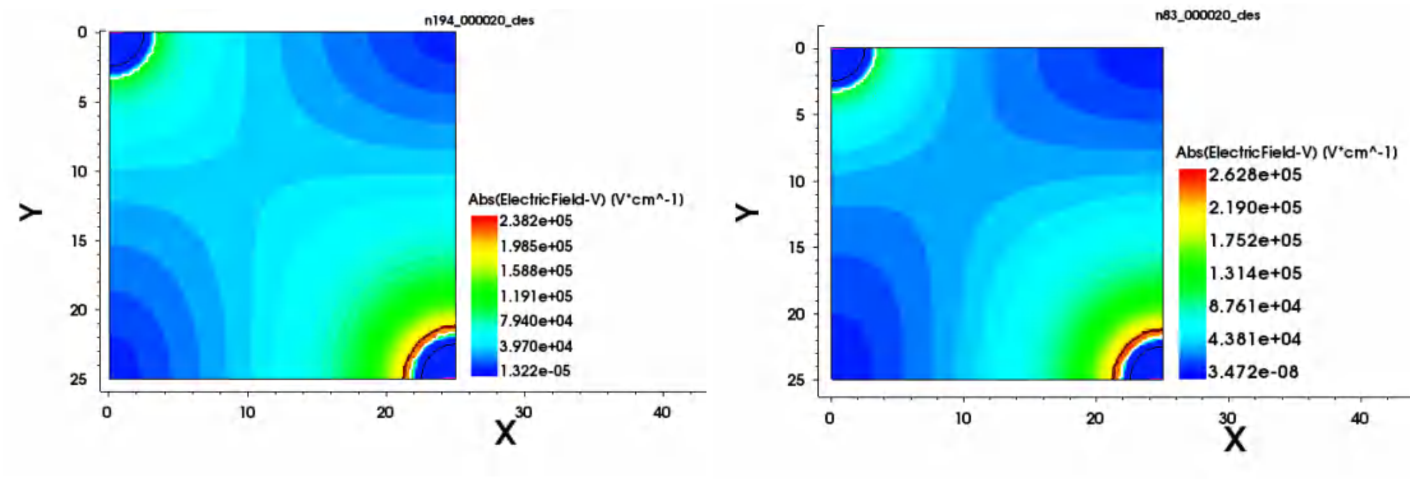

Figure IV.8: Two-dimensional maps of the electric field at 200 V reverse bias for the 50×50-1E pixel irradiate at 2×10^{16} n_{eq} cm^{-2}: (left) Perugia model; (right) CERN model.

Figure IV.9 compares the simulated SE at hit points A (close to the bias column) and C (close to the readout columns) to the experimental values measured on the same points from [11] for the 100×25-1E pixel irradiated at 2×10^{16} n_{eq} cm^{-2}.

Figure IV.10 displays the electric field for the (100 µm × 25 µm.1E) structure at applied voltage of 200 V for the two models, pixel irradiated at 2×10^{16} n_{eq} cm^{-2}. There is unexpected result from these maps, different electric field distribution are shown around the Ohmic column, where CERN model shows again an electric field peak , while Perugia model does not, in addition the Perugia model shows wider deletion region spreading from the readout column. These various maps can explain the different trend in the simulated SE in Figure IV.9. For the Perugia model, the SE is low at hitting point A and comparatively large at hit point C, owing to the electron contribution to the signal. On the other hand, the SE for the CERN model at hit point A relatively high than the SE at the hit point C, indicating, this time a more contribution to the signal from the hole. It is clearly noted also that the SE for both hit points is low compared to the (50µm × 50 µm.1E) structure; this is mainly due to the large inter-electrode distance.

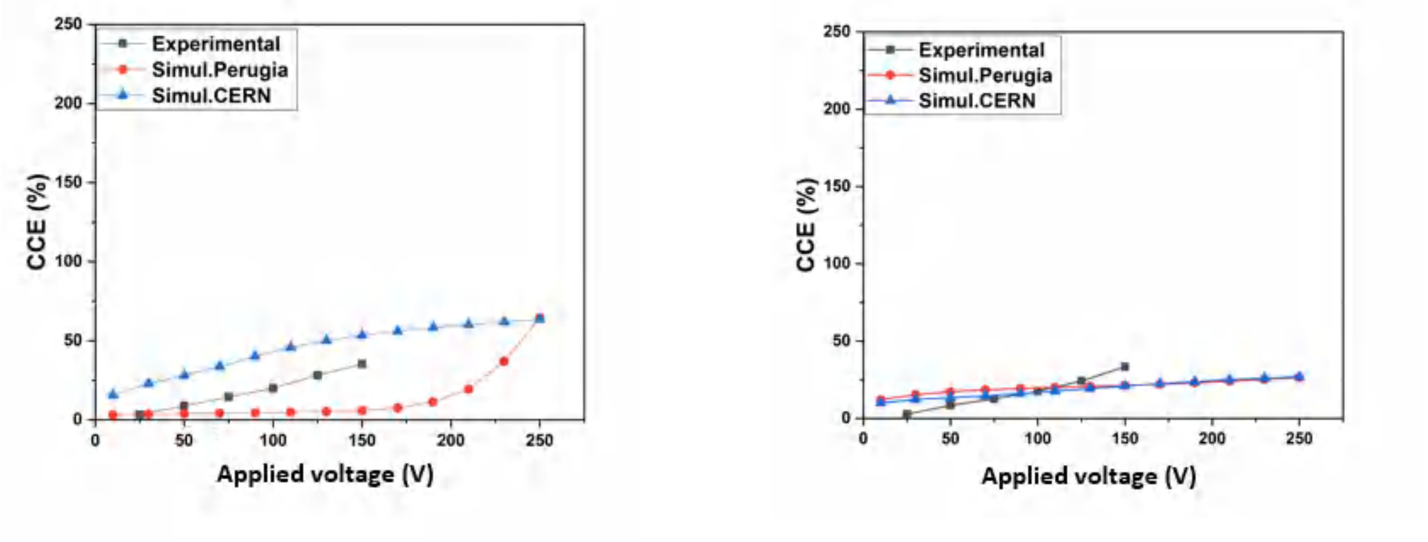

Figure IV.9: Simulated and experimental signal efficiency vs reverse voltage at different hit points for the 100×25-1E pixel irradiated at 2×10^{16} n$_{eq}$ cm^{-2}: (left) hit point A; (right) hit point C.

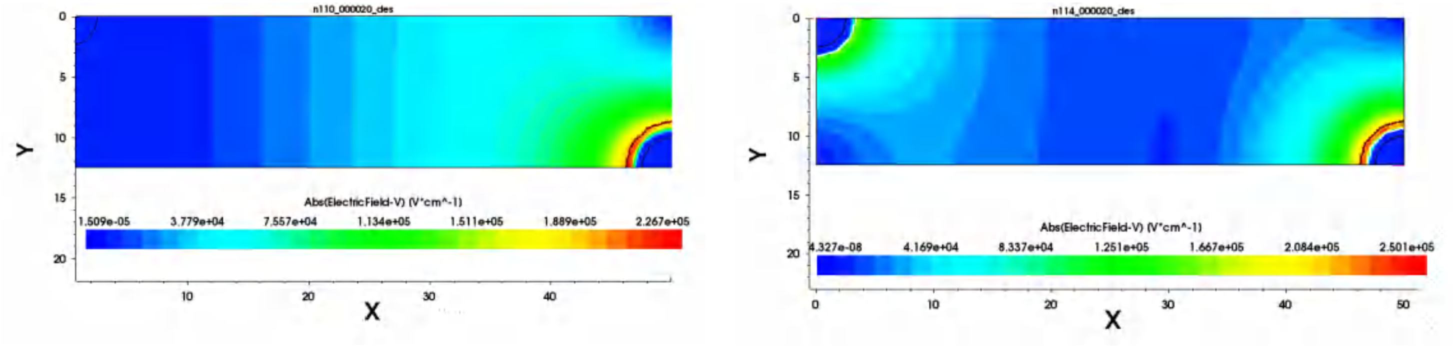

Figure IV.10: Two-dimensional maps of the electric field at 200 V reverse bias for the 100×25-1E pixel irradiated at 2×10^{16} n$_{eq}$ cm^{-2}: (left) Perugia model; (right) CERN model.

Figure IV.11 shows the simulated CCE for 50×50 µm^2 geometry for both models in comparison to experimental data of 3D diodes. These diodes are irradiated with reactor neutrons at three different fluences 1×10^{16} n$_{eq}$ cm^{-2}, 2×10^{16} n$_{eq}$ cm^{-2}, 3.5×10^{16} n$_{eq}$ cm^{-2}[7].

On one hand, when the Avalanche model is activated, simulation using Perugia model does not fit the experimental data. The CERN model is able to predict the onset of charge multiplication effects observed in the measurements of sensors with the smaller inter-electrode distances at high voltage. On the other hand, when the Avalanche model is OFF, no significant difference between the two considered models trend before and during the saturation. By increasing the fluence until at a value of 2×10^{16} $n_{eq}.cm^{-2}$, the simulation results becomes more correlate if the Avalanche is ON, until Vrev ≈ 200 V, where Perugia model over-estimates the multiplication effect. The most surprising aspect of the data is in the smaller CCE values for CERN model when the Avalanche is OFF.

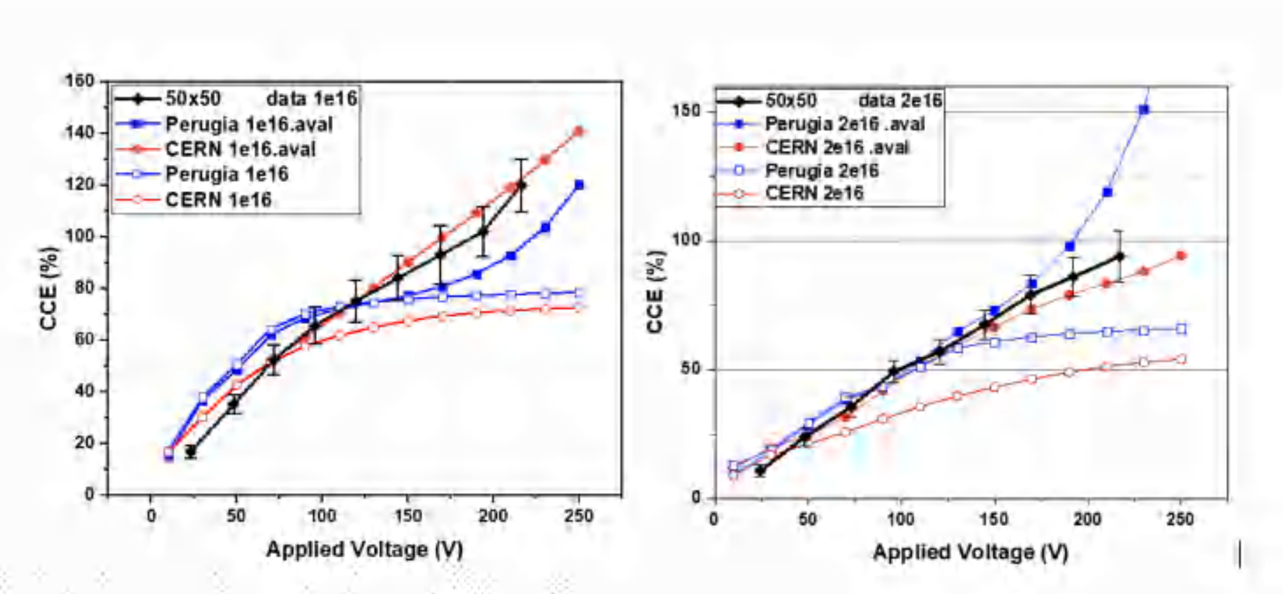

Figure IV.11: Experimental and simulated Charge Collection Efficiency (CCE) for different model vs reverse voltage in 3D diodes of 50×50 μm^2 geometries irradiated with neutrons at 1×10^{16} n_{eq} cm^{-2} and 2×10^{16} n_{eq} cm^{-2}.

Figure IV.12 and Figure IV.13 compare the simulated SE to the experimental values from [11] for all the pixel geometries irradiated at 1×10^{16} n_{eq} $cm^{-2}$and 2×10^{16} n_{eq} cm^{-2}, respectively. The experimental data represent the average of the values measured along the diagonal connecting the centers of bias and readout columns, excluding the regions covered by metal, whereas the error bars are the standard deviations. The simulated values represent the average between hit points A, B, and C. At 1×10^{16} n_{eq} cm^{-2} the agreement between simulations and measurements is good enough for the 50×50-1E structure, whereas simulations underestimate the signal efficiency for the 25×100-2E structure (note that experimental data are not available at this fluence for the 25×100-1E geometry). At 2×10^{16} n_{eq} cm^{-2} , the agreement between simulations and measurements is better for both Perugia and CERN models for all geometries, at least up to ~150 V. At larger voltage, the agreement is still acceptable with the CERN model, whereas larger deviations are observed with the Perugia model.

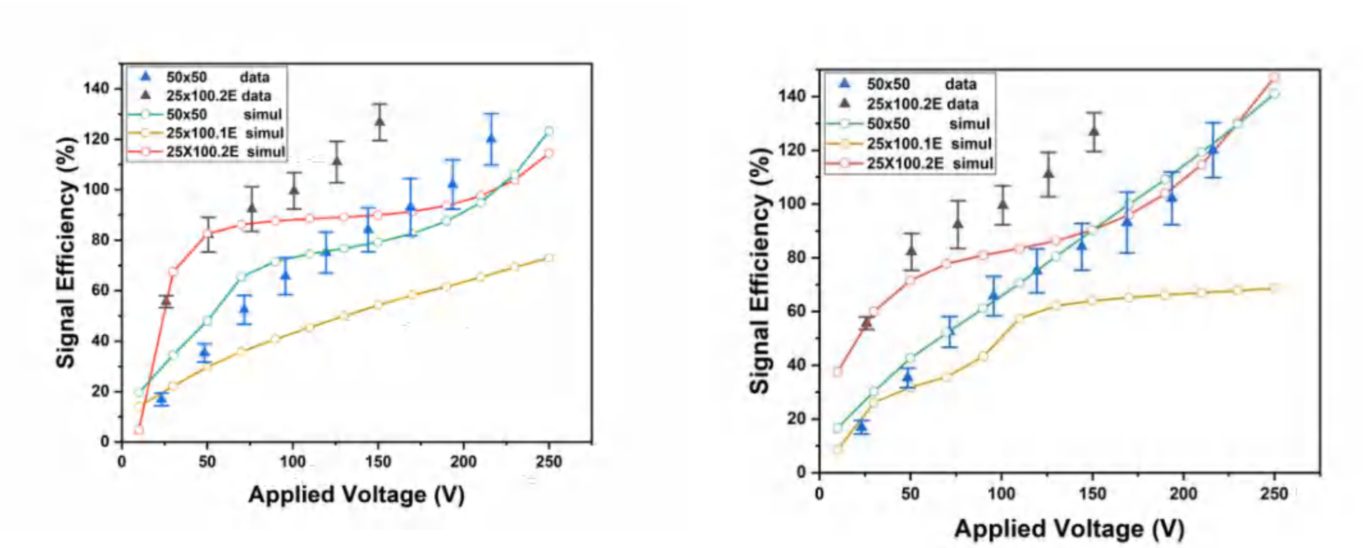

Figure IV.12: Average signal efficiency vs reverse voltage for all pixel geometries irradiated at 1×10^{16} n_{eq} cm^{-2}: (left) Perugia model; (right) CERN model.

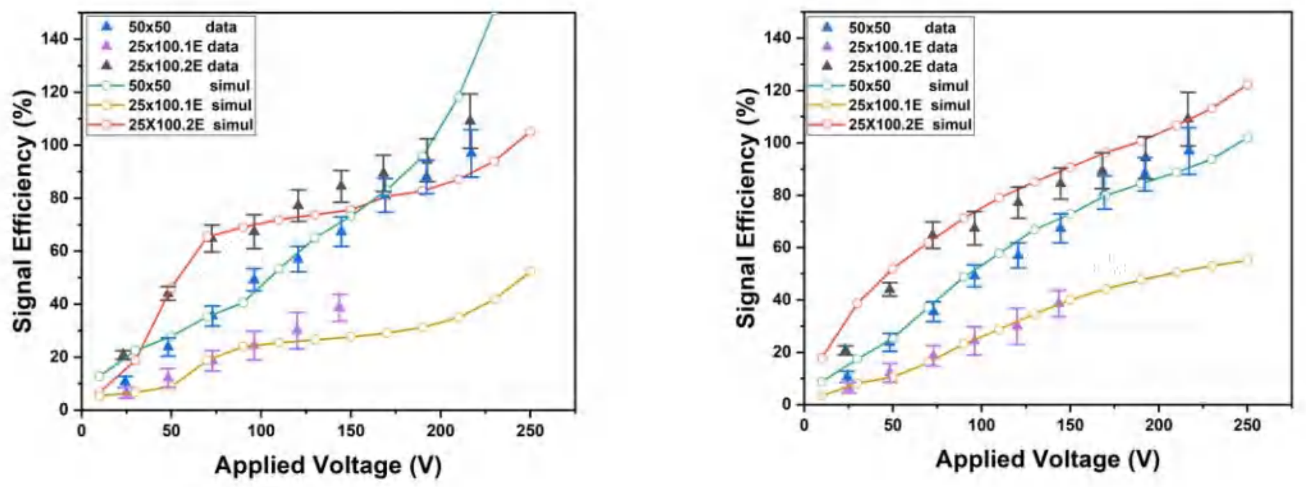

Figure IV.13: Average signal efficiency vs reverse voltage for all pixel geometries irradiated at 2×10^{16} n_{eq} cm^{-2}: (left) Perugia model; (right) CERN model.

In general, the larger discrepancies between simulations and measurements appear at large voltage, when charge multiplication effects play a major role. In this respect, it should be noted that both the junction between the readout columns and the p-spray implant close to the front-side surface, and the readout column tips can experience high electric field peaks [17], so the simplified quasi-2D domain here used is not entirely adequate. Moreover, simulations are performed at the temperatures for which the radiation damage models were validated, that differ from the temperature at which the measurements were performed (-10 ºC [11]), so that the impact ionization coefficients can be affected.

Figure IV.14 shows the simulated SE at ~100 V (i.e., below the onset of charge multiplication) as a function of the fluence within an extended range from 2×10^{15} n_{eq} cm^{-2} to 2.25×10^{16} n_{eq} cm^{-2} for the three considered structures. As expected from geometrical consideration, the SE values decrease as the inter-electrode distance is increased. The fitting curves of simulated data according to the theoretical model of Equation IV 1 are also shown in Figure IV.14 [4]:

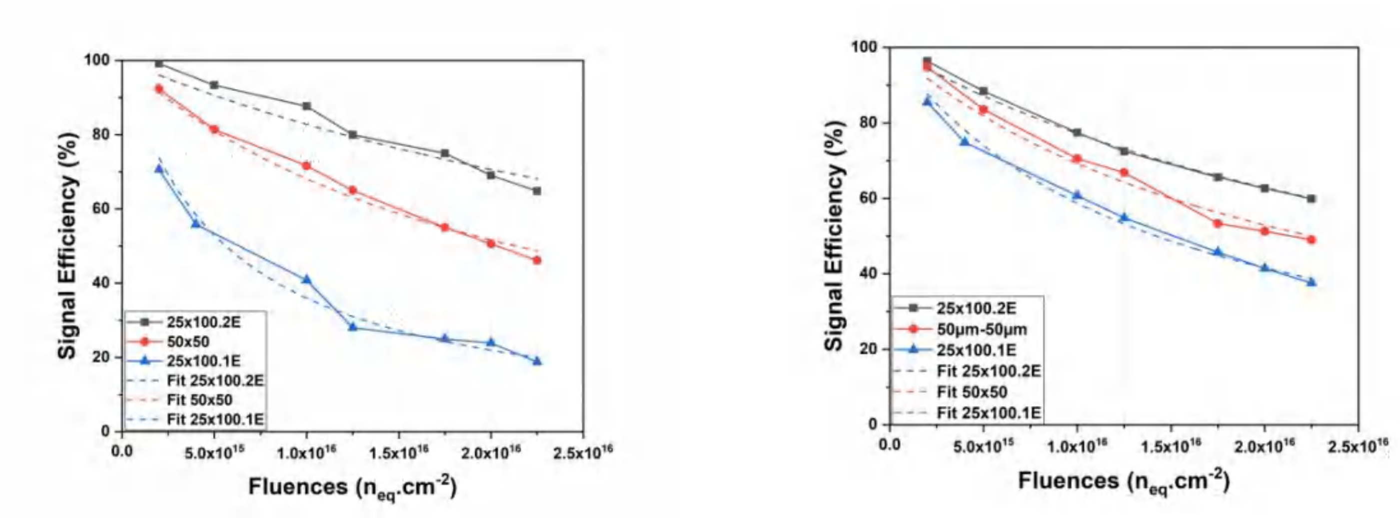

Figure IV.14: Average signal efficiency vs fluence for all pixel geometries with fits according to the geometrical model of [4]: (left) Perugia model; (right) CERN model.

$$\boldsymbol{SE = \frac{1}{1+K_c\varphi} = \frac{1}{1+0.6\, L\, K_L\varphi}} \qquad \textbf{IV-1}$$

Where K_c and $K_L$are damage parameters, L is the inter-electrode distance, and φ is the fluence. The values of L and the best-fit values of K_c and $K_L$are reported in Figure IV.3.

Table IV-3 shows the best-fit values of damage parameters $\boldsymbol{K_c}$ and $\boldsymbol{K_L}$ for the different pixel structures. It can be seen from Figure IV.14 and Table IV-3 that the two models yield comparable values for the 50×50-1E structure, whereas more significant differences are found for the other geometries, especially for the 25×100-1E. In this respect, the spread in the values of K_L (that should ideally be a constant in case charge carriers reach saturation velocity [4]) is limited for the CERN model, whereas it is much wider for the Perugia model, which seems to overestimate the dependence of radiation hardness on the inter-electrode distance.

Table IV-3: Best-fit values of damage parameters $\boldsymbol{K_c}$ *and* $\boldsymbol{K_L}$ *for the different pixel structures*

	Model	**Perugia**		**CERN**	
Structures	L (µm)	K_c (10^{-16} cm^2)	K_L (10^{-14} cm)	K_c (10^{-16} cm^2)	K_L (10^{-14} cm)
25×100-1E	51.5	1.777 ± 0.132	5.75 ± 0.43	0.702 ± 0.021	2.27 ± 0.07
50×50-1E	35.4	0.468 ± 0.024	2.20 ± 0.11	0.448 ± 0.018	2.11 ± 0.08
25×100-2E	28.0	0.208 ± 0.022	1.24 ± 0.13	0.295 ± 0.006	1.76 ± 0.04

Since the CERN has been shown more accuracy of collected charges at the high fluences, it is used to estimate the CCE for the three fluences up to a fluence of 3.5×10^{16} n_{eq}.cm^{-2}, which seems vigorous challenge for this model. Simulation results are shows in comparison with experimental data of 3D diodes irradiated with reactor neutrons at the same fluence [7]. Figure IV.15 confirms that the latter model yield a good agreement with those obtained in the measurements, correctly predicting also the charge multiplication effects observed in the measurements at high voltage.

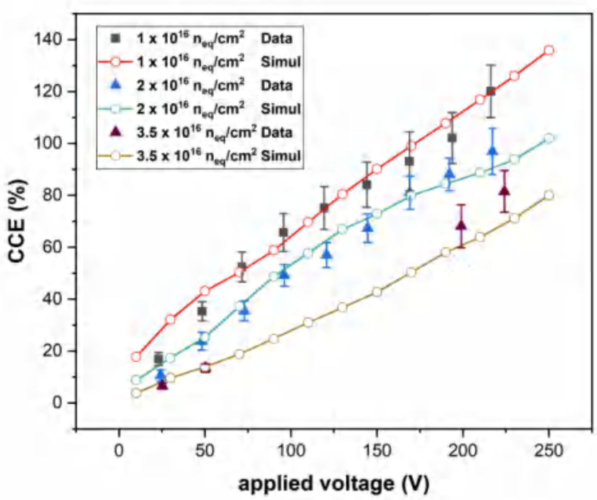

Figure IV.15: Experimental and simulated Charge Collection Efficiency (CCE) vs reverse voltage in 3D diodes of 50×50 µm2 geometries irradiated with neutrons at different fluences.

IV.4.2. I-V Characteristics:

The increase of the leakage current after exposure is linearly proportional to the irradiation fluence following the relationship:

$$\Delta I = \alpha . \varphi_{eq} . V \qquad \textit{IV-2}$$

Where α is the current-related damage parameter, Φ_{eq} the 1 MeV neutron equivalent fluence, and V the total depleted sensor volume.

Because leakage current is substantially temperature sensitive, all measurements are typically scaled to the same reference temperature, often 20°C, where the value of the damage parameter tends to be = (3.9 ± 0.03) 10^{-17} A/ cm [1].

In order to compare the accuracy of models in predicting the leakage current, experimental results are achieved with measurements on four FBK diodes irradiated in Ljubljana to a fluence of 1.0 × 10^{16} n_{eq}.cm^{-2}. As expected, the measurement results were in good agreement with CNM diodes [18]. Figure IV.16 shows the measured and simulated curves for: a) 50×50 μm^2, b) 100×25 μm^2 .1E. The simulations results are normalized by means of the Chilingarov formula [19] to -25 ºC the temperature in which the measurement were done.

$$I(T) = I(T_R).(\frac{T}{T_R})^2 exp\left[\frac{E}{2k_b}.\left(\frac{1}{T_R} - \frac{1}{T}\right)\right] \qquad \text{IV-3}$$

Where E = 1.21 eV is the effective band-gap energy, k_B is Boltzmann's constant and T_R is the reference temperature.

A first insight at the plots reveals that no significant correlation can be found between the I-V curves simulated with Perugia model and the experimental results, however, the ones simulated with CERN model are in better agreement with those observed in the sensors measurements.

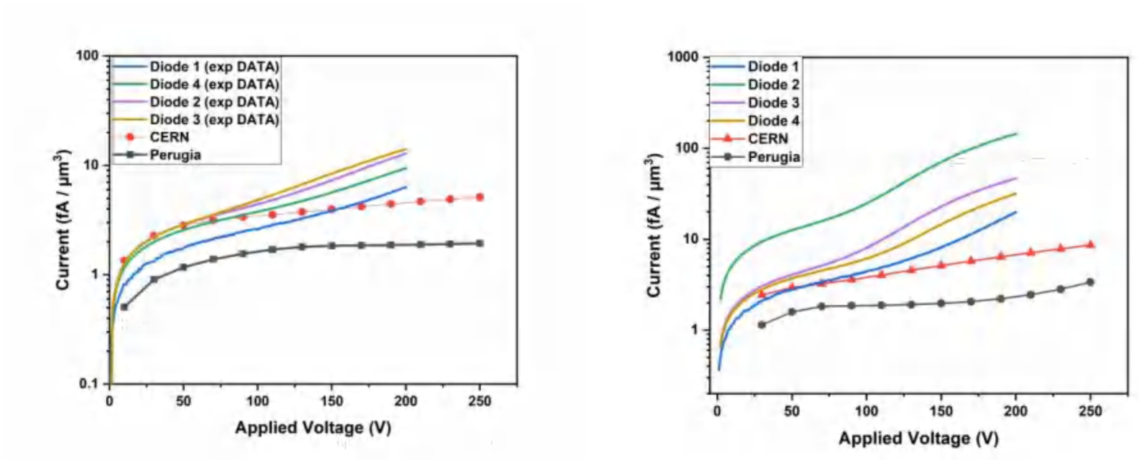

Figure IV.16: Simulated curves for: (left) 50×50 μm^2 , (right) 100×25 μm^2 .1E using both radiation bulk models in comparison with the experimental results achieved with measurements of FBK diodes irradiated in Ljubljana at a fluence of 1×10^{16} $n_{eq}.cm^{-2}$.

Figure IV.17 shows simulated curves for: a) 50×50 μm^2, b) 100×25 μm^2.1E using both radiation bulk models in comparison with the experimental results achieved with measurements of FBK diodes irradiated in Ljubljana at a fluence of 1.5×10^{16} $n_{eq}.cm^{-2.}$ The simulations results are normalized also by the same means of the Chilingarov formula to -25 ºC, the temperature in which the measurement were done. These results confirms that the Perugia model showing less accuracy in prediction of the leakage current with respect to the CERN one. It is clearly seen that the 100×25 μm^2 showing lower current, which lead to a smaller power dissipation at the same voltage.

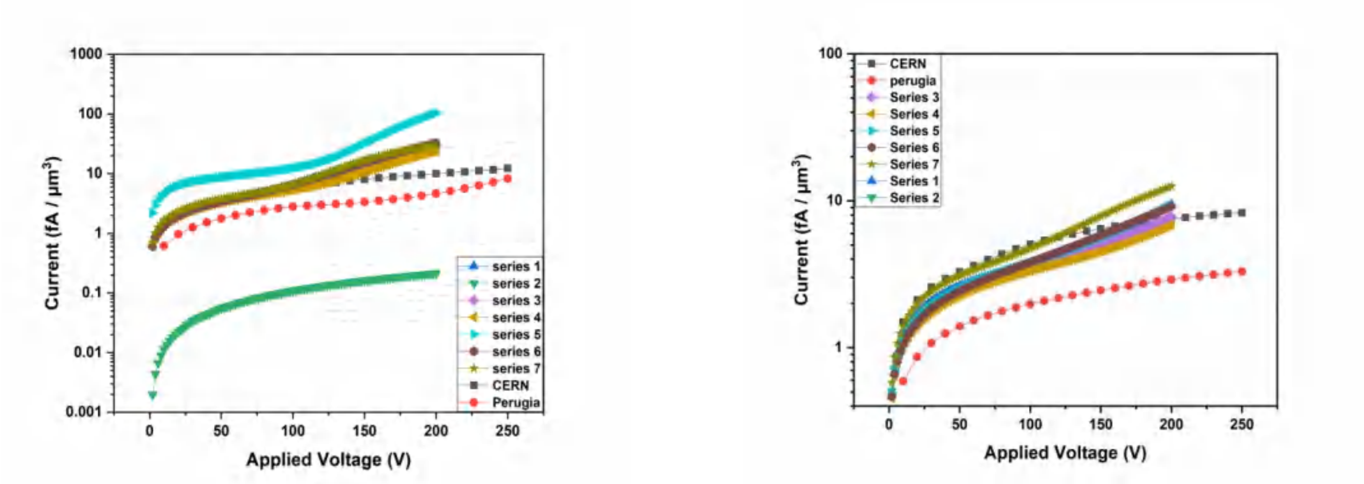

Figure IV.17: simulated curves for: (left) 50×50 μm^2 , (right) 100×25 μm^2 .1E using both radiation bulk models in comparison with the experimental results achieved with measurements of FBK diodes irradiated in Ljubljana at a fluence of 1.5×10^{16} $n_{eq}.cm^{-2}$.

In order to compare the experimental and the simulations current-related damage parameter α with the theoretical one, all the leakage currents are scaled to the same reference temperature 20°C. Results are summarized in Figure IV.4. It can be seen from its data that both models predict the good values current-related damage parameter (in the order of 10^{-17}). While α from the CERN model is very close to the theoretical one ($\alpha = (3.99 \pm 0.03) \times 10^{-17}$ A/ cm) at fluence of 1 × 1016 neq.cm-2, the Perugia model has a better agreement for the other fluence (1.5×10^{16} $n_{eq}.cm^{-2}$).

Table IV-4: Best-fit values of damage parameters Kc and KL for the different pixel structures.

Structure	**Fluence ($n_{eq}.cm^{-2}$)**		**Fluence ($n_{eq}.cm^{-2}$)**	
	1×10^{16}	**1×10^{16}**	**1.5×10^{16}**	**1.5×10^{16}**
	Perugia (A/ cm)	**CERN (A/ cm)**	**Perugia (A/ cm)**	**CERN (A/ cm)**
50×50-1E (α)	**1.96×10^{-17}**	**3.66×10^{-17}**	**2.95×10^{-17}**	**5.58×10^{-17}**
100×25-1E (α)	**1.9×10^{-17}**	**3.83×10^{-17}**	**2.95×10^{-17}**	**$5 .24 \times 10^{-17}$**

IV.5. Collaboration with Perugia for 3D detectors:

A collaboration with the University of Perugia to extend the combined bulk + surface radiation damage modeling scheme, which is published in [20] is presented in [21]. The goal is reproducing the macroscopic behavior of 3D detectors. The updated model was validated on basis of measurement performed on simple structures (e.g. PiN diodes,) in order to better understand the effects of the radiation damage on the device. At the beginning, it seemed that there are some neglecting effects, which make the I-V plots almost the same as the last Perugia radiation model [12].

In addition to the modeling scheme with three traps, some physical parameters depending on the irradiated fluence (acceptor creation mechanism) is considered; this allows obtaining more realistic results in terms of static and dynamic behavior for PiN and LGAD devices. This simulation methodology is confirmed to be advantageous for 3D devices. From Figure IV.18 it seems that the model is able to reproduce the double junction effect. The Two-dimensional maps of the electric field are presented in this figure for the 50×50-1E pixel irradiated at 2 × 10^{16} n_{eq}.cm^{-2}: (left) 50 V; (right) 200 V using the updated Perugia model.From these maps we can note that the updated Perugia model is able to reproduce the double junction effect.

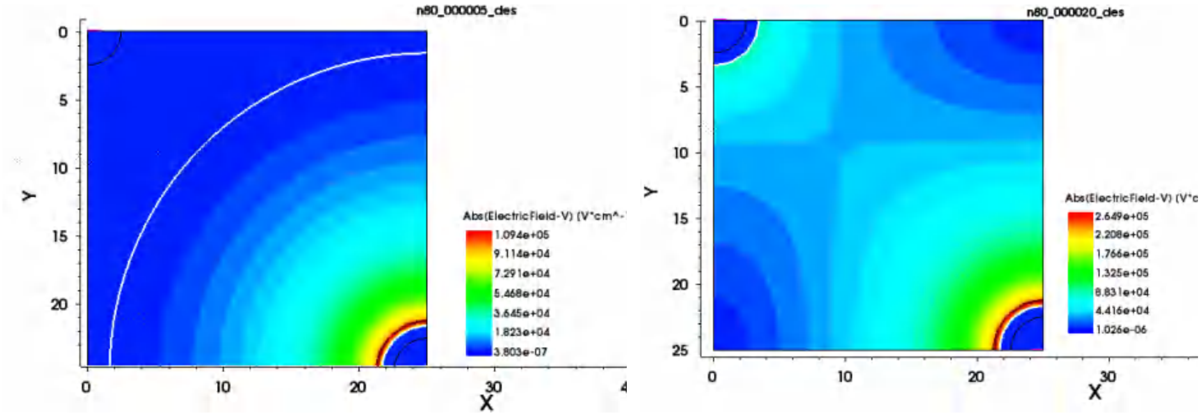

Figure IV.18: Two-dimensional maps of the electric field for the 50×50-1E pixel irradiated at 2 × 10^{16} n_{eq}.cm^{-2}: (left) 50 V, (right) 200 V using the updated Perugia model.

Figure IV.19 shows the I-V curves simulated with the updated Perugia model at fluence 1× 10^{16} n_{eq}/cm^{-2} for the 100 × 25 μm^2. They are compared to the previous experimental results of the four diodes and the the CERN model. The updated Perugia model is more accurate than the CERN one. Thus, the model is very promising for 3D and the LGAD detectors at coming high fluences.

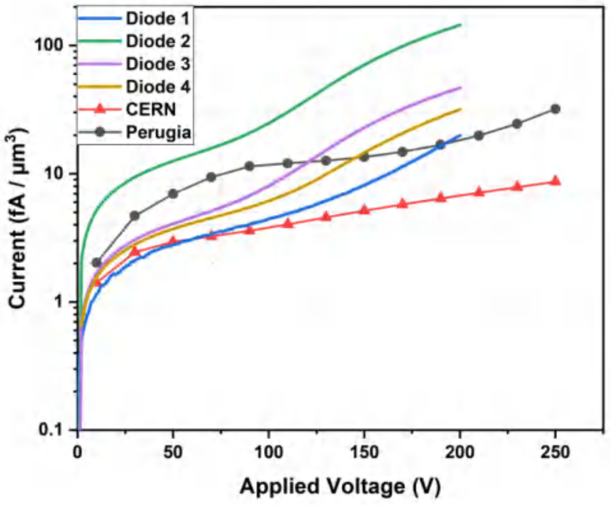

Figure IV.19: Simulated curves for:) 100×25 μm^2 .1E using both radiation bulk models in comparison with the experimental results achieved with measurements of FBK diodes irradiated in Ljubljana at a fluence of 1 × 10^{16} n_{eq}.cm^{-2}

IV.6. Conclusion

In this chapter we have reported a TCAD simulation study relevant to the signal efficiency and I-V characteristic of small-pitch 3D sensors of different geometries fabricated at FBK and irradiated at large fluences up to the maximum value foreseen at the innermost pixel layers at HL-LHC (2×10^{16} n_{eq} cm^{-2}). Simulations have been performed using a simplified quasi-2D domain, corresponding to a horizontal slice, 1-µm thick, taken at half the depth of the structures. Results based on two bulk damage models were analyzed, in comparison with experimental data from 3D diodes measured with a position resolved laser system. Despite both models were validated against data from planar sensors, here they predict leakage currents, signal efficiency values and charge multiplication effects at high voltage that are compatible with the experimental observations. Due to the different distributions of the electric field, and particularly to the presence/intensity of the double peak, the two models yield a different evolution of the signal efficiency with bias voltage at different hit points, that is found in better agreement with measurements in case of the CERN model. For both models, simulations show the largest deviations from measurements at high voltage, beyond the onset of charge multiplication. To better investigate this aspect, we plan to further extend this study using a full 3D simulation domain, including those regions that can play a critical role for high field effects.

IV.7. References

[1] C. Da Via, G.-F. Dalla Betta, and S. Parker, Radiation sensors with three-dimensional electrodes, CRC Press, Boca Raton, U.S.A., 2019.

[2] C. Da Via et al., 3D Silicon Sensors: Design, Large Area Production and Quality Assurance for the ATLAS IBL Pixel Detector Upgrade, Nucl. Instrum. Meth. A 694 (2012) 321.

[3] M. Garcia-Sc4eres, J. Christiansen, Development of pixel readout integrated circuits for extreme rate and radiation, CERN LHCC 2013 002, LHCC I 024.http://rd53.web.cern.ch/RD53

[4] C. Da Vià, S.J. Watts, The geometrical dependence of radiation hardness in planar and 3D silicon detectors, Nucl. Instrum. Meth. A 603 (2009) 319.

[5] G.-F. Dalla Betta et al, Development of a new generation of 3D pixel sensors for HL-LHC, Nucl. Instrum. Meth. A 824 (2016) 386.

[6] D M S Sultan et al., First production of new thin 3D sensors for HL-LHC at FBK, JINST 12 (2017) C01022.

[7] M. Boscardin et al., Advances in 3D Sensor Technology by Using Stepper Lithography, Frontiers in Physics - Radiation Detection and Imaging 8 (2021) 625275.

[8] H. Oide et al., INFN-FBK developments of 3D sensors for High-Luminosity LHC, Nucl. Instrum. Meth. A 924 (2019) 73.

[9] M. Boscardin et al., Performance of new radiation-tolerant thin planar and 3D columnar n+ on p silicon pixel sensors up to a maximum fluence of ~5×1015 n$_{eq}$/cm^2, Nucl. Instrum. Meth. A 953 (2020) 163222.

[10] S. Terzo et al., Novel 3D pixel sensors for the upgrade of the ATLAS Inner Tracker, Frontiers in Physics - Radiation Detection and Imaging 8 (2021) 624668.

[11] R. Mendicino et al., Characterization of FBK small-pitch 3D diodes after neutron irradiation up to 3.5×1016 neq cm−2, JINST 14 (2019) C01005.

[12] F. Moscatelli et al., Combined Bulk and Surface Radiation Damage Effects at Very High Fluences in Silicon Detectors: Measurements and TCAD Simulations,IEEE Trans. Nucl. Sci. 63 (2016) 2716.

[13] Å. Folkestad et al., Development of a silicon bulk radiation damage model for Sentaurus TCAD, Nucl. Instrum. Meth. A 874 (2017) 94.

[14] G.-F. Dalla Betta et al., Development of new 3D pixel sensors for phase 2 upgrades at LHC, IEEE NSS/MIC Conference Record, San Diego, USA (2015) N3C3-5.

[15] A. Boughedda et al., TCAD simulation of small-pitch 3D sensors for pixel detector upgrades at High Luminosity LHC, J. Phys.: Conf. Ser. 1766 (2021) 012014.

[16] M. Koehler et al., Comparat4e measurements of highly irradiated n-in-p and p-in-n 3D silicon strip detectors, Nucl. Instrum. Meth. A 659 (2011) 272.

[17] G.-F. Dalla Betta et al, Electrical characterization of FBK small-pitch 3D sensors after ɤ-ray, neutron and proton irradiations, JINST 12 (2017) C11028.

[18]] A. Lapertosa et al., “Performance of irradiated FBK 3D sensors for the ATLAS ITk pixel detector”, 16th Trento Workshop on Advanced Silicon Radiation Detectors, Feb. 2021

[19] A. Chilingarov, Temperature dependence of the current generated in Si bulk, 2013 JINST 8 P10003.

[20] Morozzi, Arianna, et al. "TCAD advanced radiation damage modeling in silicon detectors." The 28th International Workshop on Vertex Detectors. 13-18 October. 2019.

[21] F. Moscatelli et al " Simulations of radiation hard detectors for timing applications" AIDAInnova WP6 Meeting,Septempbre.2021

Conclusions and perspectives

Conclusions and perspectives

This PhD dissertation has reported on a TCAD simulation of silicon radiation detectors, in particular the active-edge planar radiation detectors , which are very appealing for X-ray imaging applications at free-electron laser facilities, due to reduce dead area and the larger breakdown voltage. These detectors are built on hybrid multilayer tiles made of active-edge high resistivity pixel sensors bump-bonded to two-tiered 65-nm CMOS front-end ICs.

We have presented a new compact border termination for active-edge planar radiation detectors. As compared to an existing design with four guard rings, owing to the use of slant field plates, the proposed design with two guard rings yields almost the same minimum breakdown voltage with an overall size smaller by ~ 60 µm, whereas that with three guard rings offers both a 100 V increase of the minimum breakdown voltage and an overall size decrease by ~30 µm. These characteristics make the proposed terminations appealing for X-ray imaging applications at FEL facilities, with a minor increase in the fabrication process complexity coming from the use of greytone lithography to tailor the slope of the side-wall oxide layer in the field plate regions. We plan to experimentally validate this approach in a batch of test diodes at FBK in the next year.

The other considered detectors in this PhD dissertation are the small pitch 3D sensors of different geometries fabricated at FBK and irradiated at large fluences up to the maximum value foreseen at the innermost pixel layers at HL-LHC (2×10^{16} n_{eq} cm^{-2}). The pixel sizes are 50×50 µm^2 with 1 readout column, and 25×100 µm^2 with 1 or 2 readout columns (1E and 2E). Owing to the small inter-electrode distance, ranging from ~28 µm to ~51 µm in the considered layouts, these devices are expected to be extremely radiation hard. Since 2013, in the framework of an R&D program funded by INFN, several batches of small-pitch 3D sensors aimed at the ATLAS and CMS upgrades were fabricated at FBK using a single-sided technology on Si-Si direct wafer bonded 6” substrates. Pixel sensors compatible with different read-out chips (ATLASFEI4, CMS PSI46dig, and RD53A) were tested under particle beams before and after irradiation, showing a very high hit efficiency of ~97 % after an irradiation fluence of 1×10^{16} n_{eq} cm^{-2}. Further tests aimed at assessing the performance up to the ~2× larger fluences of interest for the HL-LHC experiments are under way. The radiation hardness of FBK small-pitch 3D sensors irradiated up to extremely large fluences has so far been measured on test structures: the results of position resolved laser tests performed on 3D diodes of various geometries after neutron irradiation up to 3.5 × 10^{16} n_{eq} cm^{-2} are showing very high signal efficiency, also boosted by charge multiplication effects.

We have performed Simulations using a simplified quasi-2D domain, corresponding to a horizontal slice, 1 µm thick, taken at half the depth of the structures. We have analyzed results based on two bulk damage models in comparison with the previous experimental data. Despite both models were validated against data from planar sensors, they predict signal efficiency values and charge multiplication effects at high voltage that are compatible with the experimental observations. In addition, we have tested the accuracy of models in predicting the leakage currents. Experimental results are achieved with measurements on four FBK diodes irradiated in Ljubljana to a fluence of 1.0 x 10^{16} $n_{eq}.cm^{-2}$, which are in good agreement with CNM diodes. We have seen that the I-V curves simulated with CERN model are in better agreement with those observed in the sensors measurements. In order to improve this electrostatic behavior, we have done a collaboration with the University of Perugia to extend the combined bulk + surface radiation damage mode-ling scheme which is published two years ago. The goal is reproduce the macroscopic behavior of 3D detectors. There is a significant correlation between the I-V curves simulated with new extended Perugia model and experimental results compared to both previous radiation models results, making the model very promising for 3D and the LGAD detectors. We want to expand our study utilizing a full 3D simulation domain to better understand this aspect, particularly those regions that potentially play a vital role for high field effects. In addition, since the physics of 3D detector is well known in this thesis, we plan to investigate a new approach in radiation detectors with 3D trench electrodes. This geometry will produce more uniform electric and weighing fields than present devices, allowing for better timing resolution while retaining or improving on the benefits of a 3D geometry.

Abstract

Abstract

In the last few years, there has been increased emphasis on silicon radiation detectors due to their importance for a wide range of industrial, medical and scientific applications. Unlike planar technology, the use of the 3D one in the fabrication of these kind of detectors offers advanced performances. The exploitation of the third dimension within the silicon substrate in the case of planar detectors actives its volume to be terminated physically and electrically without dicing. The first goal of this thesis is to enables the dead area reduction of an existing X-ray imaging detector for the free-electron laser facilities and obtaining the required high breakdown voltage under all conditions (~ 500 V). In 3D detectors case, the columns electrodes penetrate vertically in the bulk. As a result, the active volume is decoupled from the inter-electrode distance causing a lower depletion voltage and trapping probability, reducing the power dissipation and minimizing the inter pitch charge sharing. This makes them a very tempting choice for the future High luminosity Collider (HL- LHC) upgrades, where they should withstand very large particle fluences up to (2×10^{16} n_{eq} cm^{-2}). 1-MeV equivalent neutrons. The second goal of this thesis is predicting the leakage current and charge collection efficiency (CCE) of small-pitch 3D sensors using TCAD simulation. The considered devices are irradiated at large fluences up to the maximum value foreseen at the innermost pixel layers at HL-LHC (2×10^{16} n_{eq} cm^{-2}). Results are compared with experimental data from 3D diodes measured with a position resolved laser system in order to predict high signal efficiency and charge multiplication effects at high voltage, investigating the different distribution of the electric field, in particular to presence/intensity of the double peak.

Keywords 3D technology, X-ray detectors, HL-LHC, small-pitch 3D sensors, TCAD simulation and Device characterization

Résumé

Au cours de ces dernières années, un engouement est de plus en plus observé vers les détecteurs de rayonnement au Silicium en raison des grandes possibilités qu’ils offrent dans un large éventail d'applications industrielles, médicales et scientifiques. Contrairement à la technologie planare, l'utilisation de la technologie 3D dans la fabrication de ce type de détecteurs permet d’obtenir des performances plus intéressantes. En effet, l'exploitation de la troisième dimension du substrat de Silicium dans le cas de détecteurs planaires permet d’avoir une vision globale de tout le volume de celui-ci. Le premier objectif de cette thèse est de réduire la zone « inactive » d'un détecteur d'imagerie à rayons X existant dans les installations laser à électrons libres et d'obtenir la haute tension de claquage requise dans toutes les conditions (~ 500 V). De plus, dans le cas des détecteurs 3D, les électrodes, qui se présentent sous forme de colonnes, pénètrent verticalement dans le volume de substrat. En conséquence, le volume actif est découplé de la distance inter-électrodes, ce qui entraîne une tension déplétion et une probabilité de piégeage plus faibles, réduisant ainsi la dissipation de puissance et minimisant le partage de charge entre les pas. Cela en fait un choix très tentant pour les futures mises à niveau du collisionneur à haute luminosité (HL-LHC), où ils devraient résister à de très grandes fluences de particules jusqu'à (2×10^{16} n_{eq} cm^{-2}) neutrons équivalents à 1 MeV. Le deuxième objectif de cette thèse est de prédire l’évolution du courant de fuite ainsi que l'efficacité de collecte de charge (CCE) de capteurs 3D à petit pas en utilisant la simulation TCAD. Les dispositifs considérés sont irradiés à de grandes fluences jusqu'à la valeur maximale prévue au niveau des couches de pixels les plus profondes au HL-LHC (2×10^{16} n_{eq} cm^{-2}). Les résultats que nous avons obtenus sont comparés aux données expérimentales relevées sur des diodes 3D caractérisées à l’aide d’un système laser à résolution de position afin de prédire une efficacité de signal élevée et des effets de multiplication de charge à haute tension, en étudiant la distribution du champ électrique, en particulier la présence/l'intensité du double pic observé dans ce cas-là.

Mots-clés : Technologie 3D, détecteurs de rayons X, HL-LHC, capteurs 3D à petit pas, simulation TCAD et caractérisation de dispositif

الملخص

في السنوات القليلة الماضية ، كان هناك تركيز متزايد على كاشفات إشعاع السيليكون نظرًا لأهميتها البالغة في مجال التطبيقات الصناعية، الطبية والعلمية. على عكس التكنولوجيا المستوية ، فإن استخدام تقنية التكنولوجيا ثلاثية الابعاد ، في تصنيع هذا النوع من المستشعرات يوفر أداءً متقدمًا. يؤدي استغلال البعد الثالث داخل كتلة الكاشف. تفعيل حجمها ماديًا وكهربائيًا. الهدف الأول من هذه الأطروحة هو تقليص المنطقة الميتة لكاشف الأشعة السينية الحالي لمرافق ليزر الإلكترون الحر والحصول على جهد التعطيل العالي المطلوب في جميع الظروف (~ 500 فولت). في حالة الكاشفات ثلاثية الأبعاد ، تخترق الأقطاب عموديًا كتلة الكاشف. نتيجة لذلك ، يتم فصل الحجم النشط عن المسافة بين الأقطاب الكهربية مما يتسبب في انخفاض جهد استنفاد واحتمال محاصرة ، مما يقلل من تبديد الطاقة ويقلل من الشحن الكهربائية المشتركة. وهذا يجعلها خيارًا مغريًا في الترقيات المقبلة لمصادم البروتونات ذو الإشعاع العالي في المستقبل ، حيث يجب أن تتحمل اشعاعات جسيمية كبيرة جدًا تصل إلى $(2\times10^{16}\,n_{eq}.cm^{-2})$ 1 MeV مكافئ نيوترونات. في الهدف الثاني من هذه الأطروحة هو التنبؤ بالتيارات الكهربائية وفعالية تحصيل الشحن الكهربائية الناتجة في كاشفات إشعاع السيلكون ذات الأبعاد الصغيرة بإستخدام برنامج المحاكاة. يتم تشعيع الأجهزة المدروسة بتأثيرات كبيرة تصل إلى القيمة القصوى المتوقعة في طبقات البكسل الداخلية في مصادم البروتونات ذو الإشعاع العالي HL-LHC $(2\times10^{16}n_{eq}cm^{-2})$. تتم مقارنة النتائج مع البيانات التجريبية مع الديود ثلاثية الأبعاد التي تم قياسها باستخدام نظام ليزر تم تحديد موضعه من أجل التنبؤ بفعالية تحصيل الشحن الكهربائية وتأثيرات مضاعفة الشحن عند الجهد العالي ، والتمعن في التوزيع المختلف للمجال الكهربائي ، ولا سيما وجود شدة الذروة المزدوجة.

الكلمات المفتاحية: المستشعرات ثلاثية الأبعاد صغيرة صغيرة البعد، مصادم البروتونات ذو الإشعاع العالي، كاشفات الأشعة السينية، المحاكاة و توصيف المستشعرات.

Scientific contributions

List of Publication(s) on Ph.D. Thesis

[1] **A. Boughedda**, M. Lakhdara, S. Latreche, et G. Dalla Betta, « Compact border termination for active-edge planar radiation detectors with enhanced breakdown voltage », *Micro Nano Lett.*, vol. 15, nº 13, p. 969-971, nov. 2020, doi: 10.1049/mnl.2020.0295.

[2] **A. Boughedda,** M. Lakhdara, S. Latreche, R. Mendicino, et G. F. Dalla Betta, « TCAD simulation of small-pitch 3D sensors for pixel detector upgrades at High Luminosity LHC », *J. Phys. Conf. Ser.*, vol. 1766, nº 1, p. 012014, janv. 2021, doi: 10.1088/1742-6596/1766/1/012014.

[3] **A. Boughedda**, M. Lakhdara, S. Latreche, R. Mendicino, et G.-F. Dalla Betta, « Comparing different bulk radiation damage models in TCAD simulations of small-pitch 3D Si sensors », J. Instrum., vol. 16, no 10, p. C10006, oct. 2021, doi: 10.1088/1748-0221/16/10/C10006.

List of Presentation(s) on Conferences/Workshops

[1] **A. Boughedda,** M. Lakhdara, S. Latreche, R. Mendicino, et G. F. Dalla Betta, « TCAD simulation of small-pitch 3D sensors for pixel detector upgrades at High Luminosity LHC », The Tenth International Conference on High Energy and Astroparticle Physics,(TIC-HEAP), Octobre 2019- Constantine, Algeria

https://indico.cern.ch/event/776520/attachments/1763883/3220589/BoA_Final4.pdf

[2] **A. Boughedda,** M. Lakhdara, S. Latreche, R. Mendicino, et G. F. Dalla Betta, « Comparing different bulk radiation damage models in TCAD simulations of small-pitch 3D Si sensors », 22nd International Workshops on Radiation Imaging Detectors), 27 juin 2021 à 1 juillet 2021-Ghent,Belgium
https://indico.cern.ch/event/820476/contributions/4372788/

[03] **Collaboration with the University of Perugia** to extend the combined bulk +surface radiation damage modeling scheme to reproduce the macroscopic behavior of 3D detectors.
F. Moscatelli et al " Simulations of radiation hard detectors for timing applications" pp11. AIDAInnova WP6 Meeting,Septempbre.2021.

Conference not included in the thesis

[2] BENDILMI Mohammed Sofiane, **BOUGHEDDA Abderrezak ,** ZIARI Zahira « Réalisation d'un banc automatisé de décharge couronne multi- pointes», Journées Sciences Innovations (JSI'2018), FABLAB CIRTA, Constantine (Algérie)., 22-23 Avril 2018.

[2] BENDILMI Mohammed Sofiane, **BOUGHEDDA Abderrezak ,** ZIARI Zahira « banc automatisé de décharge couronne multi- pointes », Salon National des Produits de la Recherche organisé par la DGRSDT au Palais des Expositions., la SAFEX ,Alger (Algérie), 02-04 juillet 2018.